creative commons
COMMONS DEED

저작자표시-비영리-변경금지 2.0 대한민국

이용자는 아래의 조건을 따르는 경우에 한하여 자유롭게

- 이 저작물을 복제, 배포, 전송, 전시, 공연 및 방송할 수 있습니다.

다음과 같은 조건을 따라야 합니다:

저작자표시. 귀하는 원저작자를 표시하여야 합니다.

비영리. 귀하는 이 저작물을 영리 목적으로 이용할 수 없습니다.

변경금지. 귀하는 이 저작물을 개작, 변형 또는 가공할 수 없습니다.

- 귀하는, 이 저작물의 재이용이나 배포의 경우, 이 저작물에 적용된 이용허락조건을 명확하게 나타내어야 합니다.
- 저작권자로부터 별도의 허가를 받으면 이러한 조건들은 적용되지 않습니다.

저작권법에 따른 이용자의 권리는 위의 내용에 의하여 영향을 받지 않습니다.

이것은 이용허락규약(Legal Code)을 이해하기 쉽게 요약한 것입니다.

Disclaimer

dCollection

[UCI]I804:24011-200000237520

2009년 2월

박사학위 논문

Development of Chemical and Biological Sensors Based on Porous Silicon and Silicon Nanoparticles

조 선 대 학 교 대 학 원

화 학 과

장 승 현

Development of Chemical and Biological Sensors Based on Porous Silicon and Silicon Nanoparticles

다공성 실리콘과 실리콘 나노입자를 기초로 한
화학 및 생물학센서의 개발

2009년 2월 25일

조 선 대 학 교 대 학 원

화 학 과

장 승 현

Development of Chemical and Biological Sensors Based on Porous Silicon and Silicon Nanoparticles

지도교수 손 홍 래

이 논문을 이학박사학위신청 논문으로 제출함.

2008년 10월

조 선 대 학 교 대 학 원

화 학 과

장 승 현

장승현의 박사학위논문을 인준함

위원장　전남대학교　교수　우희권　(인)

위　원　조선대학교　교수　조성동　(인)

위　원　조선대학교　교수　고문주　(인)

위　원　조선대학교　교수　이범규　(인)

위　원　조선대학교　교수　손홍래　(인)

2008년 12월

조 선 대 학 교　대 학 원

TABLE OF CONTENTS

TABLE OF CONTENTS	**I**
LIST OF SYMBOLS AND ABBREVIATIONS	**IX**
LIST OF TABLES	**XIII**
LIST OF SCHEMES	**XIV**
LIST OF FIGURES	**XV**
ABSTRACT	XXIV

PART I. INTERFEROMETRIC SENSORS BASED ON POROUS SILICON

CHAPTER ONE

INTRODUCTION OF POROUS SILICON 2

1.1	**History and Current Application of Porous Silicon**	2
1.2	**Electrochemical Preparation of Porous Silicon**	4
1.2.1	Etching Mechanism	4
1.2.2	Electrochemical Etching Setup	7
1.3	**Anodization Parameters**	9
1.3.1	Current Density	9
1.3.2	Concentration of Etching Solution and Anodization Time	12
1.4	**Properties of Porous Silicon**	14
1.4.1	Substrate Properties	14
1.4.2	Porosity	15
1.4.3	Thickness	16
1.4.4	Refractive Index	17
1.4.5	Surface Area	17
1.4.6	Optical Properties and Bench Setup	18

1.5 Stabilization of Porous Silicon 20
1.5.1 Oxidation 20
1.5.2 Surface-Derivatization (Hydrosilylation) 22

1.6 Multi-structures of Porous Silicon 25
1.6.1 Theory of Multilayer Structures 25
1.6.2 Properties of Multilayer Structures 27

1.7 Instruments and Data Acquisitions 31

1.8 References 32

CHAPTER TWO

DETECTION OF TOXIC ORGANOPHOSPHATE NERVE AGENTS USING DBR POROUS SILICON INTERFEROMETER 40

2.1 Introduction 40

2.2 Experiments 42
2.2.1 Sample Preparation 42
2.2.2 Instrumentation and Data Acquisition 42

2.3 Results and Discussion 43
2.3.1 Optical Structure of DBR PSi Interferometer 43
2.3.2 Data Analysis for Sensing Nerve Gases 45
2.3.3 Detection Limit 48

2.4 Conclusions 49

2.5 References 50

CHAPTER THREE
DETECTION OF G-TYPE NERVE AGENT SIMULANTS BASED ON A DOUBLE REFLECTION DBR POROUS SILICON INTERFEROMETER 52

3.1 Introduction..... 52

3.2 Experiments..... 54

3.3 Results and Discussion..... 55

3.4 Conclusions..... 63

3.5 References..... 64

CHAPTER FOUR
MULTI-ENCODED RUGATE POROUS SILICON AS NERVE AGENT SENSORS 67

4.1 Introduction..... 67

4.2 Experiments..... 69

4.3 Results and Discussion..... 70

4.4 Conclusions..... 78

4.5 References..... 79

CHAPTER FIVE
SURFACE-FUNCTIONALIZED DBR POROUS SILICON FOR SENSING ORGANOPHOSPHATES USING VARIOUS DETECTION LIGHT SOURCES 82

5.1 Introduction 82

5.2 Experiments 84

5.3 Results and Discussion 85

5.4 Conclusions 92

5.5 References 93

CHAPTER SIX
FABRICATION AND CHARACTERIZATION OF SURFACE-FUNCTIONALIZED DBR SMART PARTICLES FOR THE DETECTION OF BIO-MOLECULES 96

6.1 Introduction 96

6.2 Experiments 98
6.2.1 Preparation of DBR PSi Sample 98
6.2.2 Thermal Oxidation of Free-standing DBR PSi Film 98
6.2.3 Preparation of DBR Smart Particles 99
6.2.4 Synthesis of Biotin Tetrafluorophenyl Ester 99
6.2.5 Surface Derivatization of Oxidized DBR Smart Particles 100
6.2.6 Instruments and Data Acquisitions 100

6.3 Results and Discussion 101

6.4 Conclusions 112

6.5 References 113

PART II. FLUORESCENT SENSORS BASED ON NANOAGGREGATES AND NANOPARTICLES CONTAINING SILICON AND GERMANIUM

CHAPTER SEVEN

INTRODUCTION OF ORGANOSILICON CHEMISTRY 117

7.1 What is Organometallic Chemistry? 117

7.2 History of Organometallic Chemistry 118

7.3 Classification of Organometallic Chemistry 119

7.4 Organosilicon Chemistry 120
7.4.1 Organosilanes 120
7.4.2 Siloxides 121
7.4.3 Silyl Halides 122
7.4.4 Silyl Hydrides 123
7.4.5 Hydrosilylation 124
7.4.6 Silenes 124
7.4.7 Siloles 125

7.5 Introduction of Siloles 126
7.5.1 Unique Electronic Structure of Silole 126
7.5.2 Various Silole Derivatives 130

7.6 References 135

CHAPTER EIGHT

ENHANCEMENT OF PHOTOLUMINESCENCE EFFICIENCY OF POLYSILOLE BY AGGREGATION-INDUCED EMISSION 138

8.1 Introduction 138

8.2 Experiments 139

8.3 Results and Discussion 140

8.4 Conclusions 146

8.5 References 147

CHAPTER NINE

ENHANCEMENT OF PHOTOLUMINESCENCE EFFICIENCY OF POLYGERMOLE BY AGGREGATION-INDUCED EMISSION 149

9.1 Introduction 149

9.2 Experiments 150
9.2.1 Generals 151
9.2.2 Syntheses 152
9.2.2.1 Preparation of 1,1-dichloro-2,3,4,5-tetraphenylgermole **1** 152
9.2.2.2 Preparation of Polytetraphenylgermole **2** 152
9.2.2.3 Preparation of Polytetraphenylgermole Nanoaggregates **3** 153

9.3 Results and Discussion 154

9.4 Conclusions 160

9.5 References 161

CHAPTER TEN

FLUORESCENT CHEMOSENSORS BASED ON AMINOSILOLE FOR THE DETECTION OF INORGANIC ACIDS 163

10.1 Introduction 163

10.2 Experiments 165
10.2.1 Generals 165
10.2.2 Syntheses 166
10.2.2.1 Preparation of 1-chloro-1-methyl-2,3,4,5-tetraphenylsilole **1** 166
10.2.2.2 Preparation of 1-amino-1-methyl-2,3,4,5-tetraphenylsilole **2** 166
10.2.2.3 Preparation of 1-methyl-1-hydro-2,3,4,5-tetraphenylsilole **3** 167
10.2.2.4 Preparation of 1-methyl-1-(3-amino)propyl-2,3,4,5-tetraphenylsilole **4** 167

10.3 Results and Discussion 169

10.4 Conclusions 179

10.5 References 180

CHAPTER ELEVEN

DETECTION OF EXPLOSIVES BASED ON HIGHLY FLUORESCENT POLYMETALLOLES/PMPS COMPOSITE NANOAGGREGATES USING AIE AND ENERGY MIGRATION 182

11.1 Introduction 182

11.2 Experiments 185

11.3 Results and Discussion 187
11.3.1 Energy Migration from PMPS to PTPS 187
11.3.2 Fluorescence Quenching Studies with Nitroaromatic Analytes 194
11.3.3 Plot Studies of Stern-Volmer 198
11.3.4 Visible Trace of TNT 201
11.3.5 Detection Mechanism 202

11.4 Conclusions..... 204

11.5 References..... 205

CHAPTER TWELVE

NEW SYNTHETIC ROUTE OF ALKYL-TERMINATED SILICON NANOPARTILES AND THEIR OPTICAL CHARACTERISTICS 208

12.1 Introduction..... 208

12.2 Experiments..... 210
12.2.1 Materials..... 210
12.2.2 Synthesis of sodium benzophenone ketal..... 210
12.2.3 Synthesis of *n*-butyl-terminated Si Nanoparticles..... 211
12.2.4 Characterization..... 213

12.3 Results and Discussion..... 214

12.4 Conclusions..... 221

12.5 References..... 222

APPENDICES 227

APPENDIX A : CURRICULUM VITAE 238

APPENDIX B : ACKNOWLEDGMENTS 234

LIST OF SYMBOLS AND ABBREVIATIONS

Å	Angstrom
β	Beta
cm	Centimeter
℃	Celsius temperature scale
$\mathbf{m^3}$	Cubic Meter
d	Diameter
δ	Delta
ε	Epsilon
λ_{em}	Emission Wavelength
fg	Femtogram
d	Film thickness
g	Gram
$\mathbf{h^+}$	Hole
h	Hour
kJ	Kilojoule
λ	lambda
L	Liter
m	Mass
M	Molarity
μm	Micrometer
mg	Milligram
mA	Milliampere
mmol	Millimole
mL	Milliliter
λ_{max}	Maximum Wavelength
μ	Mu
***μ*M**	Micromolarity

M_w	Molecular Weight
μg	Microgram
MHz	MegaHertz
ν	Nu
nm	Nanometer
Ω	Ohm
π	Pi
%	Percent
n	Refractive Index
σ	Sigma
T	Thickness
t	Time
vs	Versus
V	Volume
W	Watt
A.U.	Arbitrary Units
Al	Aluminium
AIE	Aggregation-Induced Emission
BET	Brunauer-Emmett-Teller
BuLi	Butyllithium
Cu	Copper
CWA	Chemical Warfare Agents
c-Si	Crystalline Silicon
CCD	Charge-Coupled Detector
CdSe	Cadmium Selenide
DCP	Diethyl Chlorophosphate
DFP	Diisopropyl Phosphonate
DEEP	Diethyl Ethylphosphonate
DMMP	Dimethyl Methylphosphonate

DNA	Deoxyribonucleic Acid
DMF	Dimethyl Formaldehyde
DNT	Dinitrotoluene
EL	Electroluminescence
EDS	Energy Dispersive X-ray Spectrometry
FIPOS	Full Isolated Porous Oxidized Silicon
FWHM	Full-Width at Half-Maximum
F-P	Fabry-Pérot
FT-IR	Fourier Transform Infrared Spectroscopy
HOMO	Highest Ocuppied Molecular Orbital
HF	Hydrofluoric Acid
IC	Integrated Circuit
InP	Indium phosphate
InAs	Indium Arsenide
LCT	Lethal Concentration
LED	Light Emitting Diode
LUMO	Lowest Unoccupied Molecular Orbital
$LiAlH_4$	Lithium Aluminum Hydride
MEMS	Micro Electro Mechanical Systems
MALDI	Matrix-Assisted Laser Desorption Ionization
Mg_2Si	Magnesium Silicide
NaOH	Sodium Hydroxide
NA	Nerve Agents
NA	Nanoaggregates
NP	Nanoparticle
NMR	Nuclear Magnetic Resonance
OSHA	Occupational Safety and Health Administration
PSi	Porous Silicon
Pt	Platinum
PL	Photoluminescence
PA	Picric Acid
PBS	Phosphate Buffer Solution
PSA	Particle Size Analyzer
PTPS	Polytetraphenylsilole
PTPG	Polytetraphenylgermole
PMPS	Polymethylphenylsilane

ppm	Part Per Million
ppb	Part Per Billion
ppt	Part Per Trillion
pmol	Picomole
R.T.	Room Temperature
SAED	Selected Area Electron Diffraction
Si	Silicon
SiO_2	Silicon Dioxide
sec	Second
SAW	Surface Acoustic Wave
SOI	Silicon-On-Insulator
S-V Eqn	Stern-Volmer Equation
SWNT	Single-walled Nanotube
TLC	Thin-Layer Chromatography
TNT	Trinitrotoluene
TMS	Tetramethylsilane
THF	Tetrahydrofuran
TMEDA	Tetramethyl Ethylene Diamine
TEP	Triethylphosphate
TEOS	Tetraethyl orthosilicate
TOPO	Tri-*n*-octylphosphineoxide
UV	Ultraviolet
UV-Vis	Ultraviolet-Visible

LIST OF TABLES

Table 4.1 FE-SEM images of single (A) and triple rugate-structured PSi (B)

Table 7.1 Organometallic chemistry timeline

Table 7.2 Classification of organometallic chemistry

LIST OF SCHEMES

Scheme 7.1 Synthetic routes of silole and silole derivatives **1-9**

Scheme 7.2 Synthetic routes of silole and silole derivatives **10-17**

Scheme 7.3 Synthetic routes of silole and silole derivatives **18-23**

Scheme 9.1 Synthetic routes of compounds **1-3**

Scheme 10.1 Synthetic routes of compounds **1-4**

Scheme 11.1 Synthetic routes of silole-germole copolymer

Scheme 11.2 Schematic diagram of electron-transfer mechanism for quenching the PL of polymetallole/PMPS composite nanoaggregates by TNT

Scheme 12.1 Preparation of *n*-butyl-capped silicon nanoparticles

LIST OF FIGURES

Figure 1.1 Dissolution mechanism of crystalline silicon in hydrofluoric acid associated with the formation of porous silicon. Steps (A) through (E) represent the sequence of steps in the dissolution process

Figure 1.2 Experimental setup to produce porous silicon. Anodization is conducted under a constant current with the hydrofluoric acid electrolyte in the top portion of the Teflon cell. The aluminum foil serves as the anode and the platinum wire as the cathode.

Figure 1.3 PSi porosity (top) and etch-rate (bottom) dependence versus current density for p-type crystalline silicon substrate anodized in 35% hydrofluoric acid concentration electrolyte

Figure 1.4 Surface FE-SEM images of PSi with different current densities

Figure 1.5 Thickness of PSi with different anodization time for p-type crystalline silicon substrates anodized at a fixed current density of 50 mA/cm^2

Figure 1.6 Optical properties of porous silicon: photoluminescence (left) and reflectivity (right).

Figure 1.7 Optical bench setup for obtaining the optical properties of porous silicon

Figure 1.8 Chemical scheme for the thermal oxidation (top) and comparison of FT-IR spectra between freshly etched PSi and thermally oxidized PSi (bottom)

Figure 1.9 Schematic hydrosilylation chemistry. Hydrosilylation involves the insertion of an unsaturated bond, alkyne or alkene, into Si-H bond, resulting in Si-C bond formation and formation of alkenyl or alkyl groups, respectively.

Figure 1.10 Comparison of FT-IR spectra between freshly etched PSi and hydrosilylated PSi with 1-dodecene

Figure 1.11 Multiple interference of thin film structure. Representation of the reflection and transmission of light by a single (A) and a multilayer structure (B)

Figure 1.12 Schematic pictures on the formation of PSi multilayer structures. By pulsing between two different current densities, two different porosity PSi layers can be formed (left) and step-functions used to approximate the sinusoidal variation of refractive index (right).

Figure 1.13 Photo (top) and optical reflectivity spectra (bottom) of specific reflectors or filters anywhere in the visible range. This reflective wavelength can be controlled by tuning many etching parameters.

Figure 1.14 Cross-sectional SEM images of PSi multilayer where the different layers present alternating porosity (refractive index) layers

Figure 2.1 Structures of G-type nerve agents and organophosphate nerve agent simulants

Figure 2.2 SEM images of DBR PSi interferometer. From left; top view of DBR PSi, middle; cross-sectional of SEM image of DBR PSi indicating that the thickness of DBR PSi is about 6.87 ㎛, right; detailed cross-sectional SEM image of porous nanostructure in

DBR PSi. Low current (LC) and high current (HC) indicate two distinct refractive index, respectively.

Figure 2.3 Reflectivity spectra of DBR PSi were recorded every 15 sec for 1 min, *in situ*, under the exposure of a flux of (a) TEP (135 ppm), (b) DMMP (290 ppm), (c) DEEP (135 ppm) in air with a flow rate of 5 L/min. A red-shift of (a) 25 nm, (b) 10 nm, and (C) 10 nm is observed, respectively.

Figure 2.4 Plot for dosing response showing the detection of TEP vapor based on DBR PSi and photograph for sensing of TEP vapor displays color change of DBR PSi as vapor in and out

Figure 2.5 Plot for showing the detection limit of DMMP at 8.8 mg/m^3 (1.5 ppm) by using DBR PSi

Figure 3.1 Reflectivity spectra of DBR PSi with one or two reflection peaks

Figure 3.2 Surface and cross-sectional FE-SEM images of DBR PSi showing two reflection bands

Figure 3.3 Reflectivity spectra of DBR PSi samples DBR PSi showing single or two reflection peaks recoded for 30 sec using the tungsten-halogen lamp as a light source. A red-shift of reflectivity for single reflection DBR PSi, 1a) TEP; 25 nm, 1b) DMMP; 10 nm, 1c) DEEP; 10 nm and double reflection DBR PSi, 2a) TEP; 13 nm for the first DBR peak and 18 nm for the second DBR peak, 2b) DMMP; 22 nm and 32 nm, 2c) DEEP; 39 nm and 52 nm are observed.

Figure 3.4 Comparison of the red-shifts of two reflection peaks with different nerve agent analytes

Figure 3.5 Response for the reflective intensities at two fixed wavelengths of DBR PSi showing two reflection peaks under the exposure of DMMP vapor

Figure 4.1 Representation of the encoding method and reflectivity specta. (A) single sine components and reflectivity spectrum of single rugate PSi; (B) a composite waveform summed three individual sine components; (C) reflectivity spectrum of triple rugate-structured PSi

Figure 4.2 FE-SEM images of single (A) and triple rugate-structured PSi (B)

Figure 4.3 Detection mechanism of nerve agent simulant (TEP) vapors based on triply encoded rugate PSi

Figure 4.4 Optical reflectivity spectra of triple rugate-structured PSi in air (solid line) and under the exposure nerve agent vapors (dotted line) for 1 min, respectively.

Figure 5.1 Surface and cross-sectional FE-SEM images of Cu coated DBR PSi sample and EDX spectrum of element percent at the same location (Si:Cu = 69:31)

Figure 5.2 (A) Reflectivity spectra of DBR PSi sample containing copper (II) sulfate under a flux of TEP in air. (B) Decreases of reflective intensity for DBR PSi samples containing different concentrations of copper (II) sulfate under a flux of DMMP in air

Figure 5.3 Schematic diagram of the sensing mechanism with surface-modified DBR PSi sample

Figure 5.4 Reflectivity spectra of DBR PSi samples under a flux of TEP (A), DMMP (B), DEEP (C) in air when a LED (λ_{em} = 520, 590 nm) is used as a light source, and DMMP (D) in air when a laser (λ_{em} = 532 nm) is used as a light source.

Figure 5.5 Plots for showing the detection limits of DMMP at 8.8 mg/m^3 (1.5 ppm) by using DBR PSi when a tungsten-halogen lamp is used as a light source and at 0.88 mg/m^3 (150 ppb) by using DBR PSi when LED and laser are used as a light source.

Figure 6.1 Surface and 3-dimensional images of DBR smart particle

Figure 6.2 Schematic process for surface modification of DBR smart particles with biotin and silole groups

Figure 6.3 Optical reflectivity (dotted line) and photoluminescence (solid line) spectrum of biotin/silole-derivatized DBR smart particles. Photographs of biotin/silole-derivatized DBR smart particles under white light (top) and black light (bottom)

Figure 6.4 Diffuse reflectance FT-IR spectra of (A) a freshly etched DBR smart particle, (B) oxidized DBR smart particle at 300℃ for 3 h, (C) functionalized DBR smart particle with (3-aminopropyl) trimethoxysilane, and (D) subsequent reaction of the surface with biotin

Figure 6.5 Optical reflectivity spectra of fresh, oxidized, surface-functionalized, and biotin derivatized DBR smart particle

Figure 6.6 Sensing of avidin and streptavidin based on biotin derivatized DBR smart particle in PBS

Figure 7.1 Structures of silyl halides

Figure 7.2 Releative energy levels of the HOMO and LUMO for silole and cyclobutadiene, based on the HF/6-31G* calculations

Figure 7.3 Orbital correlation diagram for 1,1-dimethylsilole, based on the PM3 calculations

Figure 7.4 Shape of the HOMO and LUMO of silole and cyclopentadiene

Figure 8.1 Space filling model structure of polysilole

Figure 8.2 Photograph of polysilole in THF (10 mg/L, left) and polysilole nanoaggregates

Figure 8.3 Fluorescence spectra of polysilole aggregates in water-THF mixtures (% water from top; 99%, 90%, 80%, 70%, 60%, 50%)

Figure 8.4 Plot of the relative intensity of polysilole aggregates *vs* % water by volume

Figure 8.5 FE-SEM images of polysilole nanoparticles from (a) 90%, (b) 80%, and (c) 70% water fraction

Figure 9.1 Relative PL spectra and plots of the relative intensity of monomer, polymer, and polymer nanoaggregates

Figure 9.2 PL spectra of polygermole nanoaggregates in water-THF mixtures and plot of the relative intensity of polygermole nanoaggregates *vs* % water by volume.

Figure 9.3 Particle size distributions of polygermole nanoaggregates in the water/THF mixtures with (A) 90%, (B) 80%, and (C) 70%

Figure 9.4 FE-SEM images of polygermole nanoaggregates in the water/THF mixtures with (A) 90%, (B) 80%, and (C) 70%

Figure 10.1 UV-vis absorption and fluorescence spectra. A; 1-amino-1-methyl-2,3,4,5-tetraphenylsilole **1**, B;1-methyl-1-(3-amino)propyl-2,3,4,5 -tetraphenylsilole **2**

Figure 10.2 FL quenching spectra (A) and Stern-Volmer plot (B) of **1**

Figure 10.3 FL enhancing spectra (A) and Stern-Volmer plot (B) of **2**

Figure 10.4 Enhancing photoluminescence spectra of 1-methyl-1-(3-amino) propyl-2,3,4,5-tetraphenylsilole **4** with different concentration of inorganic acids

Figure 10.5 Lifetime of **2** and photoluminescence quenched **2** with HCl

Figure 10.6 Photograph of **2** after exposing 1 ppm of HCl vapor for 5 s under 365 nm UV-lamp

Figure 10.7 Visible traces of photoluminescene quenching of **2** for investigation of the detection limit

Figure 11.1 Structures of common nitroaromatic compounds as explosives

Figure 11.2 PL Spectra of PTPS, PTPG, PMPS, PTPS-PMPS, and PTPG-PMPS mixture in nanoaggregates state

Figure 11.3 PL Spectra of PTPS, PMPS, and PTPS-PMPS mixture in molecular state

Figure 11.4 PL spectra of polymetalloles *vs* PMPS weight percent

Figure 11.5 Enhancement of PL efficiency of polymer, polymer nanoaggregates, and polymer/PMPS composite nanoaggregates at the same concentration (1 ppm)

Figure 11.6 Photograph from silole monomer in THF (10 mg/L) to PTPS/PMPS composite nanoaggregates (99 : 1 by volume, 10 mg/L) under black light

Figure 11.7 FE-SEM images of polymetallole/PMPS nanoaggregates in the water/THF mixtures with 70% (top) and 99% (bottom)

Figure 11.8 Quenching of photoluminescence spectra of PTPS/PMPS composite nanoaggregates with (A) DNT, from top 5.5×10^{-7} M, 1.1×10^{-6} M, 1.65×10^{-6} M, 2.2×10^{-6} M, 2.75×10^{-6} M, 3.3×10^{-6} M, (B) TNT, from top 4.4×10^{-7} M, 8.8×10^{-7} M, 1.32×10^{-6} M, 1.76×10^{-6} M, 2.2×10^{-6} M, 2.64×10^{-6} M, (C) picric acid, from top 4.36×10^{-7} M, 8.72×10^{-7} M, 1.31×10^{-6} M, 1.74×10^{-6} M, 2.18×10^{-6} M, 2.61×10^{-6} M

Figure 11.9 Quenching of photoluminescence spectra of PTPG/PMPS composite nanoaggregates with (A) DNT, from top 5.5×10^{-7} M, 1.1×10^{-6} M, 1.65×10^{-6} M, 2.2×10^{-6} M, 2.75×10^{-6} M, 3.3×10^{-6} M, (B) TNT, from top 4.4×10^{-7} M, 8.8×10^{-7} M, 1.32×10^{-6} M, 1.76×10^{-6} M, 2.2×10^{-6} M, 2.64×10^{-6} M, (C) picric acid, from top 4.36×10^{-7} M, 8.72×10^{-7} M, 1.31×10^{-6} M, 1.74×10^{-6} M, 2.18×10^{-6} M, 2.61×10^{-6} M

Figure 11.10 Quenching of photoluminescence spectra of PTPS-PTPG Copolymer/PMPS composite nanoaggregates with (A) DNT, from top 5.5×10^{-7} M, 1.1×10^{-6} M, 1.65×10^{-6} M, 2.2×10^{-6} M, 2.75×10^{-6} M, 3.3×10^{-6} M, (B) TNT, from top 4.4×10^{-7} M, 8.8×10^{-7} M,

1.32×10^{-6} M, 1.76×10^{-6} M, 2.2×10^{-6} M, 2.64×10^{-6} M, (C) picric acid, from top 4.36×10^{-7} M, 8.72×10^{-7} M, 1.31×10^{-6} M, 1.74×10^{-6} M, 2.18×10^{-6} M, 2.61×10^{-6} M

Figure 11.11 Stern-Volmer plots; from top (A) PTPS/PMPS composite nanoaggregates, (B) PTPG/PMPS composite nanoaggregates, and (C) PTPS-PTPG copolymer/PMPS composite nanoaggregates

Figure 11.12 Comparison of Stern-Volmer plots; from top (A) picric acid, (B) TNT, and (C) DNT

Figure 11.13 TNT residue hand print visualized as quenched luminescence on paper developed with PTPS/PMPS composite nanoaggregates and illuminated with UV light

Figure 12.1 TEM micrograph for the as-prepared *n*-butyl-capped Si nanoparticles (A, B) and selected area electron diffraction (SAED) patterns of *n*-butyl-capped Si nanoparticles (C)

Figure 12.2 Particle size distributions of *n*-butyl-capped Si nanoparticles

Figure 12.3 FT-IR spectrum for silicon nanoparticles terminated with *n*-butyl groups

Figure 12.4 UV absortion and PL spectra of *n*-butyl-capped Si nanoparticles (A) and stability measurement of PL of *n*-butyl-capped Si nanoparticles (B)

초 록

다공성 실리콘과 실리콘 나노입자를 기초로 한 화학 및 생물학센서의 개발

박사과정 : 장 승 현
지도교수 : 손 홍 래
조선대학교 화학과

최근 수 십 년간 전기·전자 및 금속·반도체기술이 눈부신 발전을 이룩하였다면 21세기 현대과학에서는 새로운 형태나 특성을 연구하는 영역으로 나노과학(nanoscience) 및 나노기술(nanotechnology)이 급속히 발전하고 있다. 현대 화학이 여러 분야로 세분화되고, 전문화되어지면서 광화학 (photochemistry)이나 나노화학 (nanochemistry)에 대한 관심도가 매우 높아지고 있다. 특히, 나노(nano) 소재를 이용한 분야가 매우 빠른 속도로 발전하고 있다. 나노과학은 나노소재의 합성 및 응용분야로 분류된다. “나노센서(nanosensor)”는 나노과학의 한 응용분야로서 분자 수준의 조작이 가능한 분자센서(molecular sensor)의 집적화 또는 나노소재 (nanomaterial)나 나노구조물 (nanostructure)의 특성을 이용한 센서를 의미한다. 나노소재로는 나노다공질재료 (nanoporous material), 금속 및 반도체소재의 나노와이어 (nanowire), 나노입자 (nanoparticle), 나노튜브 (nanotube) 등이 있으며 기질을 인지(recognition) 또는 감지(sensing)할 수 있는 나노소재로부터 장치(device)를 만들었을 경우 나노센서라 일컫는다.

최근 나노센서 또는 나노바이오센서 등에 대한 관심이 나노과학의 한 분야로서 지대한 관심의 대상이 되고 있는데 그 이유는 고감도, 초소형의 센서 구현을 통해서 생명현상

인 분자 간의 상호작용을 나노크기의 수준에서 탐구하려는 학문적인 관심과 함께 응용적인 측면에서 보건의료, 식품, 환경, 국방 등의 다양한 분야에서 활용되는 센서를 개발하기 위한 실질적인 중요성 때문에 학계와 연구소, 그리고 산업체에서 활발히 연구되고 있다. 특히 나노 신소재 개발 분야는 기초과학에서부터 첨단과학까지의 융합학제(interdisciplinary)간 학문 분야로 미래기술의 선점 및 국가경쟁력 확보에 있어서 우위를 차지하는데 중요한 역할을 할 것으로 기대된다.

따라서 본 연구논문의 주제는 나노화학 및 바이오센서 개발의 일환으로 반도체 실리콘 재료를 이용하여 화학 및 생물학적 센서재료의 개발을 목표로 한다. 연구논문의 구성은 전반부에는 실리콘 웨이퍼를 전기화학적 식각을 통하여 얻어진 다공성 실리콘을 이용하여 화학신경제 및 면역단백질을 탐지하는 센서재료로 사용하였고, 후반부에는 실리콘 및 게르마늄이 함유된 광 발광성 유기금속 고분자 및 그 나노응집체 또는 나노입자를 통하여 무기산과 폭발물의 구성성분인 니트로방향족 화합물을 탐지하는 센서재료로 사용하였다.

논문의 part I 에서 나노센서로 이용된 다공성 실리콘은 실리콘 나노구조물이며, 나노크기의 기공들이 존재하는 간섭 막들의 굴절률의 변화로부터 얻어지는 독특한 광학적 특성인 광 반사(optical reflection)성을 갖는다. 다공성 실리콘은 1950대에 Uhlir에 의해 실리콘 단결정을 전자연마 (electropolishing) 하다가 발견되었으며, 1990년대 다공성 실리콘의 효율적인 발광(luminescence)을 발견한 이래로, 이 분야는 화학·물리학적 광학 특성의 연구에 매우 광범위하게 이용되어지고 있다. 다공성 실리콘은 간섭 막의 굴절률 조절로 인해 가시광선 및 적외선 영역에서 특정한 파장에서 보강간섭을 갖는 반사 띠를 갖기 때문에 센서 등 여러 분야에 적용될 수 있는 좋은 소재이다. 또한, 바이오센서분야로 이용될 경우 분자인식현상 (molecular recognition event)으로 매 추가 분자를 인식할 때마다 신호를 적립할 수 있는 장점이 있어 인식체가 분자수준의 신호증폭 (molecular-level amplification)을 하게된다. 따라서 선택성을 높이고 탐지한계를 낮추는 방법론을 개선하기위해 다양한 전기화학적 식각방법을 개발한다면 다른 나노소재보다 비교우의에 있을 것으로 사료된다. 본 연구논문의 결과로 Cu(II) 촉매를 함유한 다공성 실리콘을 이용하여 약 150 ppb 가스농도의 화학신경제를 선택적으로 감지하였으며 약 2 pmol 농도의 면역단

백질을 탐지하는데 성공하였다.

논문의 part II 에서 나노센서로 이용된 유기금속 고분자 (Polymetallole)는 불포화 5각 고리에 실리콘이나 게르마늄으로 치환된 화합물의 고분자로서 최근에 그 독특한 광학적, 전자적 특성 때문에 유기전자 재료로서 흥미의 대상이 되어왔다. 이러한 독특한 성질들은 특히 광전자 기기에서 전자전달재료 (electron transporting materials)나 정공전달재료 (hole transporting materials), 발광재료 (light-emitting materials), 또는 화학적·생물학적 센서에 매우 유용하다. 최근 유기 발광재료들의 발광효율을 증가시키기 위한 연구는 매우 흥미의 대상이 되고 있는데 그 이유는 OLED (organic-light emitting diode)나 센서로서 응용할 경우 매우 중요하기 때문이다. 그러나 높은 발광성을 갖는 유기물이나 고분자는 고체 상태에서 덜 발광성을 갖는 종인 eximer의 형성으로 인한 분자의 응집으로 발광성의 감소를 발생한다. 이러한 단점을 극복하기위해 본 논문의 Chapters 8,9 에서는 실리콘과 게르마늄이 함유된 발광성 유기고분자가 응집된 고체 상태에서 발광효율이 오히려 더욱 증가하는 응집에 의해 유도되는 광 발광 (aggregation-induced emission, AIE라 부름)의 특성을 규명하였고, 발광효율을 증가 시킬 수 있는 다른 한 방법으로 Chapter 11에서는 한 화합물에서 다른 화합물로의 에너지 전달에 의해 발광효율을 증가 시키는 특성을 규명하였다. 상기에서와 같이 발광효율을 극대화시킨 유기금속이 함유된 고분자 나노응집체 (nanoaggregates)를 이용하여 폭발물의 구성 성분인 니트로방향족 화합물 (TNT, DNT, picric acid)들을 탐지하였다. 탐지 방법은 전자부유(electron rich)화합물인 실올 (silole) 및 저몰 (germole)고분자 나노응집체 및 나노입자에서 전자부족 분석물질(electron deficient analyte)인 폭발물로 전자가 이동함으로써 실올 (silole) 및 저몰 (germole)고분자 나노응집체 및 나노입자의 광 발광성 세기의 감소를 측정하는 것이다. 본 연구결과로 인하여 폭발물 탐지 한계 (detection limit)는 약 400 ppt (part per trillion)의 TNT 분자를 수분 이내로 감지하는 것이 가능하게 되었다.

폭발물을 탐지하는 방법으로는 여러 가지가 있으나 가장 널리 사용되는 장치로는 금속 탐지기로 흔히 공항에서 널리 쓰이고 있다. 그렇지만 실제로 폭발물이 아닌 금속을 탐지하는 장치로 거짓신호가 많은 단점이 있다. 폭발물을 탐지할 수 있는 다른 방법으로는 gas chromatography (GC)가 장착된 질량 분석기, surface-en hanced Raman spectroscopy,

nuclear quadrupole resonance, energy-dispersive X-ray diffraction, neutron activation analysis, electron capture detection, 그리고 cyclic voltammetry등이 있지만 이 또한 장치의 가격이 고가이고 부피가 크고 운반성이 떨어지므로 실험실 분석용으로 적합하지만 현지 탐지용으론 부적합한 단점이 있다. 따라서, 물리적인 탐지가 아닌 폭발물 분자 자체를 인식하는 화학적 센서 시스템이 절실히 필요하다. 이러한 요구사항을 비추어볼 때 본 연구를 통해 개발된 광 발광성 고분자 나노응집체 및 나노입자센서는 화학적 특성을 이용한 탐지방법으로 이러한 단점을 보완해 줄 수 있으며 또한 고가의 장비를 저가 장비로 대체 할 수 있는 장점이 있다. 본 연구는 다양한 학문 분야의 지식을 바탕으로 한 학제 간 융합학문 분야의 연구 결과로서 아직까지 정확히 확립되지 않은 나노센서, 나노바이오센서, 나노소재의 분석 및 그 응용과 관련된 중요한 정보를 구축하는데 크게 기여할 것으로 사료된다.

Part I.

Interferometric Sensors Based on Porous Silicon

Chapter One
Introduction of Porous Silicon

1.1 History and Current Applications of Porous Silicon

The porous silicon (PSi) material, an electrochemical derivative of silicon, is a natural nano-structured material that can be prepared easily without much sophistication. The history of PSi research is quite remarkable. This material was accidentally discovered by Ulhir at Bell Labs, USA in 1956 [1], followed by Turner [2] during a study on the electropolishing of silicon in hydrofluoric acid solution. Since the discovery, a small amount of interest in the field developed as a result of the poor understanding of the porous structure. In the 1970's, it was found that by thermal oxidation, the porous structure could be easily transformed into silicon dioxide and used as an isolation dielectric material [3,4]. Futher advances in electronic isolation technology by Japanese groups in the 1980's led to the development of full isolated porous oxidized silicon (FIPOS) [5] and silicon-on-insulator (SOI) [6] process.

It was not until 1990 when L. T. Canham first reported efficient, tunable, room temperature luminescence in the visible range from PSi [7] that interest in the field grew exponentially. From this point on, a large number of academic and industrial researchers from all over the world began to study the PSi pore structure [8,9], light emission mechanism [10,11], surface chemistry [12,13], and feasibility for optoelectronic applications [14,15].

The many favorable characteristics and the vast interest in PSi have given rise to a variety of new applications such as light emitting devices [15], multi-layer structure [16], solar energy conversion [17], chemical and biological sensors [18-23], drug delivery application [24], ultrasound generators [25], micro-engineering [26], astrophysics [27], signal processing [28], and nuclear science [29]. Due to these multi-functional applications of PSi, recently it has been proposed to be an educational vehicle for introducing nano-technology and inter-disciplinary materials science by eminent scientists in the field [30].

The extremely large surface to volume ratio (≥ 500 m^2/cm^3) of the PSi nano-structures, the its easy formation and control of the surface morphology through variation of the formation parameters, its compatibility of silicon IC technology and hence amenability to the development of smart system-on-chip sensors-all these properties have made it to be a very attractive sensing material.

1.2 Electrochemical Preparation of Porous Silicon

1.2.1 Etching Mechanism

PSi can be produced in many different ways. The most common way is the anode electrochemical etching of crystalline silicon in hydrofluoric acid solution. Although there is still some consideration regarding the surface dissolution mechanism, it is commonly agreed that holes are required for the dissolution mechanism to begin. The required holes are present in p-type crystalline silicon, but they need to be supplied for the dissolution process to be initiated in n-type crystalline silicon. Illumination is the most common way for supplying holes.

In normal anodization conditions, the surface of crystalline silicon is inert against hydrofluoric acid at low pH values. In 1991, Lehmann and Gösele [31] proposed a reaction model of the dissolution chemistry for the formation of PSi. This formation mechanism is illustrated in Figure 1.1. This model is well accepted and proposes that when silicon is under anodic bias and holes reach the surface, nucleophilic attack of the silicon-hydrogen bonds by fluorine ions occurs. This attack gives rise to a silicon-fluorine bond as shown in the step (A) of Figure 1.1. Once fluorine is attached, its large electro-negativity polarizes the structure making it possible for another fluorine ion to bond to the surface. During this process, an electron is ejected into the electrode and hydrogen is released as shown in the step (B) of Figure 1.1. At this point, the large polarization of two silicon-fluorine bonds lower the electron density from the silicon-silicon bonds, making them weak and vulnerable for attack by hydrofluoric acid and water as shown in the steps (C) and (D) of Figure 1.1. This results in the removal of a silicon atom in the form of the

soluble ion SiF_6^{2-} and leaves the remaining silicon atoms hydrogen terminated as shown in the step (E) of Figure 1.1.

The overall reaction can be expressed as follows [32]:

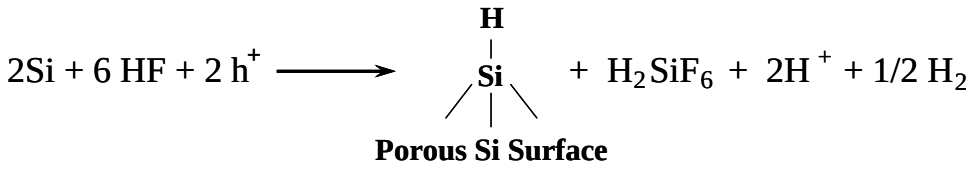

The removal of the silicon atom creates an atomic size dip or irregularity in the once atomically flat surface. The change in surface geometry concentrates the electric field lines on the irregularity site. PSi pore formation and side-wall dissolution will be inhibited by the depletion of holes. The depletion is caused by quantum confinement of charge carriers that results from the small dimensions of the pore walls. The quantum confinement increases the effective band-gap energy, making it more difficult for holes to enter the silicon region between the etched pores [31].

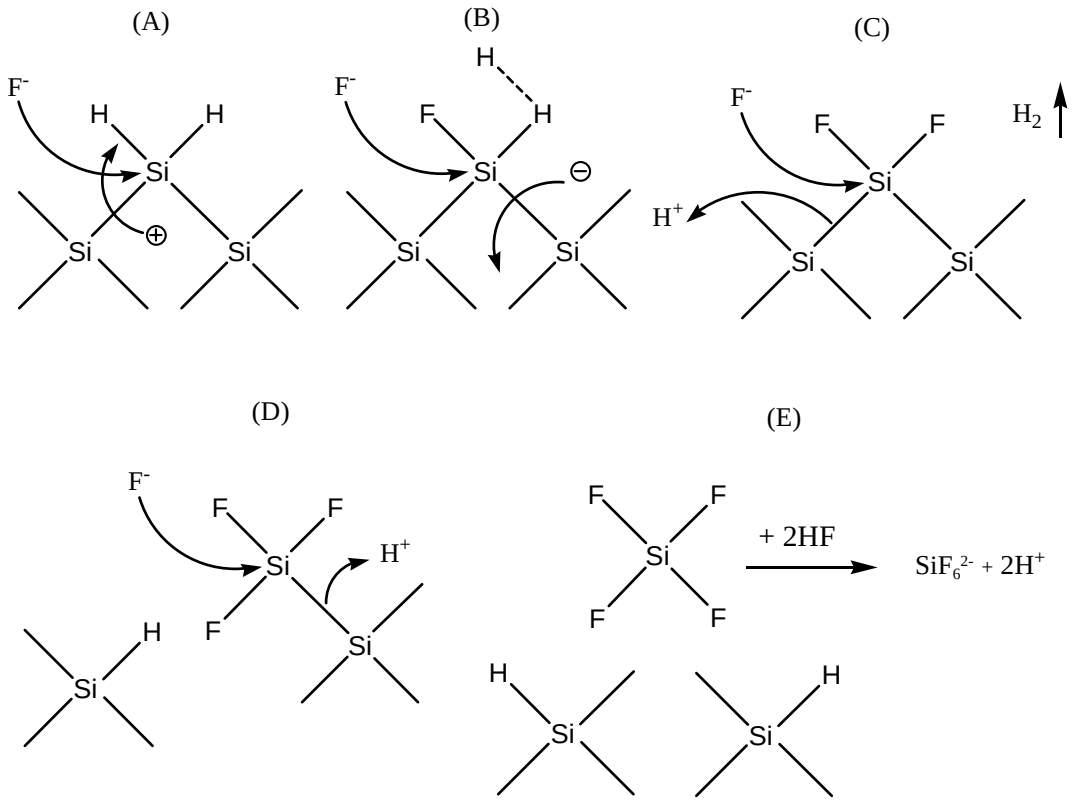

Figure 1.1. Dissolution mechanism of crystalline silicon in hydrofluoric acid associated with the formation of porous silicon. Steps (A) through (E) represent the sequence of steps in the dissolution process

1.2.2 Electrochemical Etching Setup

Figure 1.2 shows that a picture of experimental setup to produce PSi. The anodization cell is made of Teflon, which is resistive against attack from the hydrofluoric acid electrolyte. The aluminum foil serves as the anode and it is sandwiched between the top and bottom parts of the Teflon cell. For a better contact, a platinum wire is placed against the silicon wafer where leads can be connected. The cathode is a circular platinum wire that is submerged in the hydrofluoric acid electrolyte. The cathode is held in place, three wing nuts hold the entire anodization cell together during the electrochemical etching process. The hydrofluoric acid electrolyte is placed inside the top part of the Teflon cell. Enough electrolyte must be present to supply the required fluorine ions and to cover the platinum wire cathode. The top part of the Teflon cell has a circular window of area 1.2 cm^2 which exposes the silicon to hydrofluoric acid and forms the PSi. The entire electrochemical process is carried out under constant current supplied by a computer controlled Keithley 2420 power sourcemeter.

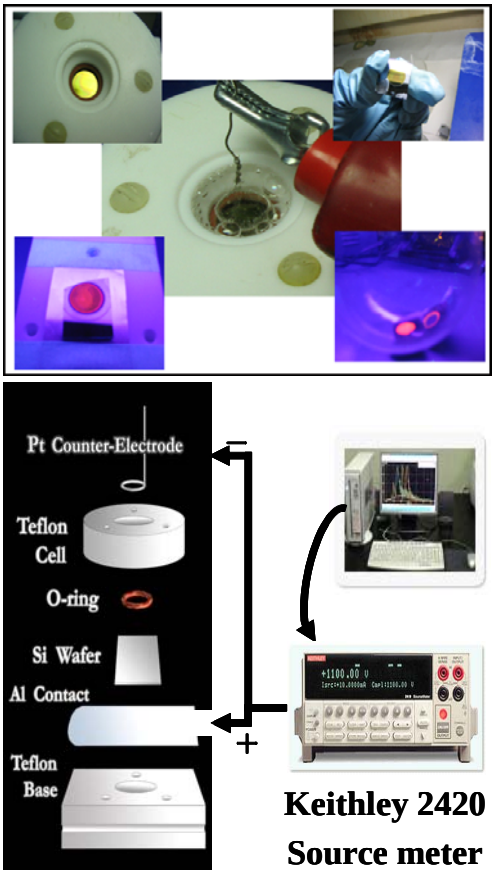

Figure 1.2. Experimental setup to produce porous silicon. Anodization is conducted under a constant current with the hydrofluoric acid electrolyte in the top portion of the Teflon cell. The aluminum foil serves as the anode and the platinum wire as the cathode.

1.3 Anodization Parameters

1.3.1 Current Density

PSi is produced by anodic etching of crystalline silicon under a constant current density. By varying the anodization current density, some general trends with respect to porosity and etching rate for a fixed hydrofluoric acid electrolyte concentration can be observed. As the current density increase, the silicon dissolution rate increases, resulting in a higher porosity and etching rate. Figure 1.3 shows that linear dependence of PSi porosity and etching rate as a function of current density.

The size of pores formed during anodization is predominantly controlled by the current density [33], with an increase in the pore size corresponding to an increase in the current density. At low current densities, the pores are randomly directed. When the current density gradually increased, the diameter of PSi pores increased. Figure 1.4 shows that surface images of etched PSi with different current densities is measured by field emission-scanning electron microscope (FE-SEM, Hitachi-4800S).

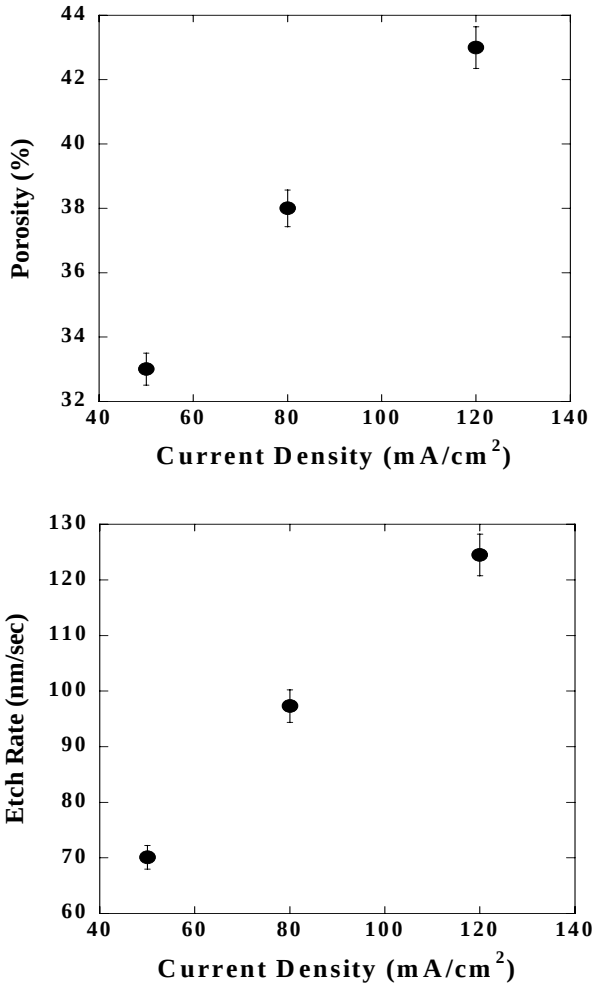

Figure 1.3. PSi porosity (top) and etch-rate (bottom) dependence versus current density for p-type crystalline silicon substrate anodized in 35% hydrofluoric acid concentration electrolyte

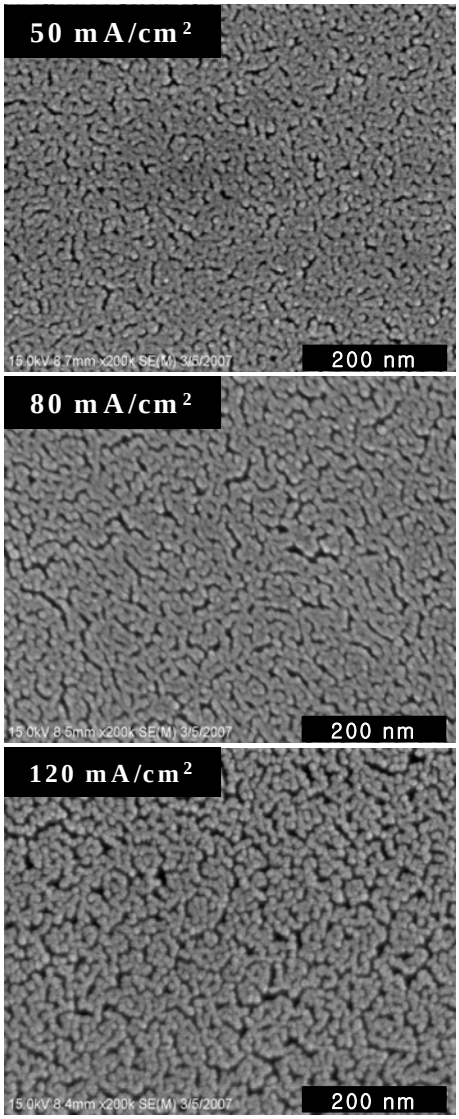

Figure 1.4. Surface FE-SEM images of PSi with different current densities

1.3.2 Concentration of Etching Solution and Anodization Time

The composition of HF solution determines the etching process. In the anodization of PSi, hydrofluoric acid with ethanol as an etchant solution is typically used. When aqueous HF solutions are used in the formation of PSi, the hydrogen bubbles evolved stick to the surface. To improve the surface uniformity in PSi, the hydrogen bubbles must be removed. The ethanol solution ensures the uniformity of the PSi by removing the hydrogen bubbles from the PSi surface and enables the HF penetration into the pores.

Concentration of the hydrofluoric acid and etching time determine the PSi porosity and thickness. For given time, porosity is inversely proportional to the HF concentration [34]. Therefore, lowering the HF concentration increase in the PSi porosity. Since PSi thickness is related to HF concentration, an increase in the HF concentration cause an increase in the PSi thickness which in turn leads to a reduction of the PSi porosity for a fixed time [35].

As the etching time is varied, the thickness and porosity of the PSi layers change. Figure 1.5 shows that the thickness of the PSi layer as a function of anodization time [36] for a p-type substrate that is etched at a constant current density of 50 mA/cm^2 in a 35% hydrofluoric acid solution. The figure shows a linear relationship between the etching time and the thickness of the PSi layer.

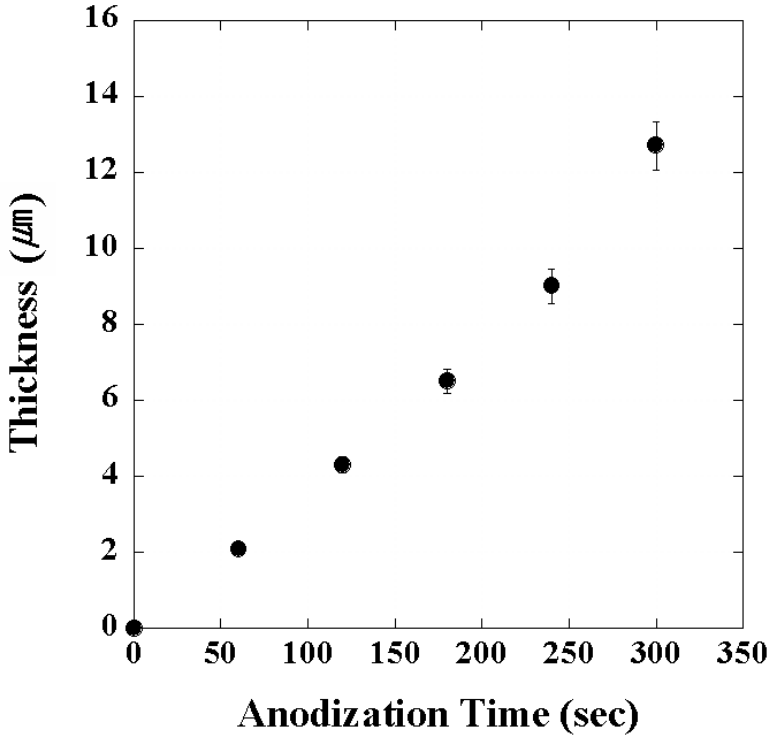

Figure 1.5. Thickness of PSi with different anodization time for p-type crystalline silicon substrates anodized at a fixed current density of 50 mA/cm^2.

1.4 Properties of Porous Silicon

Some properties, such as porosity, refractive index, thickness, pore diameter, multi-structures, and optical properties, are strongly dependent on the anodization process parameters. These parameters include HF concentration, current density, anodization time, and silicon wafer type and resistivity.

1.4.1 Substrate Properties

Silicon substrates are identified by properties such as dopant type (i.e., n-type or p-type), substrate resistivity, dopant concentration, and substrate orientation. During anodization, dopant of the silicon substrate plays a significant role. Since holes (h^+) are the most important element in the chemical reaction leading to the formation of PSi, the use of p-type wafer is the most popular. However, n-type wafer can be used with external illumination.

Substrate resistivity determines the achievable thickness of PSi. For example, a very low resistivity wafer (<0.01 Ω-cm) is capable of producing thicker PSi compared to a wafer with a higher resistivity (>10 Ω-cm) under same anodization conditions.

The morphology of the PSi can be grouped into four categories based on doping concentration: p, p^+, p^{++}, n, n^+, and n^{++} [33]. For p-type silicon wafer, the pore diameters and interpore spacing are very small (20-100 Å). As the dopant concentration increases, the pore diameter and spacing increase slightly (100-1000 Å). For n-type silicon, the pore diameters are considerably larger than those of the p-type substrate.

Substrate orientation is also important in the structure of the PSi morphology. The main pore growth direction is essntially the same irrespective of the substrate orientation, dopant concentration or anodization conditions [37-38].

1.4.2 Porosity

The most important quantity when characterizing a porous materials is the porosity which is defined as the ratio of the empty pore volume to the total volume. The porosity of a PSi can be calculated gravimetrically using following equation [39]:

$$\textbf{Porosity (\%)} = \frac{m_1 - m_2}{m_1 - m_3}$$

Where m_1 is the mass of the initial silicon wafer in grams, m_2 is the mass of the silicon wafer after anodization in grams, m_3 is the mass of the silicon wafer after dissolution of the porous layer in grams. The dissolution of PSi is performed using a 0.1 M aqueous solution of sodium hydroxide (NaOH).

This gravimetric method is applicable in cases where the PSi layer is sufficiently thick (> 5 ㎛). The differnce in masses is larger than the amount of error induced in the measurements. However, when the PSi layer is thin (< 200 nm), the mass difference is the same order of magnitude as the error in measurements, and the porosity value obtained is unreliable.

1.4.3 Thickness

The thickness of PSi can be determined using either non-destructive or destructive techniques. One non-destructive technique is the use of an ellipsometer which requires the extensive understanding of the refractive index. For the PSi samples, the index is difficult to determine since the porosity varies vertically with depth. There are two available destructive techniques that can be used with significant ease. One determines the approximate PSi thickness using following equation:

$$\textbf{Thickness} = \frac{M_1 - M_3}{S \cdot d}$$

Where M_1 is the mass of the original silicon wafer, M_3 is the wafer with anodized material removed, S is the area of the PSi sample, and d is the density of the silicon substrate.

The second and more accurate technique uses a field emission scanning electron microscope (FE-SEM) after scribing the PSi sample to visualize a cross sectional view. This technique can resolve the thickness of PSi to a few nanometers as well as provide additional information on the PSi morphology.

1.4.4 Refractive Index

The refractive index is one of the important property of PSi. This property controls the reflection and transmission of waves incident on the PSi-air interface. There are many approximations that predict the refractive index of PSi based on porosity [40-41]. However, none of them covers the entire porosity range with the same degree of high accuracy.

The refractive index of PSi is calculated by using the Bruggeman approximation as described below :

$$(1\text{-}P)\frac{\varepsilon_{Silicon}+\varepsilon_{porous\ silicon}}{\varepsilon_{Silicon}+2\varepsilon_{porous\ silicon}}+(P)\frac{\varepsilon_{air}+\varepsilon_{porous\ silicon}}{\varepsilon_{air}+2\varepsilon_{porous\ silicon}}=0$$

where P is the porosity of porous silicon, $\varepsilon_{silicon}$ is the dielectric constant of silicon, ε_{air} is the dielectric constant of air, and $\varepsilon_{porous\ silicon}$ is the dielectric constant of porous silicon.

1.4.5 Surface Area

PSi has a very large surface area (1-500 m^2/cm^3) defined as the accessible area of solid surface per unit of material. This characteristic gives PSi the ability to act as a host to many inorganic and organic materials, resulting in many potential applications. A standard method used to measure the specific surface area is the BET (Brunauer-Emmett-Teller) method [42]. This method is based on the adsorption of gases by the porous structure.

1.4.6 Optical Properties and Bench Setup

The optical properties of PSi are discussed in a wide spectral range from the infrared to the ultraviolet. PSi has two optical properties such as photoluminescence (PL) for n-type with external illumination (300 W tungsten lamp) and optical reflectivity (Fabry-Pérot fringe) for p-type as shown in Figure 1.6. The ability of PSi to emit and reflect in visible range is the most attractive property of the material. One explanation for the visible luminescence is based on the nanometer-size crystalline structure for PSi [31,43-45].

PL spectrum of PSi has been obtained with Ocean Optics LS-1 (blue LED). Optical reflectivity spectrum of PSi showing Febry-Pérot fringe pattern has been measured by using tungsten-halogen lamp and an Ocean Optics S2000 charge-coupled detector (CCD) spectrometer fitted with a fiber optic input. The reflected light collection end of the fiber optic is positioned at the focal plane of the optical microscope as described in Figure 1.7.

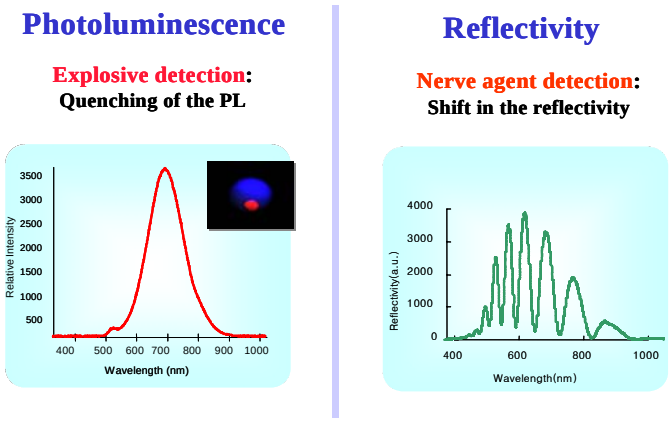

Figure 1.6. Optical properties of porous silicon; photoluminescence (left) and reflectivity (right)

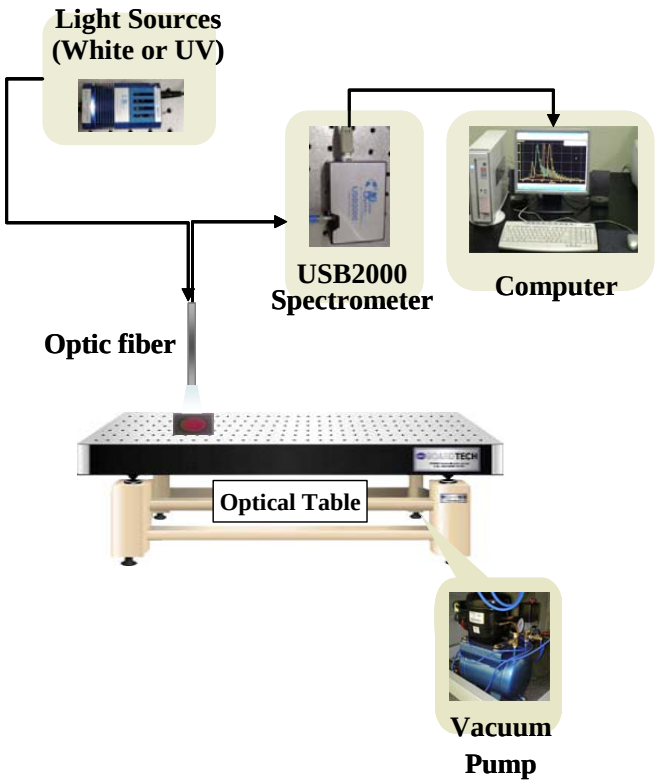

Figure 1.7. Optical bench setup for obtaining the optical properties of porous silicon

1.5 Stabilization of Porous Silicon

1.5.1 Oxidation

Freshly etched PSi is covered by hydrogen atoms that are covalently attached to the silicon surface. The attached hydrogen species are in the form of Si-H, Si-H_2, and Si-H_3 and can be characterized by fourier transform infrared spectroscopy (FT-IR). The hydrogen covered surface provides a good electron passivation layer. After the PSi is exposed to air, a slow oxidation of the surface takes place. Replacing the hydrogen by oxygen (oxidation) is one of the most common ways to passivate the electronic properties of PSi. Oxidation can be occurred by exposing the sample to air, anodic oxidation in a non-fluoride electrolyte [46], chemical oxidation [47], or thermal oxidation [48-51]. Thermal oxidation is the most commonly used because it produces reproducible and controlled oxide layers of good quality. Thermal oxidation is the method used to passivate or oxidize the PSi structure. Thermal oxidation performed in a furnace at temperatures between 300 ~ 600℃ results in the loss of hydrogen and the production of PSi with poor electronic properties. The solution is to oxidize at higher temperatures resulting in better passivation, but running the risk of converting the PSi structure into silicon dioxide (SiO_2). Figure 1.7 shows experimental setup for the thermal oxidation and comparison of FT-IR spectra between freshly etched PSi and thermally oxidized PSi.

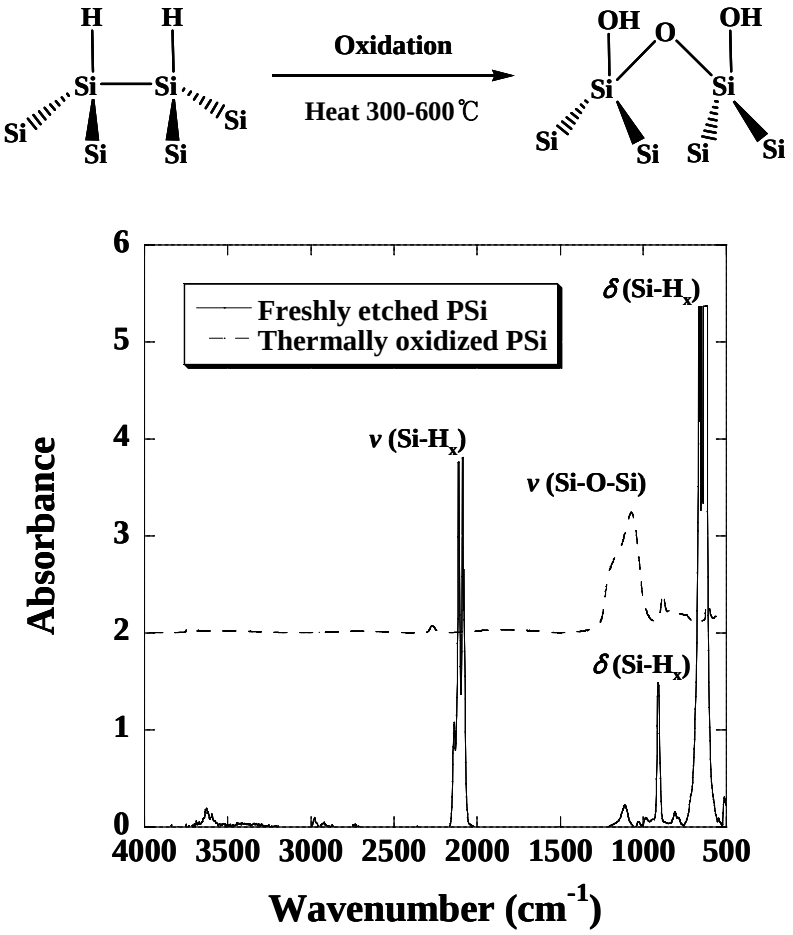

Figure 1.8. Chemical scheme for the thermal oxidation (top) and comparison of FT-IR spectra between freshly etched PSi and thermally oxidized PSi (bottom)

1.5.2 Surface-Derivatization (Hydrosilylation)

The hydride-terminated surfaces in general offer many advantages, including their excellent chemical homogeneity (>99% H termination) and strong FT-IR stretching modes (~2100 cm^{-1}) which can provide information as to surface flatness and makeup. The use of the Si-H terminated surface for many applications is precluded due to its propensity to oxidize, but it can be easily handled in air for minutes to tens of minutes without measurable degradation. Rapid and efficient preparation of Si-H hydride-terminated flat surfaces has been known for over 10 years [52-53].

Hydrosilylation involves the insertion of an unsaturated bond onto a silicon-hydride group. Alkene and alkyne hydrosilylation on Si-H-terminated surfaces yield alkyl and alkenyl termination, respectively as shown in Figure 1.9.

One of the hydrosilylation methods is the thermally induced hydrosilylation. Thermally induced hydrosilylation of alkenes and an alkyne has been applied to Si-H-terminated PSi surface [54-56]. It is initially reported that refluxing PSi for 18-20 h at 110-180℃ in an aliphatic alkyne or alkene yields alkyl monolayers [54]. Futher investigation of thermally induced hydrosilylation of 1-dodecene on PSi is examined, and derivaized surfaces are characterized by FT-IR as shown in Figure 1.10.

Another of the hydrosilylation method is the photochemical hydrosilylation using UV irradiation. The UV irradiation can promote hydrosilylation of unsaturated compounds [57] due to homolytic cleavage of Si-H bonds. UV photoinduction, however, takes place at room temperature and thus a way to avoid thermal input that can be harmful to delicate or small features on a silicon chip.

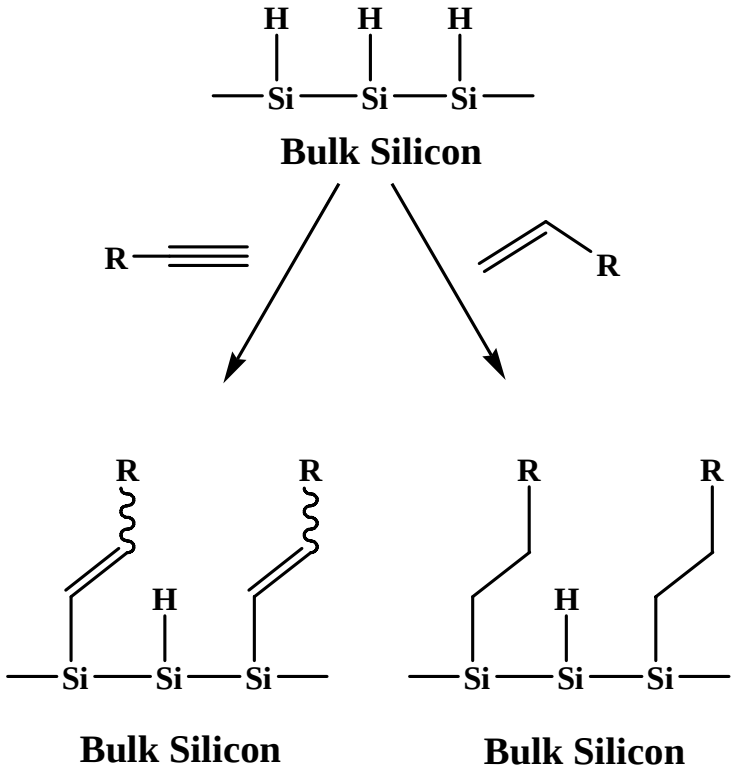

Figure 1.9. Schematic hydrosilylation chemistry. Hydrosilylation involves the insertion of an unsaturated bond, alkyne or alkene, into Si-H bond, resulting in Si-C bond formation and formation of alkenyl or alkyl groups, respectively.

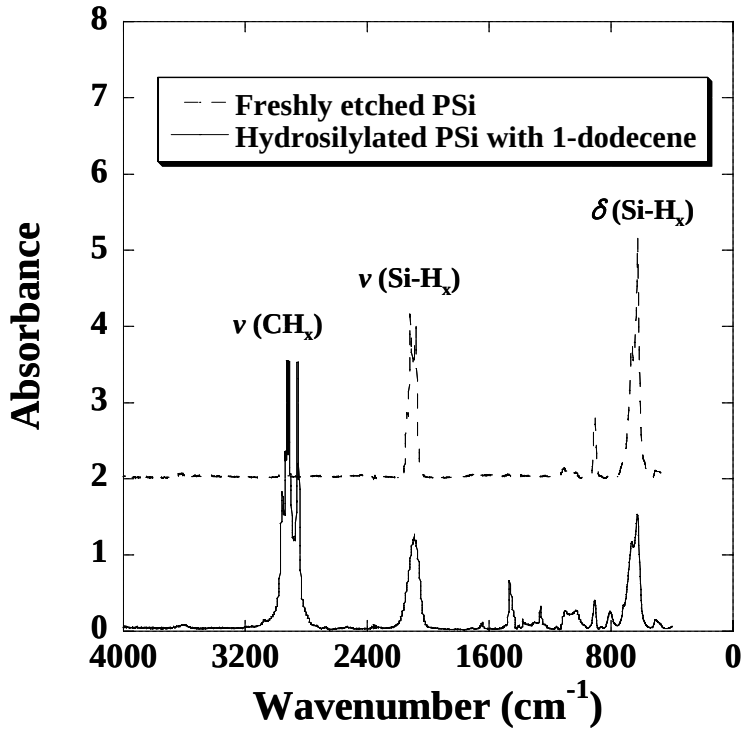

Figure 1.10. Comparison of FT-IR spectra between freshly etched PSi and hydrosilylated PSi with 1-dodecene

1.6 Multi-structures of Porous Silicon

1.6.1 Theory of Multilayer Structures

The multilayer structures based on PSi open the door for a variety of new applications. Some pf the possilble application of these structures are in the areas of interference filters [58], waveguides [59], photodiode [60], and microcavities [61]. For all these application, strict control over the reflectance and transmission properties of the PSi multilayer is required.

The advantage of a dielectric multilayer structure is the multiple interference a light beam undergoes when it is reflected at each interface. A qualitative representation of this is described in Figure 1.11, where interference from a single film is compared to a multilayer structure. The light beam is reflected at each interface between the two materials containing two different refractive indices. In a single layer (neglecting the multiple reflections of light between interface) the reflected light is composed of two reflectivity beams, one across the air-film interface and the other across the film-substrate interface (in Figure 1.11A). In the case of the multilayer structure, the reflected light is a combination of all the reflectivity beams at each of the interface (in Figure 1.11B, 5 reflected beams are observed). By simply choosing the thickness and refractive index of each of the layers, it is possible to control the constructive and destructive interference of the light across a multilayer structure, which dictates its reflectivity spectrum.

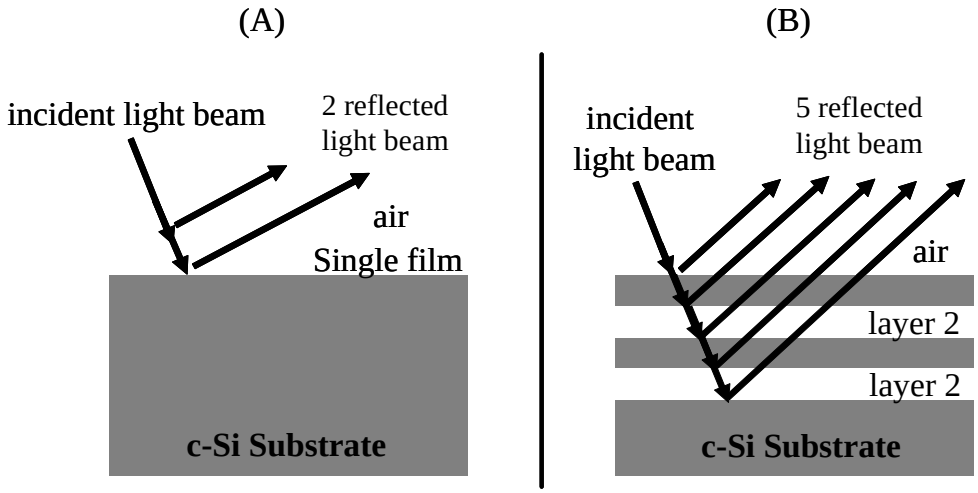

Figure 1.11. Multiple interference of thin film structure. Representation of the reflection and transmission of light by a single (A) and a multilayer structure (B)

1.6.2 Properties of Multilayer Structures

PSi multilayers consist of alternating layers of different refractive index. PSi multilayer structures are easily manufactured using a periodic current density square waveform for distributed Bragg reflectors (DBR) [62-66] and sinusoidal waveform for rugate [67-70] during the electrochemical etching process as described in Figure 1.12. The difference in porosity profile, corresponding to a variation in current density, is attributed to a difference in refractive index.

Multistructured PSi, DBR or rugate, exhibit unique optical properties providing the reflection of a specific wavelength in the optical reflectivity spectrum. This reflective wavelength can be controlled by tuning of many etching parameters and can appear anywhere in the visible range. Figure 1.13 shows a demonstration for the fabrication of specific reflectors or filters in full color.

Figure 1.14 shows a cross-sectional SEM image of a PSi multilayer where the different layers present alternating porosity (refractive index) layers. The two parameters that govern the optical properties of the multilayers are the thickness and refractive index of the alternating layers, so control over these properties is critical. Other properties like interface roughness and depth homogeneity also affect the quality of the multilayer structures.

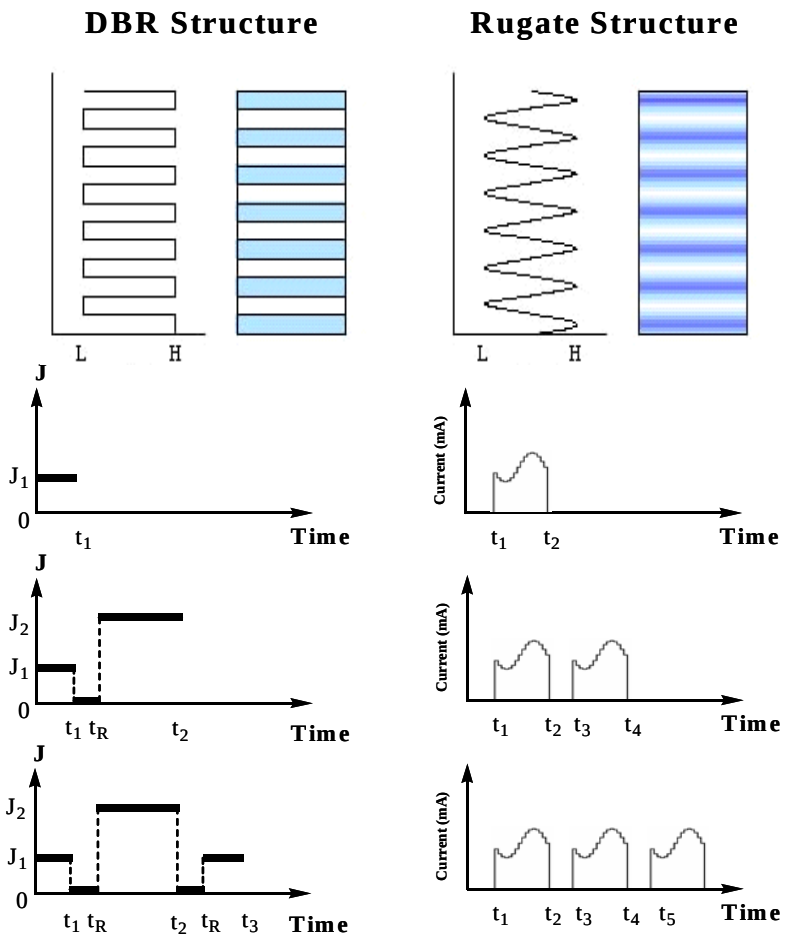

Figure 1.12. Schematic pictures on the formation of PSi multilayer structures. By pulsing between two different current densities, two different porosity PSi layers can be formed (left) and step-functions used to approximate the sinusoidal variation of refractive index (right).

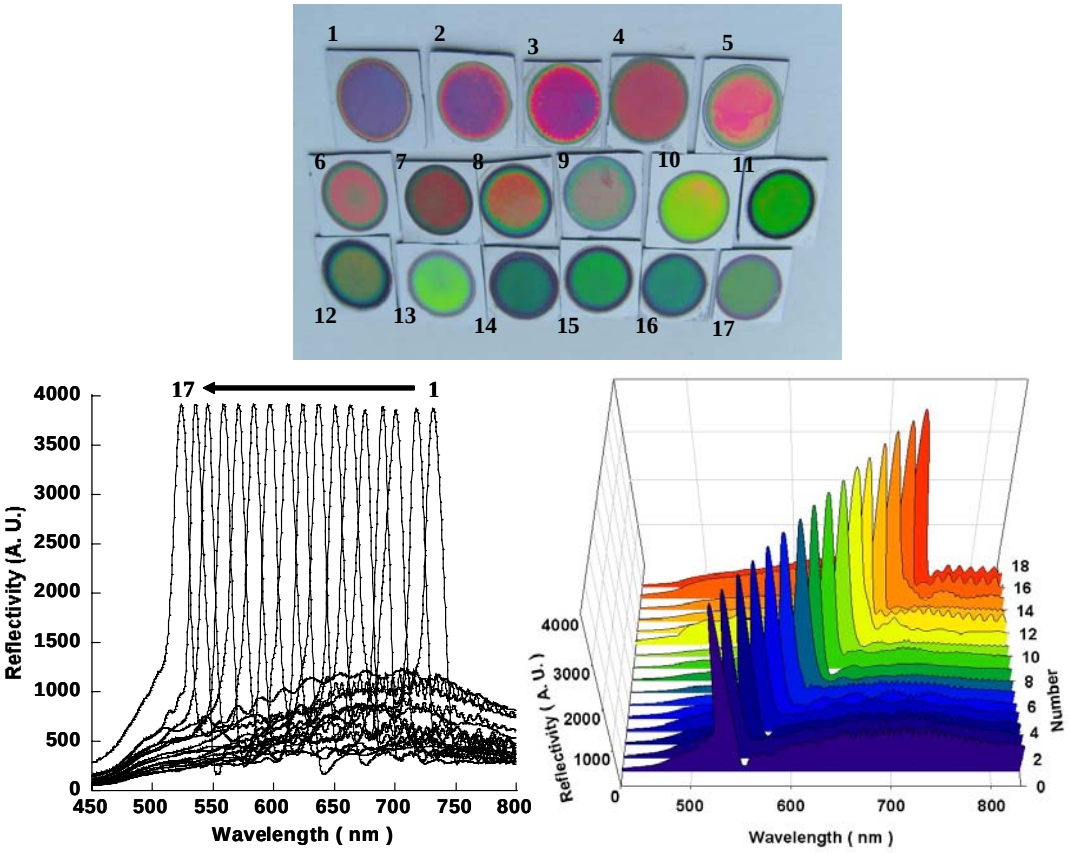

Figure 1.13. Photo (top) and optical reflectivity spectra (bottom) of specific reflectors or filters anywhere in the visible range. This reflective wavelength can be controlled by tuning many etching parameters.

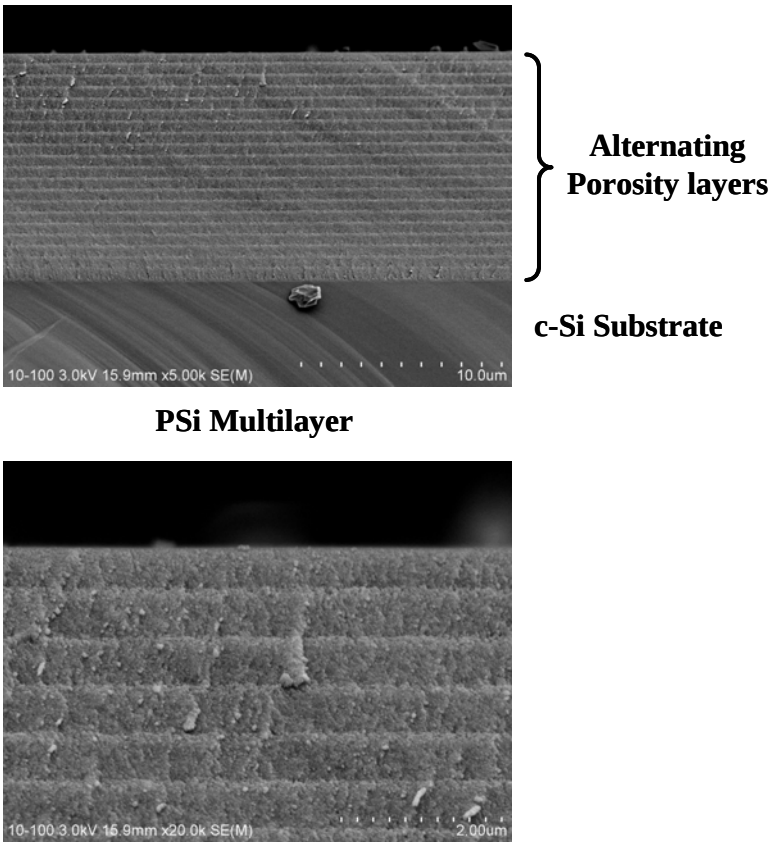

Figure 1.14. Cross-sectional SEM images of PSi multilayer where the different layers present alternating porosity (refractive index) layers

1.7 Instruments and Data Acquisitions

FT-IR is a powerful technique that can determine the chemical species present in the material. This technique measures the amount of radiation absorbed by the chemical bonds in the material as the radiation wavelength is varied through the infrared region. Specific chemical bonds will absorb the radiation at different frequencies depending on the strength of the bond. The different area where the bonds absorb serve as fingerprints in identifying the chemical species present. In this works, FT-IR spectra were acquired with a Nicolet model 5700 FT-IR instrument in the diffuse reflectance mode (Spectra-Tech diffuse reflectance attachment). The FT-IR sample compartment was purged with nitrogen before each acquisition. In this study, scanning electron microscope (SEM) is used extensively to provide real pictures of the micrometer and nanometer structure of PSi samples. The morphology of PSi is observed with cold field emission SEM (FE-SEM, S-4800, Hitachi). Another technique available with the SEM is energy dispersive X-ray spectrometry (EDS). This technique provides a spatially sensitive, non-destructive, and easy way to qualitatively determine the elemental composition of the PSi samples. EDS collects the emitted X-rays and distinguishes between emit different family of lines at particular energies. Photoluminescence of PSi is measured by Perkin-Elmer luminescence spectrometer LS 50B and Ocean Optics LS-380 (UV or blue LED) spectrometer. In order to investigate how PSi structures interact with light, interferometric reflectance spectra are recorded by using an Ocean Optics S2000 spectrometer fitted with a bifurcated fiber optic probe. Spectra were recorded with a CCD detector in the wavelength range of 400～1200 nm. The illumination of the surface as well as the measurement of the reflected light was performed along an axis coincident with the surface normal.

1.8 references

[1] A. Uhlir, *Bell Synt. Tech. J.* **35**, 333 (1956).

[2] D. R. Turner, *J. Electrochem. Soc.* **105**, 402 (1958).

[3] Y. Arita, K. Kato, and T. Sudo, *IEEE T. Electron Dev.* **24**, 757 (1977).

[4] T. Unagami and K. Kato, *Jpn. J. Appl. Phys.* **16**, 1635 (1977).

[5] K. Imai, *Solid State Electron* **24**, 159 (1981).

[6] F. Otoi, K. Anzai, H. Kitabayashi, K. Uchiho, and Y. Mizokami, *J. Electrochem. Soc.* **131**, C319 (1984).

[7] L. T. Canham, *Appl. Phys. Lett.* **57**, 1046 (1990).

[8] A. G. Cullis and L. T. Canham, *Nature* **353**, 335 (1991).

[9] Z. Sui, P. P. Leong, I. P. Herman, G. S. Higashi, and H. Temkin, *Appl. Phys. Lett.* **60**, 2086 (1992).

[10] C. Delerue, G. Allan, and M. Lannoo, *Phys. Rev. B* **48**, 11024 (1993).

[11] F. Koch, V. Petrova-koch, T. Muschik, A. nikolov, and V. Gavrilenko, *Mater. Res. Soc. Symp. Proc.* **298**, 319 (1993).

[12] E. J. Lee, T. W. Bitner, J. S. Ha, M. J. Shane, and M. J. Sailor, *J. Am. Chem. Soc.* **118**, 5375 (1996).

[13] J. M. Buriak and M. J. Allen, *J. Am. Chem. Soc.* **120**, 1339 (1998).

[14] A. Richter, P. steiner, F. Kozlowski, and W. Lang, *IEEE Electron Device Lett.* **12**, 691 (1991).

[15] K. D. Hirschmann, L. Tsybeskov, S. P. Duttagupta, and P. M. Fauchet, *Nature* **384**, 338 (1996).

[16] C. Mazzoleni and L. Pavesi, *Appl. Phys. Lett.* **67**, 2983 (1995).

[17] G. Smestad, M. Kunst, and C. Vial, *Sol. Energy Mater. Sol. Cells* **26**, 277 (1992).

[18] J. M. Lauerhaas and M. J. Sailor, *Science* **261**, 1567 (1993).

[19] H. Sohn, S. Letant , M. J. Sailor, and C. Trogler, *J. Am. Chem. Soc.* **122**, 5399 (2000).

[20] S. Letant and M. J. Sailor, *Adv. Mater.* **13**, 355 (2001).

[21] S. Chan, S. R. Horner, P. M. Fauchet, and B. L. Miller, *J. Am. Chem. Soc.* **123**, 11797 (2001).

[22] H. Sohn, R. M. Calhoun, M. J. Sailor, and W. C. Trogler, *Angew. Chem. Int. Ed.* **40**, 2104 (2001).

[23] H. Sohn, M. J. Sailor, D. magde, and W. C. Trogler, *J. Am. Chem. Soc.* **125**, 3821 (2003).

[24] X, Li, J. L. Coffer, Y. D. Chen, R. F. Pinizzotto, J. Newey, and L. T. Canham, *J. Am. Chem. Soc.* **120**, 11706 (1998).

[25] N. Koshida, T. Nakajima, M. Yoshiyama, K. Ueno, T. Nakagawa, and H. Shinoda, *Mater. Res. Soc. Symp. Proc.* **536**, 105 (1999).

[26] T. E. Bell, P. T. J. Gennissen, D. Demunter, and M. Kuhl, *J. Micromech. Microeng.* **6**, 361 (1996).

[27] V. G. Zubko , T. L. Smith, A. N. Witt, *Astrophys. J.* 501 (1998).

[28] V. P. Parkhutik, E. Matveeva, R. Perez, J. Alamo, and D. BeltraÂn, *Mater. Sci. Engn. B* **69-70**, 53 (2000).

[29] V. P. Bondarenko, Y. V. Bogatirev, J. P. Colinge, L. N. Dolgyi, A. M. Dorofeev, and V. A. Yakovtseva, *IEEE. Trans. Nucl. Sci.* **44**, 1719 (1997).

[30] V. P. Parkhutik and L. T. Canham, *Phys. Stat. Sol. A* **182**, 591 (2000).

[31] V. Lehmann and U. Gösele, *Appl. Phys. Lett.* **58**, 856 (1991).

[32] M. J. Sailor, J. L. Heinrich, and J. M. Lauerhaas, *Stud. surface Sci. Cat.* **103**, 209 (1996).

[33] R. L. Smith and S. D. Collins, *J. Appl. Phys.* **71**, R1 (1992).

[34] S. M. Hossain, J. Das, S. Chakraborty, S. K. Dutta, and H. Saha, *Semicon. Sci. Tech.* **17**, 55 (2002).

[35] I. K. Itotia and R. F. Drayton, *IEEE Antenn. Propag. Soc.* **2**, 663 (2003).

[36] A. Halimaoui, Porous Silicon Science and Technology, edited by J. C. Vial and J. Derrien, Springer-Verlag, New York, pp. 33, (1995).

[37] M. Christopersen, J. Carstensen, and H. Foll, *Phys. Stat. Sol. A* **182**, 601 (2000).

[38] S.-F. Chuang, S. D. Collins, and R. L. Smith, *Appl. Phys. Lett.* **55**, 675 (1989).

[39] D. Brumhead, L. T. Canham, D. M. Seekings, and P. J. Tufton, *Electrochi. Acta*. **38**, 191 (1993).

[40] D. J. Bergman, *Phys. Rep. C* **43**, 377 (1978).

[41] H. Looyenga, *Physica* **31**, 401 (1965).

[42] S. Brunauer, P. H. Emmett, and E. Teller, *J. Am. Chem. Soc.* **60**, 309 (1938).

[43] S. Sawada, N. Hamada, N. Ookubo, *Phys. Rev. B* **49**, 5236 (1994).

[44] A. J. Read, R. J. Needs, K. J. Nash, L. T. Canham, P. D. J. Calcott, and A. Qteish, *Phys. Rev. Lett.* **69**, 1232 (1992).

[45] Y. Kanemitsu, H. Uto, Y. Masumoto, T. Futagi, and H. Mimura, *Phys. Rev. B* **48**, 2827 (1993).

[46] M. A. Hory, R. Herino, M. Ligeon, F. Muller, F. Gaspard, I. Mihalcescu, and J. C. Vial, *Thin Solid Films* **255**, 200 (1995).

[47] A. Nakahima, T. Itakura, S. Watanabe, and N. Nakayama, *Appl. Phys. Lett.* **64**, 46 (1992).

[48] J. Yan, S. Shih, K. H. Jung, D. L. Kwong, M. Kovar, J. M. White, B. E. Gnade, and L. Magel, *Appl. Phys. Lett.* **64**, 1374 (1994).

[49] L. Walter, S. Peter, K. Frank, and R. Peter, *Thin Solid Films* **255**, 224 (1995).

[50] K. D. Hirschmann, L. Tsybeskov, S. P. Duttagupta, and P. M. Fauchet, *Nature* **384**, 338 (1996).

[51] A. E. Pap, K. Kordás, T. F. George, and S. Leppävuori, *J. Phys. Chem. B* **108**, 12744 (2004).

[52] G. S. Higashi, Y. J. Chabal, G. W. Trucks, and K. Raghavachari, *Appl. Phys. Lett.* **56**, 656 (1990).

[53] G. S. Higashi, R. S. Becker, R. S. Chabal, and A. J. Becker, *Appl. Phys. Lett.* **58**, 1656 (1991).

[54] J. E. Bateman, R. D. Eagling, D. R. Worrall, B. R. Horrocks, and A. Houlton, *Angew. Chem. Int. Ed. Engl.* **37**, 2683 (1998).

[55] R. Boukherroub, S. Morin, D. D. M. Wayner, F. Bensebaa, G. I. Sproule, J.-M. Baribeau, and D. J. Lockwood, *Chem. Mater.* **13**, 2002 (2001).

[56] J. E. Bateman, R. D. eagling, B. R. Horrocks, and A. Houlton, *J. Phys. Chem. B* **104**, 5557 (2000).

[57] I. Fleming, In Comprehensive Organic Chemistry, N. Jones, Ed, Pergamon, New York, **3**, 568 (1979).

[58] M. G. Berger, C. Dieker, M. Thonisen, L. Vescan, H. Luth, and H. Munder, *J. Phys. D* **27**, 1333 (1994).

[59] A. Loni, L. T. Canham, M. G. Berger, R. Arens-Fisher, H. Munder, H. Luth, H. F. Arrand, and T. M. Benson, *Thin Solid Films* **276**, 143 (1996).

[60] M. Hruger, M. G. Berger, M. Marso, W. Reetz, T. Eickhoff, R. Loo, L. Vescan, M. Thonissen, H. Luth, R. Arens-Fisher, S. Hilbrich, and W. Theiss, *Jpn. J. Appl. Phys*. **36**, L24 (1997).

[61] L. Pavesi, La Rivista del Nuovo Cimento, della Societá Italiana di Fisica, dited by S. Frabetti, P. Marangon, M. Missiroil, and P. Rucci, Bologna, pp. 1, (1997).

[62] C. Mazzoleni and L. Paves. *Appl. Phys. Lett*. **67**, 2983 (1995).

[63] M. G. Berger, R. Arens-Fischer, M. Thonisson, M. Kruger, S. Billat, H. Luth, S. Hilbrich, W. Theiss, and P. Grosse, *Thin Solid Films* **297**, 237 (1997).

[64] M. Cazzanelli, C. Vinegoni, and L. Pavesi. *J. Appl. Phys*. **85**, 1760 (1999).

[65] V. Lehmann, R. Stengl, H. Reisinger, R. Detemple, and W. Theiss. *Appl. Phys. Lett*. **78**, 589 (2001).

[66] V. Agrawal and J. A. del Rio, *Appl. Phys. lett*. **82**, 1512 (2003).

[67] B.G. Bovard, *Appl. Opt*. **32**, 5427 (1993).

[68] A. J. Nolte, M. F. Rubner, and R. E. Cohen, *Langmuir* **20**, 3304 (2004).

[69] J. R. Dorvee, A. M. Derfus, S. N. Bhatia, and M. J. Sailor, *Nat. Mater.* **3**, 896 (2004).

[70] S. Ilyas, T. Böcking, K. Kilian, P.J. Reece, J. Gooding, K. Gaus, and M. Gal, *Opt. Mater.* **29**, 619 (2007).

Chapter Two
Detection of Toxic Organophosphate Nerve Agents Using DBR Porous Silicon Interferometer

2.1 Introduction

Photonic crystals of porous silicon (PSi) have been a topic of interest, because of their use in chemical and biological sensors, biomaterials, and optical devices [1-4]. Multistructured porous silicons such as distributed Bragg reflectors (DBR) PSi and Rugate PSi exhibit unique optical properties providing the reflection of a specific wavelength in the optical reflectivity spectrum. Detection of chemical warfare agents is of great interest since they are highly toxic and are a great international concern. Dimethyl methylphosphonate (DMMP), triethylphosphate (TEP), and diethyl ethylphosphonate (DEEP) are a simulant for G-type nerve agents. These compounds are chemically similar nerve agents such as sarin, soman and tabun. Sarin, a G-type nerve agent, has lethality depending on both concentration and exposure time. The LCt_{50} for sarin by inhalation of the vapor form is 100 milligrams of sarin per cubic meter of air for one minute [5]. The main method currently used to detect nerve agents is based on a surface acoustic wave (SAW) device [6,7]. Other methods using enzymes [8], single-walled carbon nanotubes [9], metal oxides [10], and organic polymers [11] have been recently reported. PSi is also an alternative method to detect chemical nerve agents [1,12].

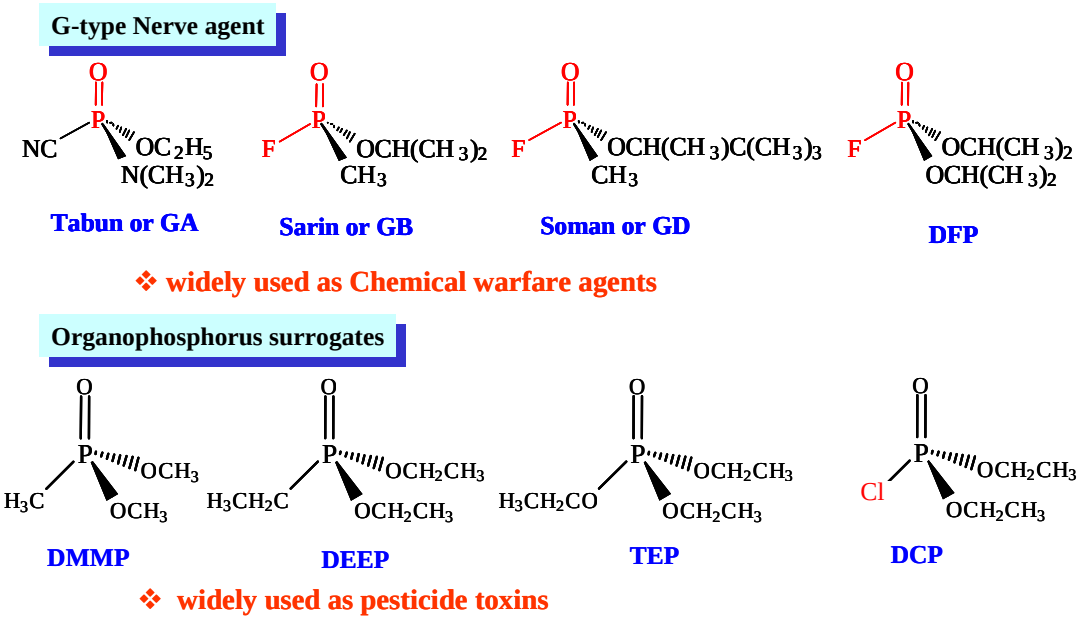

Figure 2.1. Structures of G-type nerve agents and organophosphate nerve agent simulants

2.2 Experiments

2.2.1 Sample Preparation

Porous silicon samples were prepared by electrochemical etch of heavily doped p^{++}-type silicon wafers (boron doped, polished on the <100> face, resistivity; 0.8-1.2 mΩ·cm, Siltronix, Inc.). The etching solution consists of a 3:1 volume mixture of aqueous 48% hydrofluoric acid (Aldrich Chemicals) and absolute ethanol (Aldrich Chemicals). Galvanostatic etching was carried out in a Teflone cell applying 20 cycles of a two-electrode configuration. DBR PSi has been prepared by using a square wave current between 5 $mA \cdot cm^{-2}$ for 90 sec and 50 $mA \cdot cm^{-2}$ for 3 sec. TEP, DMMP, and DEEP were purchased from Aldrich Chemicals and used without any purification.

2.2.2 Instrumentation and Data Acquisition

Optical reflectivity spectra were measured using a tungsten-halogen lamp and an Ocean Optics S2000 CCD spectrometer fitted with a fiber optic input. The reflected light collection end of the fiber optic was positioned at the focal plane of the optical microscope. Scanning electron microscope (SEM) images were obtained by a cold field emission scanning electron microscope (FE-SEM, S-4700, Hitachi).

2.3 Results and Discussion

2.3.1 Optical Structure of DBR PSi Interferometer

DBR PSi containing two distinct porosities has been successfully prepared using a periodic galvanostatic electrochemical etch by applying a square wave current density. The wavelength of a peak in the reflectivity spectrum is given by the following equation:

$$m\lambda_{Bragg} = 2n_i d_i$$

where m is the spectral order of the optical fringe, λ the wavelength, n_i the refractive index of the film, and d_i its thickness. Photonic feature of DBR PSi results in a mirror with high reflectivity at 520 nm with sidelobes around the reflectance peak. The reflection band of DBR PSi has the full-width at half-maximum (FWHM) of 20 nm indicates that the FWHM of these reflection bands is much narrower than that of fluorescence spectrum obtained from a fluorescent organic molecules or quantum dot. SEM images shown in Figure 2.2 have been obtained by a cold field emission scanning electron microscope. The cross-sectional image of DBR PSi shown illustrates that the multilayer of DBR PSi has a depth of a few microns. A repeating etch process results in two distinct refractive indices.

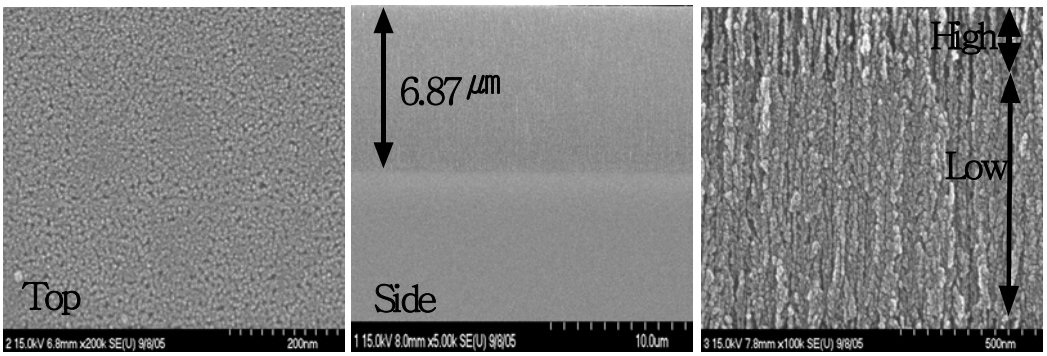

Figure 2.2. SEM images of DBR PSi interferometer. From left; top view of DBR PSi, middle; cross-sectional of SEM image of DBR PSi indicating that the thickness of DBR PSi is about 6.87 ㎛, right; detailed cross-sectional SEM image of porous nanostructure in DBR PSi. Low current (LC) and high current (HC) indicate two distinct refractive index, respectively.

2.3.2 Data Analysis for Sensing Nerve Gases

DBR PSi samples are placed in an exposure chamber fitted with an optical window. The samples are exposed to a flux of DMMP (partial pressure of 0.22 torr or 290 ppm) in air with a flow rate of 5 L/min. Figure 2.3 shows reflectivity spectra recorded every 15 sec, *in situ*, while exposing the detector to the organophosphate vapors. Capillary condensation causes the reflectivity spectrum of the DBR PSi to shift to longer wavelengths by about 10 nm for 1 min due to an increase in reflective indices of the porous medium. The 10 nm and 25 nm red-shift of reflectivity has been observed in the case of DEEP or TEP vapor (135 ppm). Real-time detection shown in Figure 2.4 has been achieved by the monitoring of intensity of reflected light at 520 nm from DBR PSi for three exposure/evacuation cycles using TEP analyte at their saturation vapor pressure. The intensity of reflection has been decreased about 25% for 10 sec of exposure. A reversible response is observed for 15 sec.

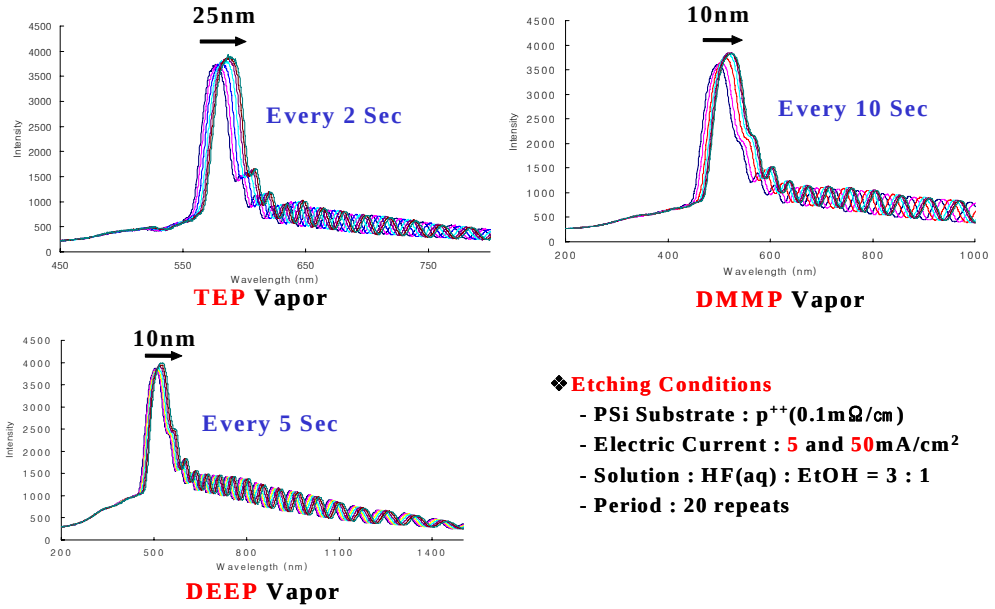

Figure 2.3. Reflectivity spectra of DBR PSi were recorded every 15 sec for 1 min, *in situ*, under the exposure of a flux of (a) TEP (135 ppm), (b) DMMP (290 ppm), (c) DEEP (135 ppm) in air with a flow rate of 5 L/min. A red-shift of (a) 25 nm, (b) 10 nm, and (C) 10 nm is observed, respectively.

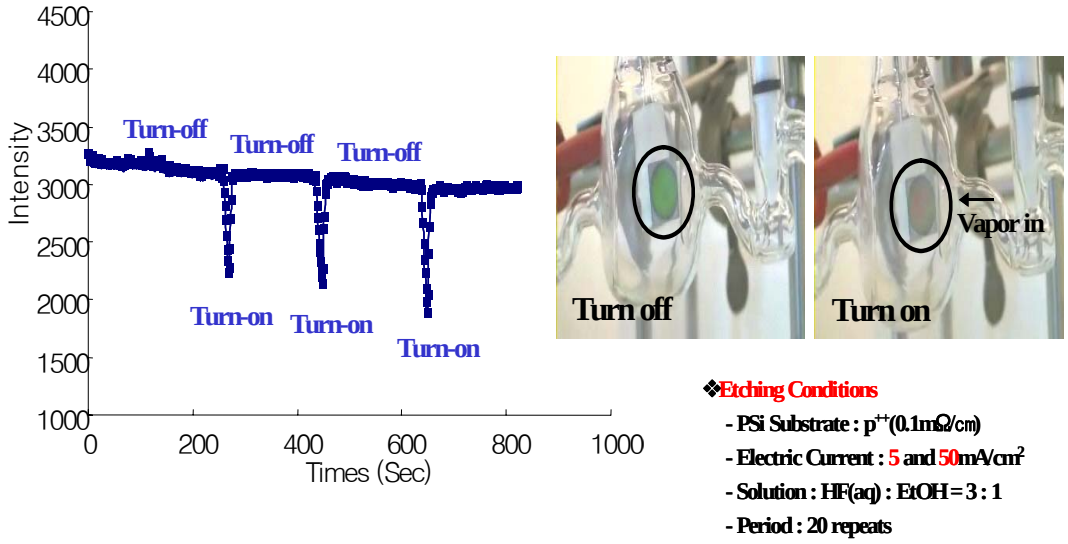

Figure 2.4. Plot for dosing response showing the detection of TEP vapor based on DBR PSi and photograph for sensing of TEP vapor displays color change of DBR PSi as vapor in and out.

2.3.3 Detection Limit

DMMP is a stimulant for G-type nerve agents such as sarin. Vapor of sarin has a lethality that is indicated by both concentration and exposure time. If a group of people breathed a concentration of 100 mg of sarin per cubic meter of air for one minute, this would be a lethal dose for 50% of a group. At 1 mg/m^3=0.17 ppm for sarin, 100 mg/m^3 is equal to 17 ppm [5]. As shown in Figure 2.5, The detection limit of DMMP (1.5 ppm) using DBR PSi is 8.8 mg/m^3 for 1 min. This result indicates that the detection of organophosphonates using DBR PSi chips exhibits a couple of decades times better detection limits compared with single layer PSi (800 ppm of DFP for 5 min) [1] or Rugate structured PSi (31 ppm of DMMP for 1 min) [5].

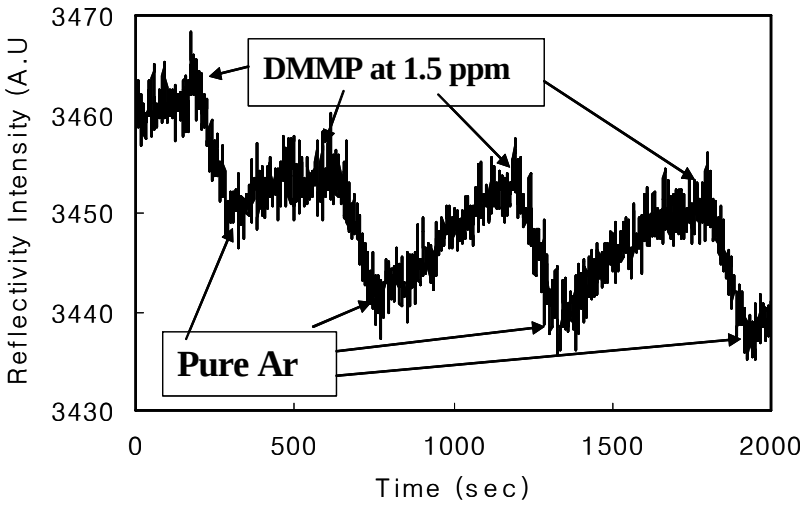

Figure 2.5. Plot for showing the detection limit of DMMP at 8.8 mg/m^3 (1.5 ppm) by using DBR PSi

2.4 Conclusions

This work demonstrates the detection of chemical nerve agents using DBR PSi. The red-shift of reflective wavelength has been observed due to the condensation of nerve gases. The detection process is reversible and reliable with in 15 sec. Detection limit for DBR PSi using tungsten lamp is 1.5 ppm (8.8 mg/m^3) for DMMP.

2.5 References

[1] H. Sohn, S. Letant, M. J. Sailor and W. C. Trogler, *J. Am. Chem. Soc*. **122**, 5399 (2000).

[2] C. Pacholski, M. Sartor, M. J. Sailor, F. Cunnin and G. M. Miskelly, *J. Am. Chem. Soc*. **127**, 11636 (2005).

[3] L. T. Canham, M. P.Stewart, J. M. Buriak, C. L. Reeves, M. Anderson, E. K. Squire, P. Allcock and P. A. Snow, *Phys. Status Solidi A.* **128**, 521 (2000).

[4] V. Lehmann, R. Stengl, H. Reisinger, R. Detemple and W. Theiss, *Appl. Phys. Lett*. **78**, 589 (2001).

[5] J. Dorvee and M. J. Sailor, *Phys. Stat. Sol*. **202**, 1619 (2005).

[6] M. S. Nieuwenhuizen and J. L. N. Harteveld, *Sens. Actuators B.* **40**, 167 (1997).

[7] D. Williams and G. Pappas, *Field Anal. Chem. Technol*. **3**, 45 (1999).

[8] K. E. LeJeune, J. R. Wild and A. J. Russell, *Nature* **395**, 27 (1998).

[9] E. S. Snow, F. K. Perkins, E. J. Houser, S. C. Badescu, and T. L. Reinecke, *Science* **307**, 1942 (2005).

[10] N. Taranenko, J.-P. Alarie, D. L. Stokes and T. Vo-Dinh, *J. Raman Spectrosc*. **27**, 379 (1996).

[11] A. R. Hopkins and N. S. Lewis, *Anal. Chem*. **73**, 884 (2001).

[12] S. E. Letant, S. R. Kane, B. R. Hart, M. Z. Hadi, T.-C. Cheng, V. K. Rastogi and J. G. Reynolds, *Chem. Commun*. 851 (2005).

Chapter Three
Detection of G-type Nerve Agent Simulants Based on a Double Reflection DBR Porous Silicon Interferometer

3.1 Introduction

G-type nerve-agent simulants, such as DMMP, DEEP, and TEP, having extremely toxicity are widely used as chemical weapons and pesticide toxins [1-3]. Sarin, a G-type nerve agent, has lethality depending on both concentration and exposure time. The LCt_{50} for sarin by inhalation of the vapor form is 100 milligrams of sarin per cubic meter of air for one minute. Therefore, rapid detection of nerve agent simulants is of current interest.

PSi has been an interesting materials for sensing applications because it has unique electronic and optical properties, as well as a large internal surface area. The large internal surface area (~100 m^2/cm^3) of PSi acts as a good host material for effective detection of toxin vapors [4], liquids [5], and biological molecules [6]. Besides its electronic and optical properties, PSi provides a wide range of morphological properties, as well as possible surface modifications that are useful for sensing applications [7-9].

In recent years, several possible applications using a multistructured PSi, both DBR and rugate PSi, providing a reflection band at a desired wavelength in the optical reflectivity spectrum, have been actively exploited. By adjusting the electrochemical etching conditions, such as the alternating current density, time, and

HF concentration, the morphology and the porosity of PSi multilayer can be easily controlled.

Encoded materials are of interest for their applications because a large number of parallel experiments can be performed in a short period of time [10-15]. Recently, multiple rugate-structured PSi containing many independent codes has been reported [16-18]. Multiple rugate peaks in optical reflectivity spectrum can be placed in the same physical location where both the wavelength and the amplitude of the spectral peaks are controllable by changing the etch parameters. However, the strategy to encode multiple DBR structures has not been reported yet. When the applied current densities obtained from single DBR structures are doubled, DBR PSi with two reflection peaks has been obtained. Here, we report an efficient method for the detection of nerve agent simulants based on a DBR PSi interferometer with two reflection peaks. The detection mechanism involves a red shift of the reflectivity resulting from an increase in the average refractive index of the multilayers.

3.2 Experiments

The DBR PSi samples were prepared by electrochemical etching of heavily-doped p^{++}-type silicon wafers (boron doped, polished on the <100> face, resistivity of 0.8-1.2 mΩ·cm, Siltronix, Inc.). The etching solution consisted of a 3:1 volume mixture of aqueous 48% hydrofluoric acid (ACS reagent, Aldrich Chemicals) and absolute ethanol (ACS reagent, Aldrich Chemicals). The galvanostatic etch was carried out in a Teflon cell by applying 20 cycles of a two-electrode configuration. DBR PSi with one or two reflection bands was prepared by using periodic square-wave currents between 5 $mA \cdot cm^{-2}$ for 90 sec and 50 $mA \cdot cm^{-2}$ for 3 sec or between 10 $mA \cdot cm^{-2}$ for 90 sec and 100 $mA \cdot cm^{-2}$ for 3 sec, respectively. Analytes, such as DMMP, DEEP, and TEP, were purchased from Sigma-Aldrich, Inc., and were used without purification.

The optical reflectivity spectra of DBR PSi with one or two reflection bands have been measured by using a tungsten-halogen lamp and an Ocean Optics S2000 CCD spectrometer fitted with a fiber optic input. The reflected light collection end of the fiber optic was positioned at the focal plane of the optical microscope. SEM images were obtained by using a cold field emission scanning electron microscope (FE-SEM, S-4800, Hitachi).

3.3 Results and Discussion

DBR PSi exhibits a high reflectivity band with a Bragg wavelength λ_{Bragg}, depending on the thickness of the layers (d_1, d_2) and the corresponding refractive indices (n_1, n_2). The mth order of the Bragg peak is given by

$$m\lambda_{Bragg} = 2(d_1n_1 + d_2n_2).$$

Typical etch parameters for the DBR PSi structure involve using a periodic square-wave current between low and high current densities. In our previous work [19], the applied current densities for the fabrication of DBR PSi was varied between 5 and 50 $mA \cdot cm^{-2}$. The dissolution times for a $\lambda/4$ layer of the Bragg structures were typically from 90 sec to 5 sec. Its reflection band had a narrow FWHM of 20 nm at 520 nm. DBR PSi with two reflection peaks was obtained when the current densities of the single DBR structure was doubled. The photonic feature of the latter DBR PSi exhibited a high reflectivities at both 560 and 717 nm, as shown in Figure 3.1. The second reflection peak might have resulted from the increase in the refractive indices according to the Bragg equation, which is proportional to the applied current densities. The first and the second reflection bands of DBR PSi have FWHM of 15 and 20 nm, respectively. The cross-sectional image of the double reflected DBR PSi shown in Figure 3.2 illustrates that the latter DBR PSi has a depth of 11.5 microns.

A repeating etching process results in two discrete refractive indices. DBR PSi samples are placed in an exposure chamber fitted with an optical window. The samples are exposed to a flux of DMMP (partial pressure of 0.22 Torr or 290 ppm) in air with a flow rate of 5 L/min.

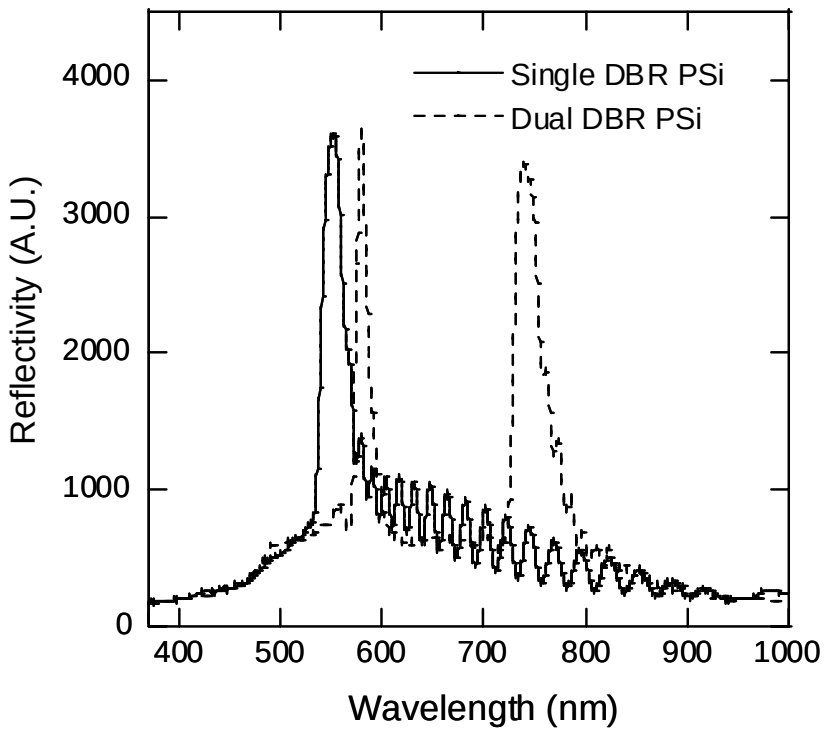

Figure 3.1. Reflectivity spectra of DBR PSi with one or two reflection peaks

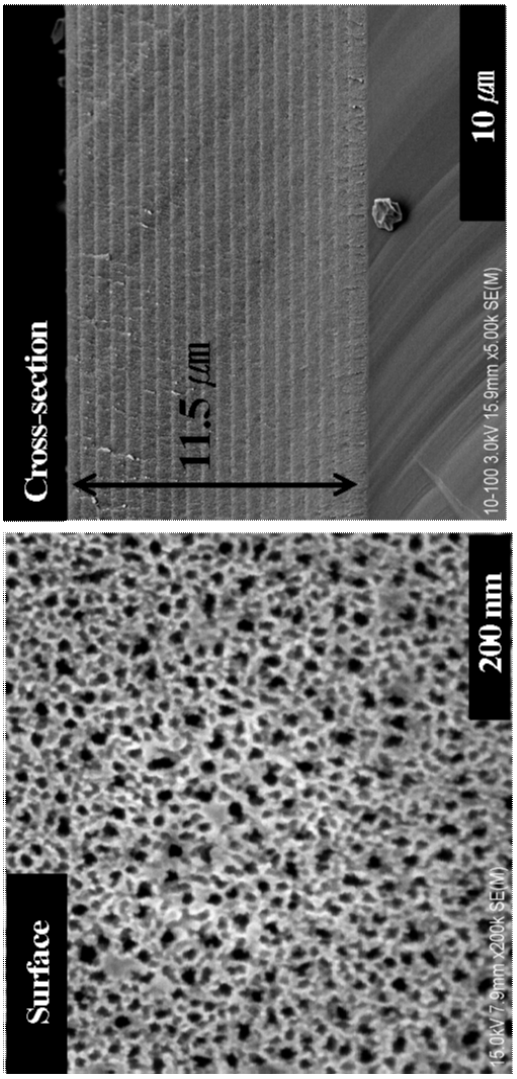

Figure 3.2. Surface and cross-sectional FE-SEM images of DBR PSi showing two reflection bands

Figure 3.3 shows reflectivity spectra of DBR PSi with one or two reflection bands while exposing the detector to organophosphate vapors. The reflection spectra from DBR PSi with one reflection peak for the detection of nerve agent stimulants were recorded for 1 min. under exposure to the vapor of each analyte [18]. Reed shift of 25 nm (1a), 10 nm (1b), and 10 nm (1c) in the reflectivity were observed for the air-saturated vapors of TEP (135 ppm), DEEP (135 ppm), and DMMP, respectively. DBR PSi with two reflection peaks was also exposed to a flux of organophosphate vapors in identical conditions. The reflection spectra from DBR PSi with two reflection bands were recorded for 30 sec. Capillary condensation caused both reflection peaks to shift to longer wavelengths by 13 nm for the first DBR peak (shorter wavelength) and 18 nm for the second peak (longer wavelength) under exposure to TEP vapor. Red shifts of 22 and 32 nm for the detection of DMMP were observed for the first and the second DBR peaks in the reflectivity spectrum, respectively. For DEEP vapor, red shifts of 39 and 52 nm for the first and the second DBR peaks were observed in the reflectivity spectrum, respectively. More dramatic red shifts of the reflectivity were observed in the cases of DMMP and DEEP vapors, even though the vapor pressures of DMMP and DEEP were lower than that of TEP. These shifts are due to an increase in the reflective indices of the porous medium. The red shifts of the reflectivity vary with the degree of condensation of the analyte. Capillary condensation depends on the chemical properties of the DBR PSi surface and the analyte, as well as the vapor pressure of the analyte. Since all parameters in these experiments are fixed, except for the chemical property of analyte, the chemical interaction between the surface of porous silicon and analyte might influence the shift of reflectivity rather than the vapor pressure of analyte. In addition, DBR PSi with two reflection bands exhibits better detection efficiency than DBR PSi with one reflection band.

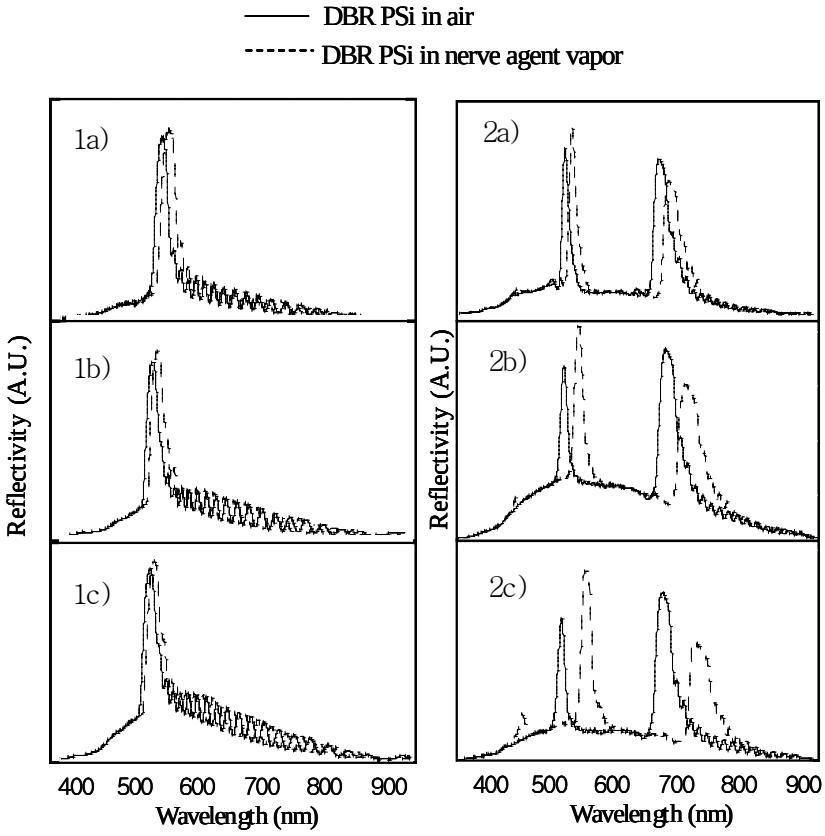

Figure 3.3. Reflectivity spectra of DBR PSi samples DBR PSi showing single or two reflection peaks recoded for 30 sec using the tungsten-halogen lamp as a light source. A red-shift of reflectivity for single reflection DBR PSi, 1a) TEP; 25 nm, 1b) DMMP; 10 nm, 1c) DEEP; 10 nm and double reflection DBR PSi, 2a) TEP; 13 nm for the first DBR peak and 18 nm for the second DBR peak, 2b) DMMP; 22 nm and 32 nm, 2c) DEEP; 39 nm and 52 nm are observed.

Figure 3.4 illustrates how an analyte might be specified using a DBR PSi with two reflection peaks. The DBR PSi peaks exhibit different ratios of the red shift to nalytes, which can be used to identify the analyte. Figure 3.5 shows the change in the reflective intensities at the two fixed wavelengths (560 nm and 717 nm) when DBR PSi having two reflection bands is exposed to DMMP vapor. Each exposure time is 30 s, and the reflective intensities decrease instantly just after the exposure. The ratio of the decrease in intensity is 66.4% for the first peak and 71.5% for the second peak. This result indicates that DBR PSi having two reflection bands exhibits selectivities for analytes. In addition, this real-time detection for the stimulant indicates that the detection measurements are reversible.

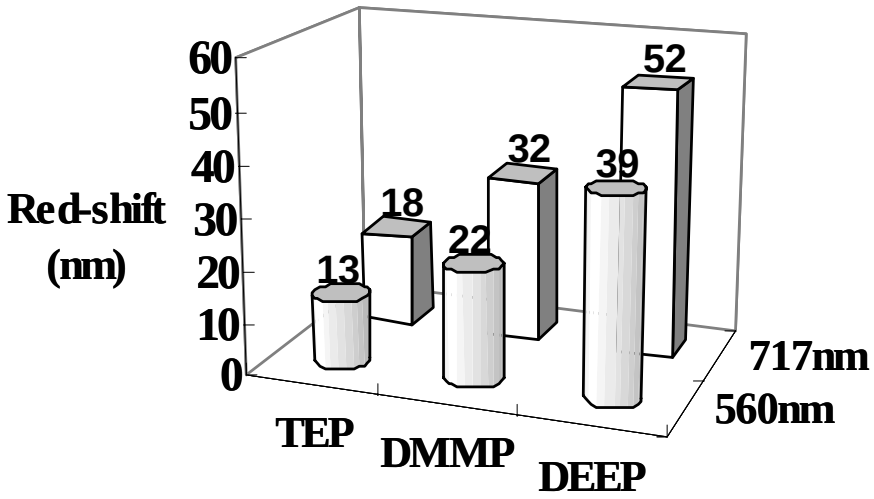

Figure 3.4. Comparison of the red-shifts of two reflection peaks with different nerve agent analytes

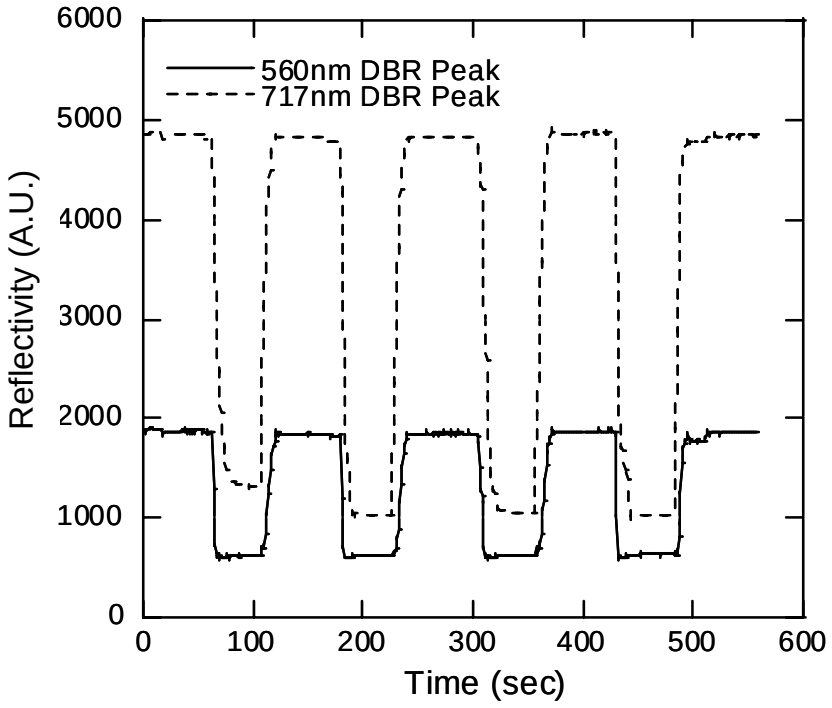

Figure 3.5. Response for the reflective intensities at two fixed wavelengths of DBR PSi showing two reflection peaks under the exposure of DMMP vapor

3.4 Conclusions

DBR PSi with double reflection peaks has been obtained, when the current densities of single DBR structure increase twice. The change of reflectivity spectra of DBR PSi with one or two reflection bands was measured for the detection of organophosphate vapors. Reflection spectra from DBR PSi with one reflection peak for the detection of nerve agent stimulants display 25, 10, and 10 nm of red-shift for the air-saturated vapor of TEP, DEEP, and DMMP, respectively. DBR PSi with two reflection peaks has been also used to detect organophosphate vapors in identical conditions. Dramatic red-shifts of reflectivity are observed in case of DMMP and DEEP vapors. DBR PSi with two reflection bands exhibits better detection efficiency than DBR PSi with one reflection band. DBR PSi with two reflection peaks exhibit different ratios of red-shift to analytes, indicating how to identify the analyte. The real-time detection for the stimulant indicates the reversible detection measurements.

3.5 References

[1] S. M. Kanan and C. P. Tripp, *Langmuir* **17**, 2213 (2001).

[2] S. M. Aschmann, E. C. Tuazon, and R. Atkinson, *J. Phys. Chem. A.* **109**, 2282 (2005).

[3] B. C. Singer, A. T. Hodgson, H. Destaillats, T. Hotchi, K. L. Revzan, and R. G. Sextro, *Environ. Sci. Technol.* **39**, 3203 (2005).

[4] H. Sohn, S. Letant , M. J. Sailor, and C. Trogler, *J. Am. Chem. Soc.* **122**, 5399 (2000).

[5] S. Letant and M. J. Sailor, *Adv. Mater.* **13**, 355 (2001).

[6] S. Chan, S. R. Horner, P. M. Fauchet, and B. L. Miller, *J. Am. Chem. Soc.* **123**, 11797 (2001).

[7] C. Pacholski, M. Sartor, M. J. Sailor, F. Cunnin, and G. M. Miskelly, *J. Am. Chem. Soc.* **127**, 11636 (2005).

[8] V. Lehmann, R. Stengl, H. Reisinger, R. Detemple, and W. Theiss, *Appl. Phys. Lett.* **78**, 589 (2001).

[9] J. R. Dorvee, A. M. Derfus, S. N. Bhatia, and M. J. Sailor, *Nat. Mater.* **3**, 896 (2004).

[10] M. Bruchez, M. Moronne, P. Gin, S. Weiss, and A. P. Alivisators, *Science* **281**,2013(1996).

[11] J. A. Ferguson, T. C. Boles, C. P. Adams, and D. R. Walt, *Nat. Biotechnol.* **14**, 1681 (1996).

[12] H. Fenniri, L. Ding, A. E. Ribbe, and Y. Zyrianov, *J. Am. Chem. Soc.* **123**, 8151 (2001).

[13] W. C. W. Chan and S. Nie, *Science* **281**, 2016 (1998).

[14] S. R. Nicewarner-Peña, R. G. Freeman, B. D. Reiss, L. He, D. J. Peña, I. D. Walton, R. Cromer, C. D. Keating, and M. J. Natan, *Science* **294**, 137 (2001).

[15] F. Cunin, T. A. Schmedake, J. R. Link, Y. Y. Li, J. Koh, S. N. Bhatia, and M. J. Sailor, *Nat. Mater.* **1**, 39 (2002).

[16] S. O. Meade, M. S. Yoon, K. H. Ahn, and M. J. Sailor, *Adv. Mater.* **16**, 1811 (2004).

[17] J. Park, S. Cho, Y. C. Ko, and H. Sohn, *J. Korean Phys. Soc.* **50**, 695 (2007).

[18] S. Jang, J. Kim, Y. Koh, Y. C. Ko, H. -G. Woo, and H. Sohn, *J. Nanosci. Nanotechnol.* **7**, 4049 (2007).

[19] B.-J. Lee, S. Jang, and H. Sohn, *Solid State Phenom.* **124-126**, 491 (2006).

Chapter Four
Multi-encoded Rugate Porous Silicon as Nerve Agent Sensors

4.1 Introduction

Detection of G-type chemical warfare agents is of major importance since they are highly toxic and thus a matter of international concern. DCP, TEP, DMMP, and DEEP are stimulant for G-type nerve agents [1-4]. Detection methods for nerve agents have been recently developed by using of enzymes, [5] interferometry, [6] fluorescence [7-8], single-walled carbon nanotube [9], metal oxide [10], and organic polymers [11]. PSi is also an alternative method to detect chemical nerve agents [6,12].

Photonic crystals of PSi have been investigated extensively, because of their unique properties, including surface area and convenient surface chemistry, as well as their optical signal transduction capability. These properties have led to their use in chemical and biological sensors, biomaterials, and optical devices [13-15]. Electrochemical etch of single crystalline silicon can easily control the pore morphology, thickness, and porosity by appropriate adjustment of the preparation conditions [16]. Chemical or bio molecules can be detected based on changes in the spectral interference pattern [6].

Photonic crystals containing rugate structure result in a mirror with high reflectivity in a specific narrow spectral region and are prepared by applying a

computer-generated pseudo-sinusoidal current waveform [17]. Rugate filters possess a sinusoidally varying porosity gradient in the direction perpendicular to the plane of the filter. Multiple rugate-structured PSi showing many sharp independent reflection peaks has been also reported [18].

The importance of PSi is due to its very high surface area for reactions, its unique photonic properties, and its process compatibility with semiconductor technology [19]. This high surface area material has been shown to be useful in a variety of analytical applications, in MEMS (micro electro mechanical systems) as a matrix for MALDI (matrix-assisted laser desorption ionization) mass spectroscopy [20] and especially in chemical and biological sensors [21]. Multiplexed assays [22-23] are powerful tools for studying genomes, for identifying candidate drugs, and for a variety of other applications in which a large number of parallel experiments should be performed in a short period of time [18]. Recently, beads or particles containing many independent codes made by using quantum dots, fluorescent molecules, and metal rods have been used for these applications [24,17].

The present chapter describes a detection method to specify nerve agent simulants based on changes in the spectral interference of a triple rugate-structured PSi.

4.2 Experiments

All Chemicals such as triethyl phosphate (TEP; 99.8%), diethyl chlorophosphate (DCP; 97%), dimethyl methylphosphonate (DMMP; 97%), and diethyl ethylphosphonate (DEEP; 98%) were commercially purchased from Sigma-Aldrich, Inc. and used without any purification. Rugate PSi having three photonic band gaps were prepared by electrochemically etching of heavily doped p^{++}-type silicon wafer (boron doped, polished on the <100> face, resistivity; 0.8 ~ 1.2 mΩ·cm, obtained from Siltronix, Inc.). The etching solution consisted of a 3:1 volume mixture of aqueous 48% hydrofluoric acid (ACS reagent, Aldrich Chemicals) and absolute ethanol (ACS reagent, Aldrich Chemicals). Galvanostatic etching was carried out in a Teflon cell using a two-electrode configuration. A composite waveform summed three computer-generated pseudo-sinusoidal current waveform varying between 51.5 and 74.6 $mA \cdot cm^{-2}$ (100 s periodicity, 30 repeats) was applied as an anodization current. Each sine component varied from 0.42 to 0.30 Hz, with a spacing of 0.06 Hz between each sine component. The anodization current was supplied by a Keithley 2420 high-precision constant current source which was controlled by a computer to allow the formation of PSi multilayers. To prevent the photogeneration of carriers, the anodization was performed in the dark. After formation, the samples were rinsed with absolute ethanol and dried with nitrogen gas.

For the data acquisition, the samples were illuminated with a tungsten-halogen lamp, and the reflected light spectrum was measured using an Ocean Optics S2000 CCD spectrometer fitted with a fiber optic input. The reflected light collection end of the fiber optic was positioned at the focal plane of the optical microscope. The surface and cross-sectional SEM images of samples were obtained by a cold field emission scanning electron microscope (FE-SEM, S-4800, Hitachi).

4.3 Results and Discussion

Photonic crystals containing rugate structure are prepared by applying a computer-generated pseudo-sinusoidal current waveform. Two different samples, single rugate-structured PSi and triple rugate-structured PSi, have been prepared. The waveform used in the present work involves an individual sine component, which is represented by Equation 4.1.

$$y_i = A_i \sin(k_i t) + B \qquad (1)$$

Where y_i represents a temporal sine wave of amplitude, A_i; frequency, k_i; time, t; applied current, B. The reflectivity spectrum of single rugate-structured PSi sample prepared with 0.30 Hz of k, 11.55 mA of A, and 63.05 mA of B is shown in Figure 4.1(A) and exhibits a sharp reflectivity at 554 nm. This rugate peak can be tuned to appear anywhere in the visible spectral range, depending on the programmed etch waveform.

Photonic crystals containing triple rugate-structured PSi are prepared by applying a composite waveform summed three computer-generated pseudo-sinusoidal current waveform. The rugate PSi generated in this method exhibits three sharp lines in the optical reflectivity spectrum. The values of k_i for each of the sine components are varied from 0.30 to 0.42 Hz, with a spacing of 0.06 Hz between each sine component. Three individual sine components are summed together to create a composite waveform and shown in Equation 4.2 and Figure 4.1(B).

$$Y_{comp} = A_1\sin(k_1t) + A_2\sin(k_2t) + A_3\sin(k_3t) + B \quad (2)$$

Equation 4.2 can be converted to an analog current-time waveform to etch using a computer-controlled digital galvanostat. The values of A_i and B for every sine component are 11.55 and 63.05 mA, respectively. The reflectivity spectrum of triple rugate structured PSi shown in Figure 4.1(C) displays three reflection peaks at 554, 632, and 745 nm, respectively. Each of the main peaks in an optical reflectivity spectrum corresponds to one of the sine components of the composite waveform, indicating that the reflectivity spectrum represents the Fourier transform of the composite current-time waveform.

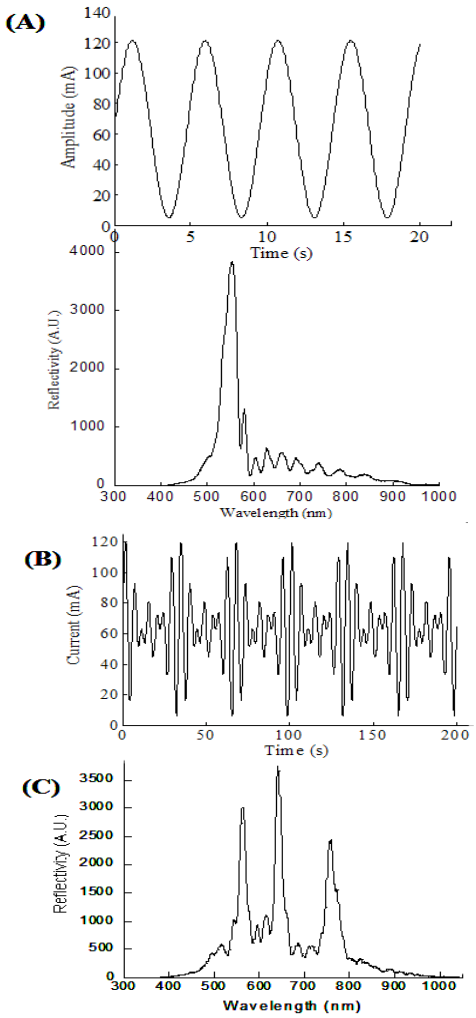

Figure 4.1. Representation of the encoding method and reflectivity specta. (A) single sine components and reflectivity spectrum of single rugate PSi; (B) a composite waveform summed three individual sine components; (C) reflectivity spectrum of triple rugate-structured PSi

An effective refractive index of rugate PSi depends directly on porosity. An electrochemical etching offers the opportunity to modulate the porosity in depth and allows the fabrication of structures with any refractive index profile. When the current is gradually modulated, a smooth index profile of rugate PSi can be achieved. FE-SEM images of single rugate-structured PSi are shown in Figure 4.2(A) and display a sinusoidally varying porosity gradient in the direction perpendicular to the plane of the filter. The cross-sectional image of triple rugate-structured PSi shown in Figure 4.2(B) illustrates that it possesses a depth of 100 micron without such a gradient porosity depth profile due to the composite current waveform. Triple rugate-structured PSi sample is placed in an exposure chamber fitted with an optical window. The sample is then exposed to a flux of nerve agent such as DMMP, DCP, TEP, and DEEP in air with a flow rate of 5 L/min. When the PSi sample is exposed to analytes in the gas phase, capillary condensation causes an increase of its effective refractive index by the replacement of air to liquid of analyte. The positions of three reflection peaks are monitored as a function of time after an analyte vapor is introduced. Diffusion and capillary condensation effects determine the response, because the pressure of analyte is constant. Detection mechanism of G-type nerve agent simulant (TEP) based on triply encoded rugate PSi describes in Figure 4.3.

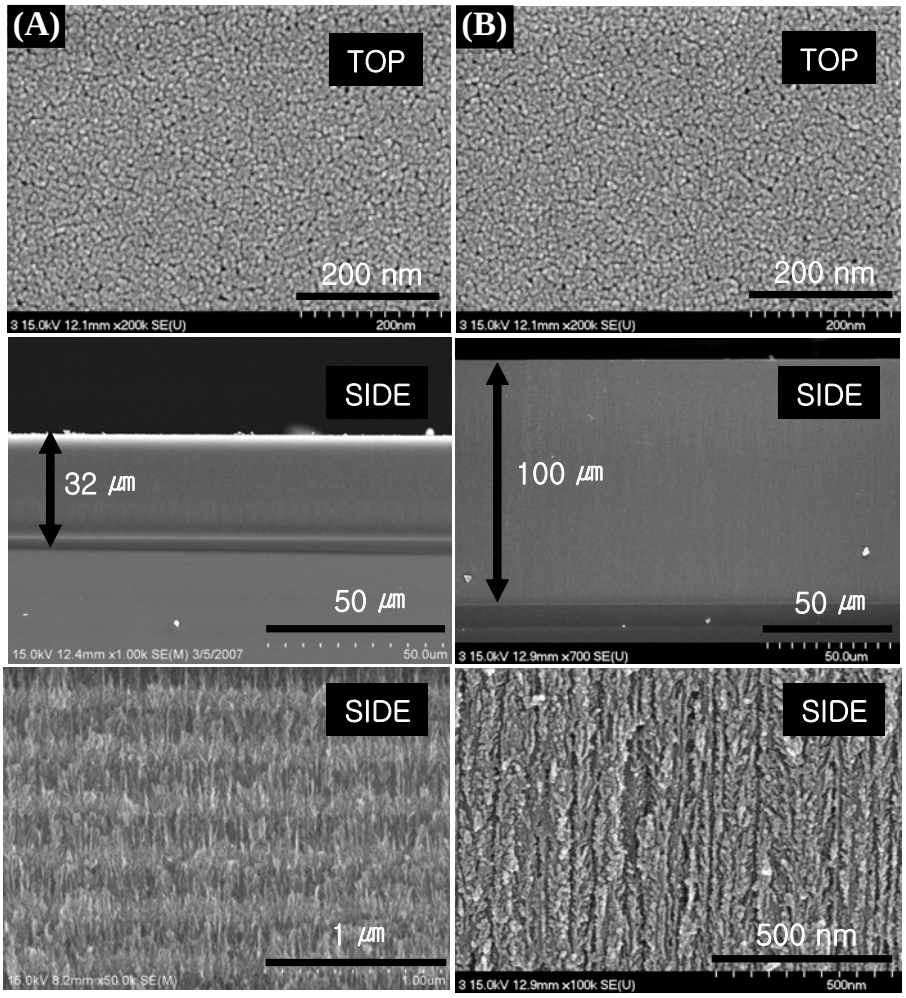

Figure 4.2. FE-SEM images of single (A) and triple rugate-structured PSi (B)

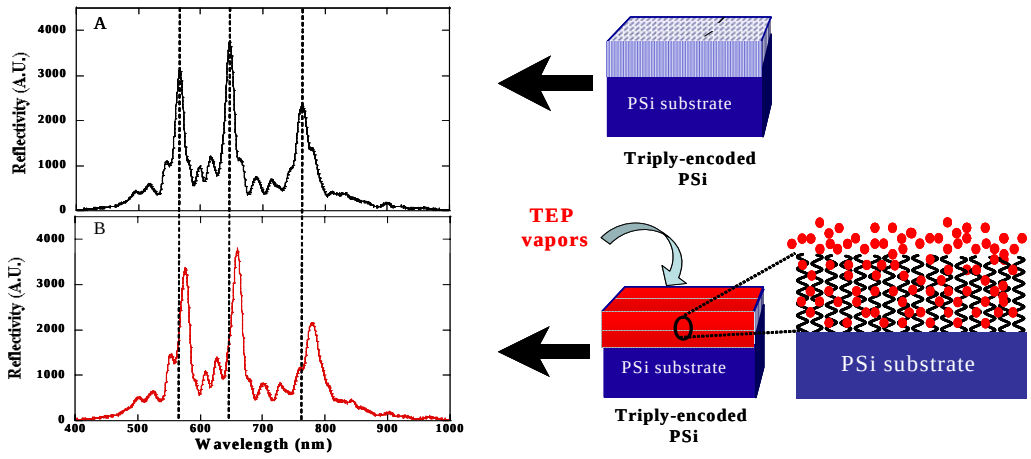

Figure 4.3. Detection mechanism of nerve agent simulant (TEP) vapors based on triply encoded rugate PSi

Figure 4.4 shows the shift of reflection peaks under the exposure of four different analytes, respectively. The time required for the system to reach equilibrium is less than 1 min for all analytes. The analytes have different refractive indices and vapor pressures, respectively. The amplitude of the red shift of the reflection peaks depends on both refractive index and vapor pressure of the analyte condensed in the sample as well as the surface characteristics including hydrophilicity and varied pore diameter. These parameters would lead to very complex pattern of red shift for an individual reflection peak. The degree of red shift of individual reflection peak is obtained for different analytes and summarized in Table 4.1. It should be noticed that TEP shows larger red-shift even its vapor pressure (135 ppm) is lower than DMMP (290 ppm), due to the complex nature of parameters. The reflection peak at the longer wavelength exhibits the more red-shifted photonic feature. Three reflection peaks display different degrees of the red-shift for an individual analyte. The use of multi-rugate structured PSi could be inspired by the performance to specify an analyte.

(unit : nm)

Peak	DMMP	DCP	TEP	DEEP
1	4	5	10	13
2	4	6	10	17
3	5	9	17	20

Table 4.1. FE-SEM images of single (A) and triple rugate-structured PSi (B)

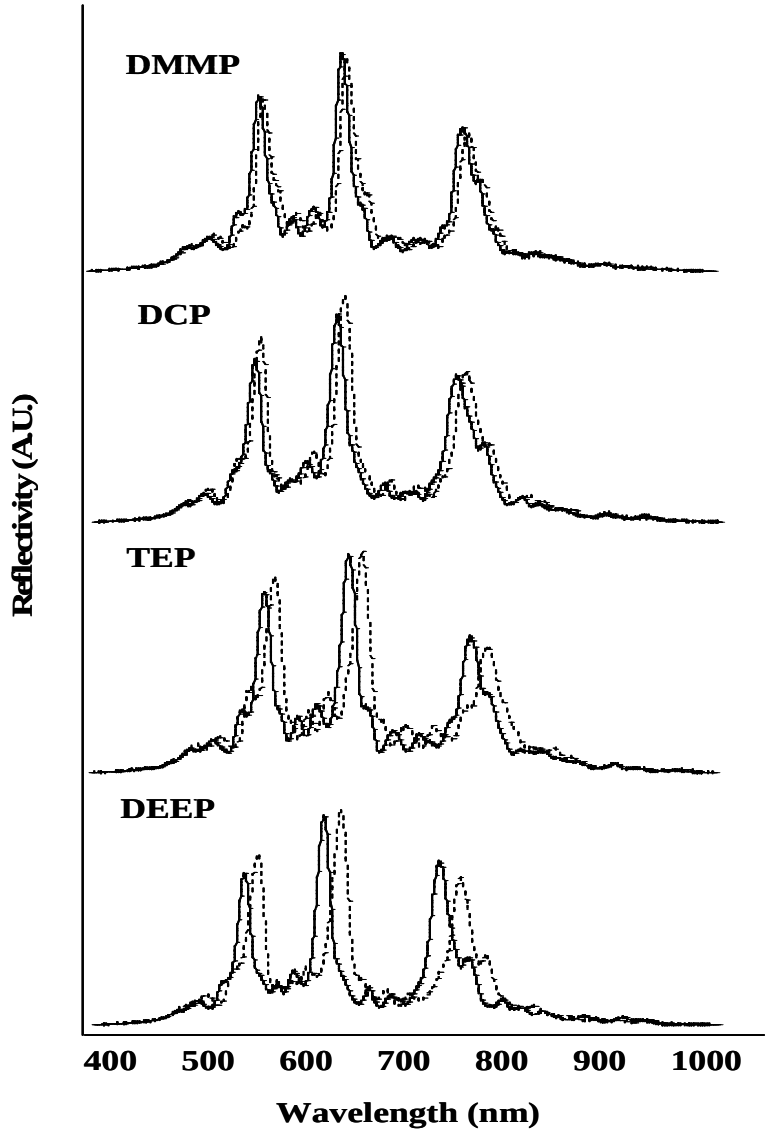

Figure 4.4. Optical reflectivity spectra of triple rugate-structured PSi in air (solid line) and under the exposure nerve agent vapors (dotted line) for 1 min, respectively

4.4 Conclusions

The nanostructured rugate PSi containing multiple photonic band gaps have been generated by an electrochemical etching through applying a composite waveform summed three computer-generated pseudo-sinusoidal current waveforms. The detection mechanism for sensing chemical nerve agents involves the red-shift of the reflectivity resulted from an increase in the average refractive index of the PSi multilayers. Three reflection peaks of the triple rugate-structured PSi display different degrees of the red-shift to specify the particular analyte.

4.5 References

[1] S. M. Kanan and C. P. Tripp, *Langmuir* **17**, 2213(2001).

[2] S. M. Aschmann, E. C. Tuazon, and R. Atkinson, *J. Phys. Chem. A.* **109**, 2282 (2005).

[3] B. C. Singer, A. T. Hodgson, H. Destaillats, T. Hotchi, K. L. Revzan, and R. G. Sextro, *Environ. Sci. Technol.* **39**, 3203 (2005).

[4] Office of the special assistant for Gulf War Illness, Department of Defense, Fact Sheet on Exposure Limits for Sarin(GB), 1997.

[5] K. E. LeJeune, J. R. Wild, and A. J. Russell, *Nature* **395**, 27 (1998).

[6] H. Sohn, S. Letant , M. J. Sailor, and W. C. Trogler, *J. Am. Chem. Soc.* **122**, 5399 (2000).

[7] S.-W. Zhang and T. M. Swager, *J. Am. Chem. Soc.* **125**, 3420 (2003).

[8] J. D. Trevor and R. J. Julius, *J. Am. Chem. Soc.* **128**, 4500 (2006).

[9] E. S. Snow, F. K. Perkins, E. J. Houser, S. C. Badescu, and T. L. Reinecke, *Science*. **307**, 1942 (2005).

[10] N. Taranenko, J.-P. Alarie, D. L. Stokes, and T. Vo-Dinh, *J. Raman Spectrosc*. **27**, 379 (1996).

[11] A. R. Hopkins and N. S. Lewis, *Anal. Chem*. **73**, 884 (2001).

[12] B.-J. Lee, S. Jang, and H. Sohn, *Solid State Phenom*. **124-126**, 491 (2007).

[13] C. Pacholski, M. Sartor, M. J. Sailor, F. Cunnin, and G. M. Miskelly, *J. Am. Chem. Soc*. **127**, 11636 (2005).

[14] L. T. Canham, M. P.Stewart, J. M. Buriak, C. L. Reeves, M. Anderson, E. K. Squire, P. Allcock, and P. A. Snow, *Phys. Status Solidi A.* **128**, 521 (2000).

[15] V. Lehmann, R. Stengl, H. Reisinger, R. Detemple, and W. Theiss, *Appl. Phys. Lett*. **78**, 589 (2001).

[16] A. Janshoff, K. -P. S. Dancil, C. Steinem, D. P. Greiner, V. S.-Y. Lin, C. Gurtner, K. Motesharei, M. J. Sailor, and M. R. Ghadiri, *J. Am. Chem. Soc*. **120**, 12108 (1998).

[17] F. Cunin, T. A. Schmedake, J. R. Link, Y. Y. Li, J. Koh, S. N. Bhatia, and M. J. Sailor, *Nat. Mater*. **1**, 39 (2002).

[18] S. O. Meade, M. S. Yoon, K. H. Ahn, and M. J. Sailor, *Adv. Mater*. **16**, 1811 (2004)

[19] A. J. Nolte, M. F. Rubner, and R. E. Cohen, *Langmuir* **20**, 3304 (2004).

[20] S. E. Letant and M. J. Sailor, *Adv. Mater.* **12**, 335 (2000).

[21] M. J. Sailor and J. R. Link, *Chem. Commun.* 1375 (2005).

[22] M. G. Berger, R. Arens-Fischer, M. Thönissen, M. Krüger, S. Billat, H. Lüth, S. Hilbrich, W. Theiß and P. Grosse, *Thin Solid Films* **297**, 237 (1997).

[23] S. Setzu, P. Ferrand, and R. Romestain, *Mat. Sci. Eng. R.* **69-70**, 34 (2000).

[24] M. Bruchez, M. Moronne, P. Gin, S. Weiss, and A. P. Alivisators, *Science* **281**, 2013 (1996).

Chapter Five
Surface-functionalized DBR Porous Silicon for Sensing Organophosphates Using Various Detection Light Sources

5.1 Introduction

Photonic crystals of porous silicon (PSi) have been a topic of interest because of their unique properties, including surface area and convenient surface chemistry, as well as their optical signal transduction capability. These properties have led to their use in chemical and biological sensors [1-4], biomaterials [5], and optical devices [6]. Multistructured PSi such as Rugate PSi have been recently investigated in terms of their possible applications [7-12]. DBR (distributed Bragg reflectors) PSi exhibits unique optical properties providing the reflection of a specific wavelength in the optical reflectivity spectrum. DBR structured porous silicon having the photonic structure of a Bragg filter has been developed by applying a computer generated square current density waveform [13]. Biological or chemical molecules can be detected based on changes in the spectral interference pattern.

Detection of G-type chemical warfare agents is of major importance since they are highly toxic and thus a matter of international concern. Triethyl phosphate (TEP) is a simulant for G-type nerve agents. Sarin, a G-type nerve agent, has lethality depending on both concentration and exposure time. The LCt_{50} for sarin by inhalation of its vapor form is 100 milligrams of sarin per cubic meter of air for one minute [14]. The main method currently used to detect nerve agents is

based on utilization of a surface acoustic wave (SAW) device [15-16]. Other methods using enzymes [17], single-walled carbon nanotubes (SWNT) [18], metal oxides [19], and organic polymers [20] have also recently been reported. PSi is an alternative method to detect chemical nerve agents [21-22]. This chapter reports on an efficient detection method for a nerve agent simulant based on DBR PSi using a light emitting diode (LED) or laser as incident light sources. Detection of other simulants, i.e., dimethyl methylphosphonate (DMMP) and diethyl ethylphosphonate (DEEP), have also been investigated.

5.2 Experiments

PSi samples were prepared by electrochemical etching of heavily doped p^{++}-type silicon wafers (boron doped, polished on the <100> face, resistivity of 0.8-1.2 m Ω·cm, Siltronix, Inc.). The etching solution consisted of a 3:1 volume mixture of aqueous 48% hydrofluoric acid (ACS reagent grade, Aldrich Chemicals) and absolute ethanol (ACS reagent grade, Aldrich Chemicals). Galvanostatic etch was carried out in a Teflon cell applying 20 cycles of a two-electrode configuration. DBR PSi was prepared using a computer-controlled periodic square wave current between 5 $mA \cdot cm^{-2}$ for 90 s and 50 $mA \cdot cm^{-2}$ for 3 s. Prepared DBR PSi samples exhibit high reflectivity at 510 nm in the reflectivity spectrum. The reflection band of DBR PSi has a full-width at half-maximum (FWHM) of 20 nm.

DBR PSi samples were spin-coated with 0.01 M of copper (II) sulfate aqueous solution, washed with hexane to remove the copper complex on the surface of PSi, and dried under reduced pressure prior to use. All analytes such as triethyl phosphate (TEP; 99.8%), diethyl chlorophosphate (DCP; 97%), dimethyl methylphosphonate (DMMP; 97%), and diethyl ethylphosphonate (DEEP; 98%) are commercially purchased from Sigma-Aldrich, Inc. and used without further purification.

Optical reflectivity spectra of DBR PSi showing specific one reflection band has been measured by using a tungsten-halogen lamp, LED (λ_{em} = 520, 590 nm) or laser (λ_{em} = 530nm) and an Ocean Optics S2000 CCD spectrometer fitted with a fiber optic input. The reflected light collection end of the fiber optic was positioned at the focal plane of the optical microscope. SEM images have been obtained by a cold field emission scanning electron microscope (FE-SEM, S-4800, Hitachi).

5.3 Results and Discussion

A DBR PSi exhibits a high reflectivity band with a Bragg wavelength λ_{Bragg}, depending on the thickness of the layers (d_1, d_2) and the corresponding refractive indices (n_1, n_2). The mth order of the Bragg peak is given by:

$$m\lambda_{Bragg} = 2(d_1n_1 + d_2n_2).$$

Typical etch parameters for DBR PSi structure involves using a periodic square wave current between low and high current densities. FE-SEM images shown in Figure 5.1 were obtained using a cold field emission scanning electron microscope (FE-SEM, S-4800, Hitachi). The cross-sectional image of DBR PSi shown illustrates that the multilayer DBR PSi has a depth of a few microns. A repeating etch process results in two distinct refractive indices.

Copper (II) chloride and copper (II) sulfate were found to adsorb NH_3, SO_2, and organophosphate [23]. Energy-dispersive X-ray analysis reveals the presence of copper (II) sulfate in the DBR PSi as shown in Figure 5.1. After the incorporation of copper (II) sulfate in the pores, DBR PSi samples are placed in an exposure chamber fitted with an optical window. The samples are then exposed to a flux of TEP (135 ppm) in air with a flow rate of 5 L/min. Optical reflectivity spectra were measured using a tungsten-halogen lamp and an Ocean Optics S2000 CCD spectrometer fitted with a fiber optic input. The reflected light collection end of the fiber optic was positioned at the focal plane of the optical microscope.

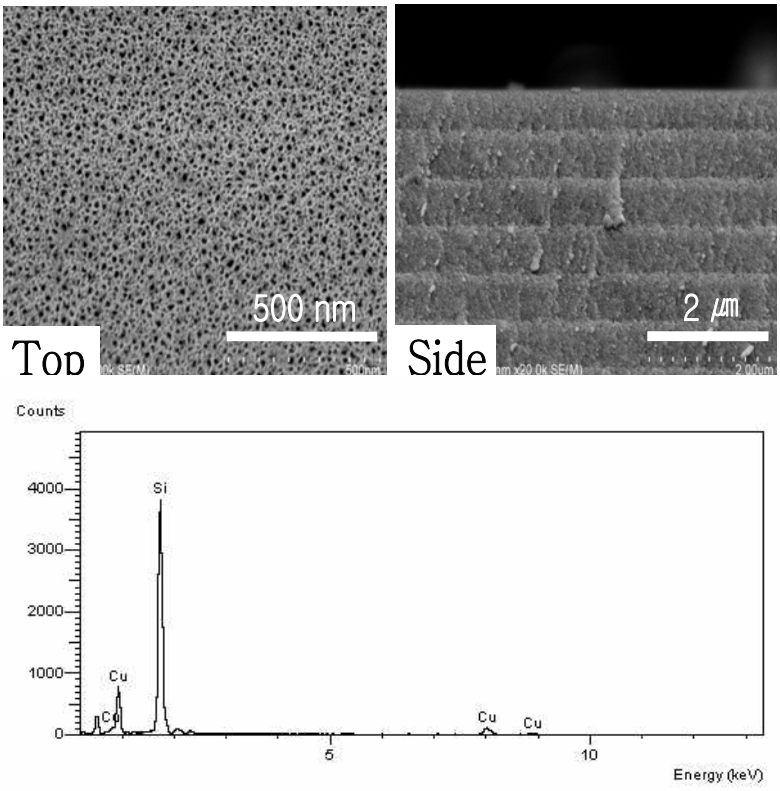

Figure 5.1. Surface and cross-sectional FE-SEM images of Cu coated DBR PSi sample and EDX spectrum of element percent at the same location (Si:Cu = 69:31)

Figure 5.2 (A) shows reflectivity spectra recorded under illumination with the tungsten-halogen lamp after 1 min. Capillary condensation and then adsorption of organophosphate to copper (II) sulfate in the pores cause the reflectivity spectrum of the DBR PSi to shift by about 12 nm to longer wavelengths due to an increase in reflective indices of the porous medium. Such a large red shift is characteristic of an increase in the average refractive index of the multilayers, consistent with the replacement of a significant amount of empty pore volume with organophospate.

The effect of incorporated concentration of copper (II) sulfate in the pores on the detection limit for DMMP is shown in Figure 5.2(B). Different decreases of reflective intensity at 510 nm according to the loaded quantity of copper (II) sulfate are obtained. Maximum decrease of reflective intensity is observed for the DBR PSi with a minimum concentration of 0.1 M copper (II) sulfate.

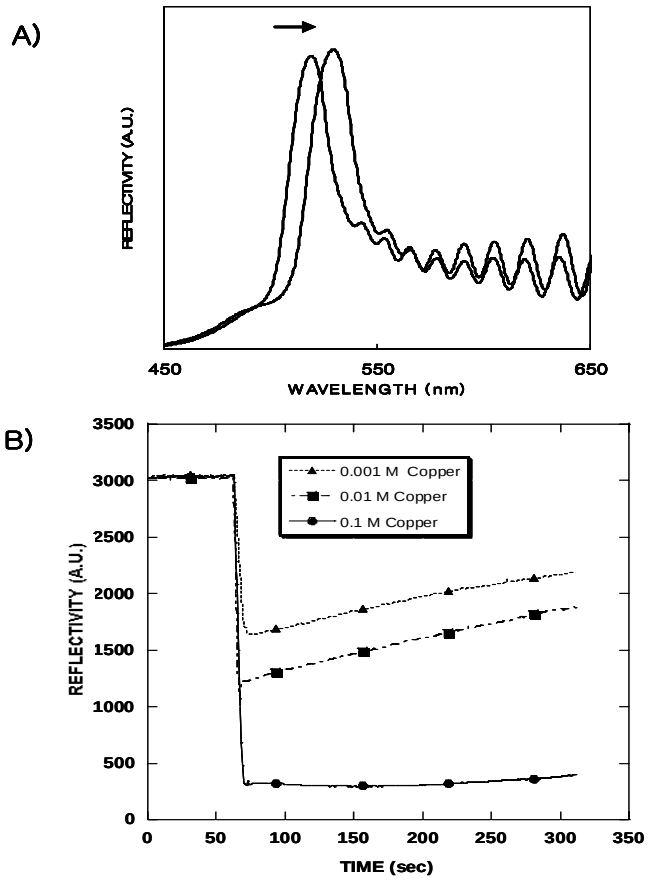

Figure 5.2. (A) Reflectivity spectra of DBR PSi sample containing copper (II) sulfate under a flux of TEP in air. (B) Decreases of reflective intensity for DBR PSi samples containing different concentrations of copper (II) sulfate under a flux of DMMP in air

A schematic diagram of the TEP sensing mechanism is shown in Figure 5.3. A red-shift of reflectivity of 10 and 12 nm has been observed in the case of DEEP and DMMP, respectively.

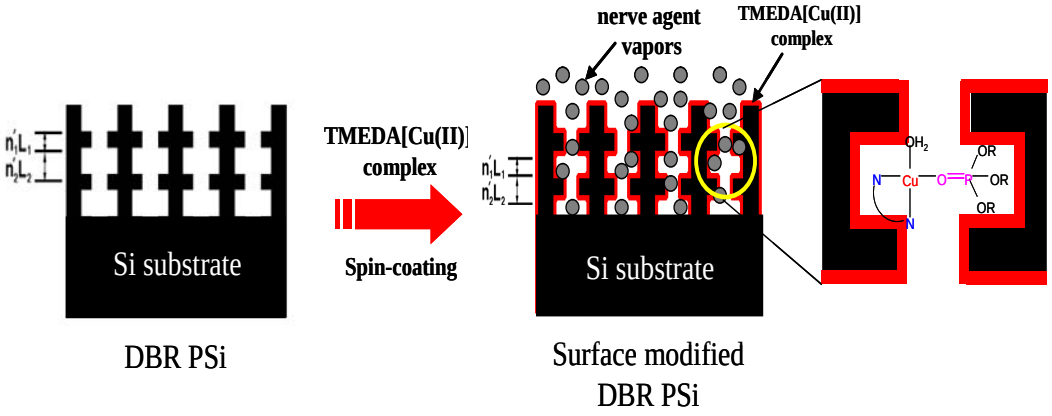

Figure 5.3. Schematic diagram of the sensing mechanism with surface-modified DBR PSi sample

Another DBR PSi sample was prepared using a periodic square wave current between 5 $mA \cdot cm^{-2}$ for 100 s and 50 $mA \cdot cm^{-2}$ for 3 s to match the emission wavelength of the LED (Ocean Optics, LED-520 and 590, FWHM = 15 nm) with its reflection band at 520, 590 nm. When the LED is used as the incident light source instead of the tungsten-halogen lamp, a dramatic decrease of the reflectivity, resulting from the red-shift, is observed in the reflectivity spectrum. Figure 5.4 shows reflectivity spectra recorded every 5 sec, in situ, while exposing DBR PSi to TEP vapor. A dramatic decrease (75%) of reflection intensity was observed within 15 sec for TEP as shown in Figure 5.4(A inset).

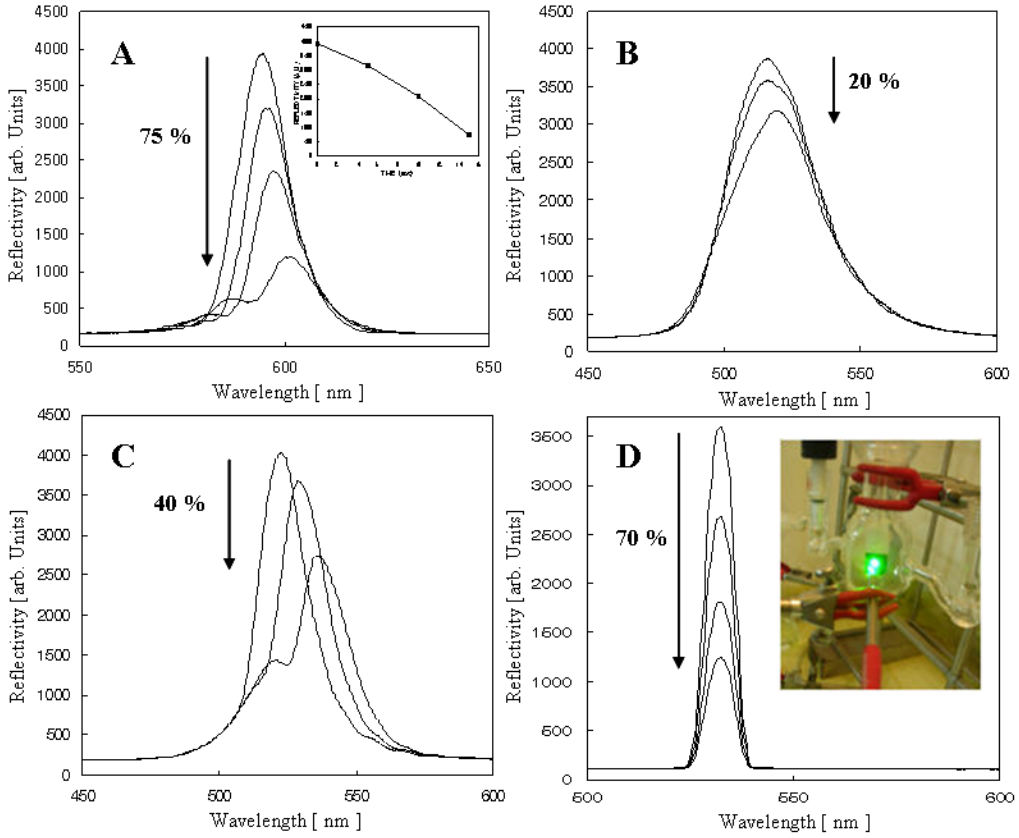

Figure 5.4. Reflectivity spectra of DBR PSi samples under a flux of TEP (A), DMMP (B), DEEP (C) in air when a LED (λ_{em} = 520, 590 nm) is used as a light source, and DMMP (D) in air when a laser (λ_{em} = 532 nm) is used as a light source.

When the tungsten-halogen lamp is used, the detection limit for TEP is about 1.5 ppm for 1 min. However, a detection limit of roughly 150 ppb for 15 sec. is obtained with the LED. Thus, the detection limit for organophosphonates has been greatly improved relative to previously reported methods [1,22].

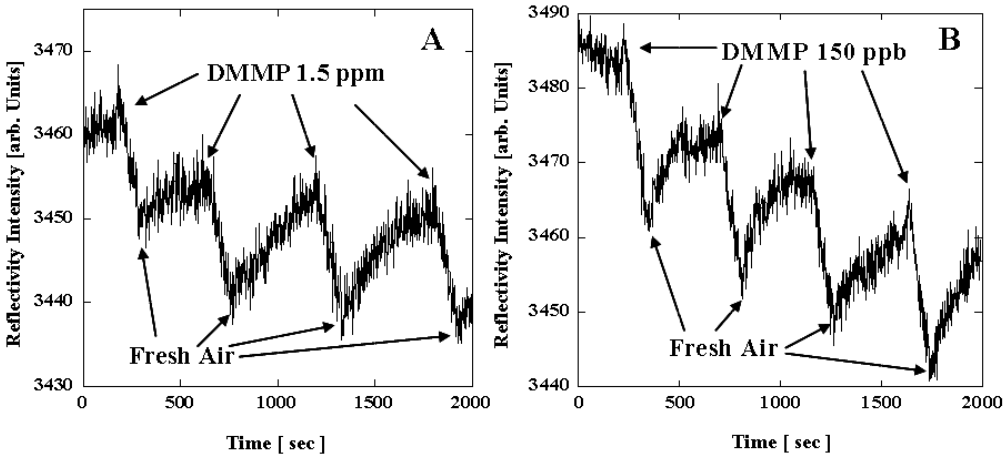

Figure 5.5. Plots for showing the detection limits of DMMP at 8.8 mg/m^3 (1.5 ppm) by using DBR PSi when a tungsten-halogen lamp is used as a light source and at 0.88 mg/m^3 (150 ppb) by using DBR PSi when LED and laser are used as a light source.

5.4 Conclusions

Various detection methods using multi-structured materials such as DBR and rugate PSi for sensing of G-type nerve agent simulants have been developed. The detection methods involve the shift of DBR PSi peaks in reflectivity spectra under the exposure of vapors of nerve agent simulants. Rapid detections have been achieved in few seconds, *in situ*, and observed by the red-shift of reflection peak resulted from the increase of refractive indices in PSi. The detection efficiency for nerve agent mimics is surprisingly increased when a light emitting diode (LED) and laser are used as an incident light source. The detection of organophosphonate nerve agents has been also achieved with DBR PSi samples containing copper (II) sulfate. Real-time detection for the nerve gases based on surface-functionalized DBR PSi with copper (II) sulfate indicates that the measurement is irreversible. Detection of DMMP vapors using laser (λ_{em} = 530 nm) as a light source was much faster and greater due to the narrower FWHM compared to LED light source by 2.5 times for 1 minute. Our detection limit (150 ppb) for DMMP vapors has been enhanced to a couple of hundreds times better previous other detection limits.

5.5 References

[1] H. Sohn, S. Letant, M. J. Sailor, and W. C. Trogler, *J. Am. Chem. Soc.* **122**, 5399 (2000).

[2] S. Chan, S. R. Horner, B. L. Miller, and P. M. Fauchet, *J. Am. Chem. Soc.* **123**, 11797 (2001).

[3] P. A. Snow, E. K. Squire, P. S. J. Russell, and L. T. Canham, *J. Appl. Phys.* **86**, 1781 (1999).

[4] C. Pacholski, M. Sartor, M. J. Sailor, F. Cunnin, and G. M. Miskelly, *J. Am. Chem. Soc.* **127**, 11636 (2005).

[5] L. T. Canham, M. P.Stewart, J. M. Buriak, C. L. Reeves, M. Anderson, E. K. Squire, P. Allcock, and P. A. Snow, *Phys. Status Solidi A.* **182**, 521 (2000).

[6] V. Lehmann, R. Stengl, H. Reisinger, R. Detemple, and W. Theiss, *Appl. Phys. Lett.* **78**, 589 (2001).

[7] T. A. Schmedake, F. Cunin, J. R. Link, and M. J. Sailor, *Adv. Mater.* **14**, 1270 (2002).

[8] F. Cunin, T. A, Schmedake, J. R. Link, Y. Y. Li, J. Koh, S. Bhatia, and M. J. Sailor, *Nat. Mater.* **1**, 39 (2002).

[9] M. S. Yoon, K. H. Ahn, R. W. Cheung, H. Sohn, J. R. Link, F. Cunin, and M. J. Sailor, *Chem. Commun*. 680 (2003).

[10] J. R. Dorvee, A. M. Derfus, S. N. Bhatia, and M. J. Sailor, *Nat. Mater*. **3**, 896 (2004).

[11] M. J. Sailor and J. R. Link, *Chem. Commun*. 1375 (2005).

[12] Y. Y. Li, F. Cunin, J. R. Link, T. Gao, R. E. Betts, S. H. Reiver, V. Chin, S. N. Bhatia, and M. J. Sailor, *Science* **299**, 2045 (2003).

[13] M. Thonissen and M. G. Berger, Multilayer Structures of Porous Silicon, in Properties of Porous Silicon, vol. 18, ed. L. Canham, Short Run Press Ltd, London, 1997, p. 30.

[14] Office of the special assistant for Gulf War Illness, Department of Defense, Fact Sheet on Exposure Limits for Sarin(GB), 1997.

[15] M. S. Nieuwenhuizen and J. L. N. Harteveld, *Sens. Actuators B.* **40**, 167 (1997).

[16] D. Williams and G. Pappas, *Field Anal. Chem. Technol.* **3**, 45 (1999).

[17] K. E. LeJeune, J. R. Wild, and A. J. Russell, *Nature* **395**, 27 (1998).

[18] E. S. Snow, F. K. Perkins, E. J. Houser, S. C. Badescu, and T. L. Reinecke, *Science* **307**, 1942 (2005).

[19] N. Taranenko, J.-P. Alarie, D. L. Stokes, and T. Vo-Dinh, *J. Raman Spectrosc*. **27**, 379 (1996).

[20] A. R. Hopkins, and N. S. Lewis, *Anal. Chem*. **73**, 884 (2001).

[21] S. E. Letant, S. R. Kane, B. R. Hart, M. Z. Hadi, T.-C. Cheng, V. K. Rastogi, and J. G. Reynolds, *Chem. Commun*. 851 (2005).

[22] J. Dorvee and M. J. Sailor, *Phys. Stat. Sol*. **202**, 1619 (2005).

[23] V. J. Novick, S. A. Johnson, H. A. Hisgen, and V. J. Reyes, *Rev. Sci. Instrum*. **70**, 1829 (1999).

Chapter Six
Fabrication and Characterization of Surface-functionalized DBR Smart Particles for the Detection of Bio-molecules

6.1 Introduction

The development of new technology, which can achieve at nanometer scale, to build such a device is of great interest, because it is too complex to fabricate by using conventional lithographic method. Since the discovery of PSi [1], it has been intensively investigated for a variety of applications such as chemical [2] and biological sensors [3], medical diagnostics [4], optical band pass filters [5], micro chemical reactors [6], and micro fuel cells [7] due to very high surface area as well as their unique photonic properties. Especially, optical devices based on multi-structured PSi have been brought to the attention of the scientists. Multilayer PSi such as DBR PSi [8-9] or rugate PSi [10-11] exhibit unique optical properties providing a reflection band at specific wavelength in the optical reflectivity spectrum. The direction of pores and pore diameters depend on surface orientation, doping level and type, temperature, the current density, and the composition of the etching solution [12]. DBR PSi as multi-layered PSi has been developed and typically prepared by an applying a square current waveform to the etch cell. DBR PSi resulted in two discrete indices and displayed photonic structure of Bragg filters. Chemical modification of PSi multilayer exhibited the modification of its physical, chemical, and electronic properties. Chemical or bio molecule can be

detected based on changes in the spectral interference pattern [13-14].

For applications in high throughput drug discovery and disease diagnostics, label-free biosensors would be important due to the advantage of easy sample preparation [15-16]. Two main optical transduction methods for label-free biosensors were both optical interferometric methods based on interferometers [17], evanescent wave devices [18], and grating couplers [19], and surface plasmon methods based on metal films [20] and colloids [21]. Biosensor based on PSi interferometer had a great advantage due to a large surface area matrix for immobilization of a variety of biomolecules such as enzymes [22], protein [23], and DNA fragments [24]. Sailor et al. recently reported that the electronic or optical properties of mono-layered PSi can be used as the transducer of biomolecular interaction in biosensor application [3]. In the present work, we have developed DBR smart particle biosensors based on surface-derivatized DBR PSi interferometer. The fabrication, optical characterization, and surface functionalized of biotin/silole-derivatized DBR smart particles were reported. The binding interaction with streptavidin was investigated for the application as a label-free biosensor.

6.2 Experiments

6.2.1 Preparation of DBR PSi Sample

DBR PSi samples were prepared by an electrochemical etch of heavily doped p^{++}-type silicon wafer (boron doped, polished on the <100> face, resistivity of 0.8~1.2 $m\Omega \cdot cm^{-2}$, Siltronix, Inc.). The etching solution consisted of a 3:1 volume mixture of aqueous 48% hydrofluoric acid (ACS reagent, Aldrich Chemicals) and absolute ethanol (ACS reagent, Aldrich Chemicals). Galvanostatic etch was carried out in a Teflon cell applying 30 cycles of a two-electrode configuration and performed in a dark room. DBR PSi was prepared by using a periodic pseudo-square wave current between 30 $mA \cdot cm^{-2}$ for 11 s and 300 $mA \cdot cm^{-2}$ for 1.5 s. All samples were then rinsed several times with ethanol and dried under argon atmosphere prior to use. The resulting DBR PSi were removed from the silicon substrate by an applying of electropolishing current at 460 $mA \cdot cm^{-2}$ for 100 s in a solution of 48% aqueous HF and ethanol (3:1 by volume) and 29 $mA \cdot cm^{-2}$ for 200 s in a solution of 48% aqueous HF and ethanol (1:15 by volume) to obtain a free-standing DBR PSi film.

6.2.2 Thermal Oxidation of Free-standing DBR PSi Film

Surface of a free-standing DBR PSi film was predominant hydride-terminated after the etching procedure. This surface was sensitive to oxidation and hydrolysis upon exposure to aqueous solution. Thermally oxidized DBR PSi samples were obtained by heat treatment in a furnace (Thermolyne F6270-26 furnace equipped

with controller) using the following parameters: intial ramp rate, 5℃/min to 300℃; hold time, 3 h; and passive cooling to ambient temperature.

6.2.3 Preparation of DBR Smart Particles

Preparation of DBR smart particles was accomplished by placing the oxidized DBR PSi films in 100 mL of ethanol in a Schlenk flask under argon atmosphere. The free-standing DBR PSi films were then made into particles by ultrasonic fracture in organic solution for 10 min. After removal of the solution, samples were rinsed with ethanol and acetone several times, dried under a reduced pressure, and stored in nitrogen atmosphere prior to use.

6.2.4 Synthesis of Biotin Tetrafluorophenyl Ester

For the biotinlylated DBR smart particles, biotin tetrafluorophenyl ester was prepared by previously known method [25]. Biotin (2.5 g, 10.22 mmol) was dissolved in 200 mL of warm (70℃) DMF under argon atmosphere. The solution was allowed to cool to room temperature. Triethylamine (2.5 mL, 20.5 mmol) was added, followed by an addition of 2,3,5,6-tetrafluorophenyl trifluoroacetate (4 g, 15.25 mmol). The reaction mixture was stirred at room temperature for 30 min. All volatiles were removed under reduced pressure. 100 mL of ether was added and the reaction mixture was filtered.

6.2.5 Surface Derivatization of Oxidized DBR Smart Particles

Dihydroxysilole (500 mg, 1.2 mmol) prepared by previously described method [26] and (3-aminopropyl)trimethoxysilane (1.8 mL, 10 mmol, 99%, Aldrich Chemicals) were dissolved in 50 mL of toluene. The oxidized DBR smart particles were added and refluxed for 24 h. After functionalization with amine and silole group, the sample was rinsed successively with acetone, dichloromethane, and ethanol and subsequently dried under a stream of nitrogen. Resulting DBR smart particles were incubated in biotin tetrafluorophenyl ester dissolved in triethylamine 20 mL at room temperature for 12 h. The sample was washed with acetone, dichloromethane, and ethanol and dried under argon gas.

6.2.6 Instruments and Data Acquisitions

FT-IR spectra were acquired with a Nicolet model 5700 FT-IR instrument in the diffuse reflectance mode (Spectra-Tech diffuse reflectance attachment). The FT-IR sample compartment was purged with nitrogen before each acquisition. The morphology of DBR smart particles was observed with cold field emission scanning electron microscope (FE-SEM, S-4800, Hitachi). Photoluminescence of silole/biotin-derivatized DBR smart particles was measured by Perkin-Elmer luminescence spectrometer LS 50B, and interferometric reflectance spectra were recorded by using an Ocean Optics S2000 spectrometer fitted with a bifurcated fiber optic probe. Spectra were recorded with a CCD detector in the wavelength range 400~1200 nm. The illumination of the surface as well as the measurement of the reflected light was performed along an axis coincident with the surface normal.

6.3 Results and Discussion

A DBR PSi exhibits a high reflectivity band with a Bragg wavelength λ_{Bragg}, depending on the thickness of the layers (d_1, d_2) and the corresponding refractive indices (n_1, n_2). The mth order of the Bragg peak is given by:

$$m\lambda_{Bragg} = 2(d_1n_1 + d_2n_2)$$

Multilayered DBR PSi prepared by applying a square current waveform exhibits high reflectivity in a specific narrow spectral region. The reflectivity can be tuned to appear anywhere in the visible to near-infrared spectral range, depending on the programmed etch waveform. The electrochemical process generates an optically uniform layer of PSi: the thickness and porosity of a given layer is controlled by the current density, the duration of the etch cycle, and the composition of the etchant solution. High current densities result in the desired well-defined macropores (diameter, d > 50 nm), rather than the random orientation of highly interconnected micropores (d < 2 nm). DBR PSi films have been removed from the silicon wafer by applying an electropolishing current and then ultrasonicated to create particles. Particles with sizes ranging from several hundred nanometers to few hundred micrometers were generated depending on the duration of ultrasonication. Figure 6.1 showed the SEM images of DBR PSi particles (so called "smart particle"). Size of DBR smart particle was about 20 ~ 40 micrometers. The surface image of DBR smart particles indicated that the pore size of particle retained a good porosity without destruction of porous structure during ultrasonication. The prepared DBR smart particles had cylindrical macropores with the average pore size of 100 nm, which could be suitable for the detection of streptavidin due to its size of 54×58

×48 Å [27].

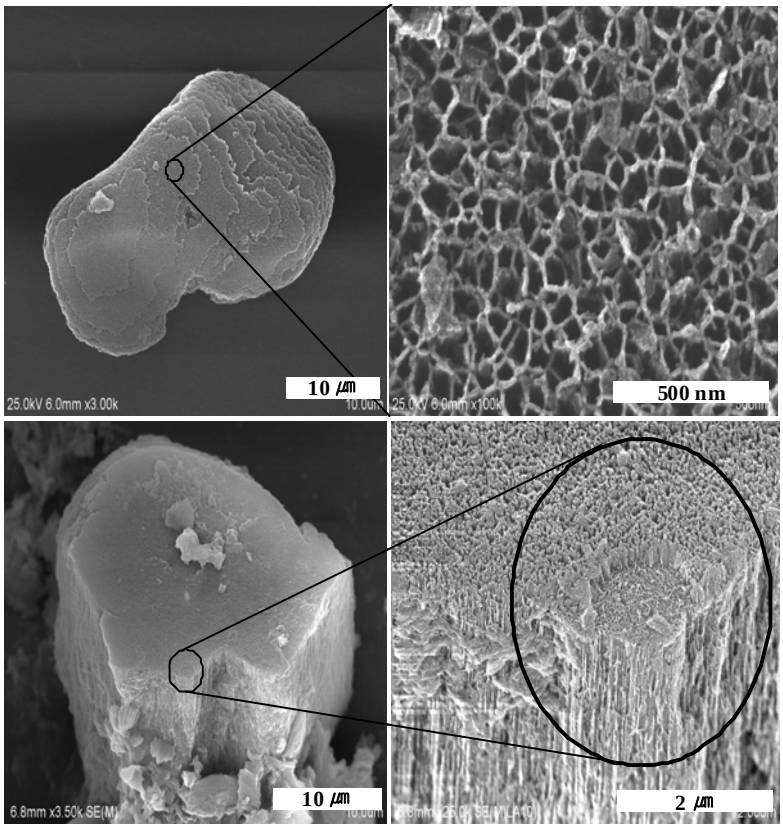

Figure 6.1. Surface and 3-dimensional images of DBR smart particle

Figure 6.2 describes the process for chemical functionalization of DBR smart particles with biotin terminated (3-aminopropyl)trimethoxysilane and dihydroxysilole. The thermal oxidation of DBR smart particles at 300℃ for 3 h converted the hydride-terminated surface into the hydroxyl terminated surface. Biotin terminated (3-aminopropyl)trimethoxysilane and dihydroxysilole were used for the surface modification of oxidized DBR smart particles for the detection of streptavidin.

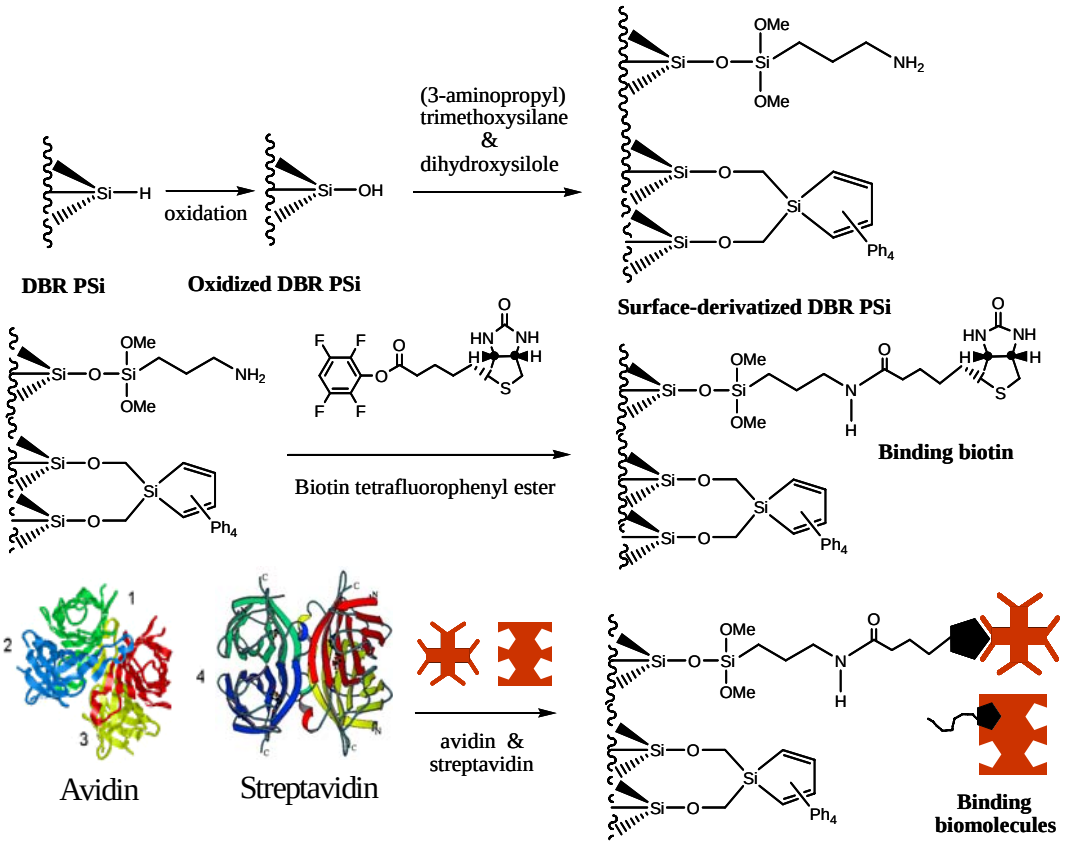

(continued)

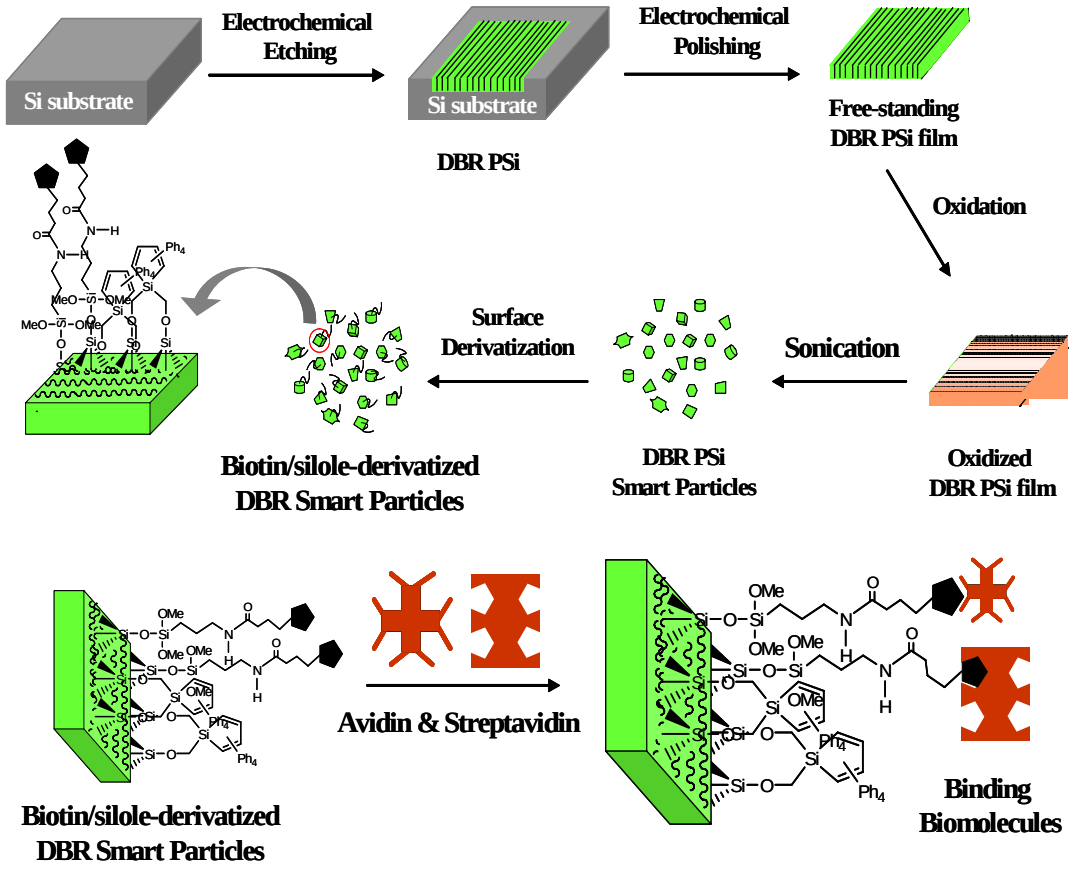

Figure 6.2. Schematic process for surface modification of DBR smart particles with biotin and silole groups

Figure 6.3 showed that biotin/silole-derivatized DBR smart particles displayed both photoluminescence (λ_{em} = 505 nm) with 360 nm of excitation wavelength and reflectivity (λ_{max} = 607 nm) under tungsten-halogen lamp. Photograph of samples demonstrated that biotin/silole-derivatized DBR smart particles exhibited dual optical properties.

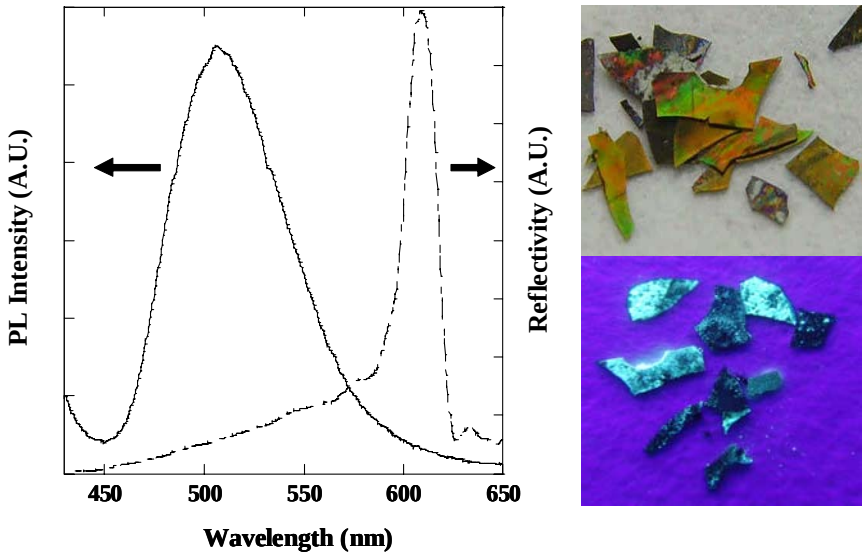

Figure 6.3. Optical reflectivity (dotted line) and photoluminescence (solid line) spectrum of biotin/silole-derivatized DBR smart particles. Photographs of biotin/silole-derivatized DBR smart particles under white light (top) and black light (bottom)

Diffuse reflectance FT-IR spectroscopy was used to monitor the oxidation and functionalization reaction of DBR smart particles sample. Figure 6.4A showed that the FT-IR spectrum of DBR smart particle immediately after an anodization of the silicon wafer displayed a characteristic broad band centered at 2115 and 908 cm^{-1} for the $\nu_{(Si-H)}$ stretching vibration and $\delta_{(Si-H)}$ bending vibration. After the thermal oxidation of DBR smart particles, the presence of silicon oxide was determined by FT-IR measurement as shown in Figure 6.4B. Thermal oxidation of the DBR smart particles resulted in the appearance of the characteristic large and broad Si-O-Si vibrational band around 1100 cm^{-1} in the FT-IR. The oxidized DBR smart particles exhibited vibrational bands characteristic of $\nu_{(OSi-H)}$ and $\delta_{(OSi-H)}$ vibratioal modes observed at 2277 and 883 cm^{-1}, respectively. Thermal oxidation of DBR smart particles led to a decrease of the Si-H vibrational band and the appearance of the OSi-H vibrational band. Condensation of the Si-OH surface of DBR smart particles with (3-aminopropyl)trimethoxysilane generated a surface-bound amino group. The FT-IR spectrum shown in Figure 6.4C displayed additional bands characteristic of the linker (the amide band of $\nu_{(N-H)}$ broad band centered at 3300 cm^{-1} and $\delta_{(N-H)}$ at 1579 cm^{-1} and the aliphatic $\nu_{(C-H)}$ stretching bands at 2858 and 2954 cm^{-1}). Surface derivatization led to complete the disappearance of the OSi-H vibrational band. The subsequent reaction with biotin as shown in Figure 6.2 led to the desired biotin-functionalized surface which was used in the avidin and streptavidin-binding studies (Figure 6.4D). The band at 1685 cm^{-1} was assigned to the carbonyl stretching vibration of the biotin head group.

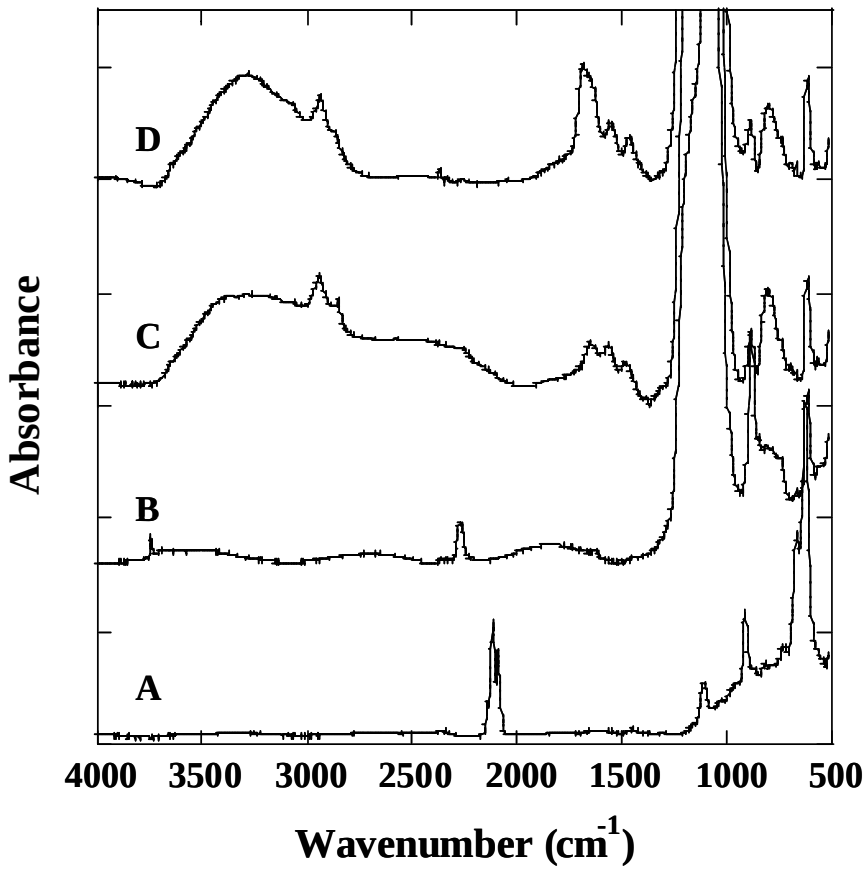

Figure 6.4. Diffuse reflectance FT-IR spectra of (A) a freshly etched DBR smart particle, (B) oxidized DBR smart particle at 300℃ for 3 h, (C) functionalized DBR smart particle with (3-aminopropyl)trimethoxysilane, and (D) subsequent reaction of the surface with biotin

Fresh DBR PSi displayed a very sharp line at 624 nm with sidelobes around the reflectance peak in the optical reflectivity spectrum as shown in Figure 6.5. The spectral bands of DBR smart particles had a full-width at half-maximum (FWHM) of about 20 nm. The thermal oxidation of DBR PSi resulted in the reflectivity at 580 nm shifted to shorter wavelengths by 44 nm due to the decrease of refractive index of silicon dioxide from silicon. Condensation of the Si-OH surface of DBR smart particles with (3-aminopropyl)trimethoxysilane generated a surface-bound amino group. The amine-functionalized DBR smart particles resulted in the reflectivity at 600 nm shifted to longer wavelengths by 20 nm due to the increase of refractive index upon introduction of the amine group into the pores of DBR smart particles. The subsequent reaction with biotin led to the desired biotin-funtionalized DBR smart particles which were used in the avidin and streptavidin-binding studies. The biotin-functionalized DBR smart particles resulted in the reflectivity at 610 nm shifted to longer wavelengths due to the increase of additional refractive index.

The surface functionalized DBR smart particles were placed in the flow cell. Aqueous phosphate buffer solution (PBS) was flushed to perform for an initial measurement of reflectivity. The surface was rinsed thoroughly with PBS buffer solution to ensure a covalent attachment to the surface and to check the stability of the reflectivity measurement. The biotin-functionalized DBR smart particles in PBS buffer solution resulted in the reflectivity at 665 nm shifted to longer wavelengths by 55 nm due to the increase of refractive index upon introduction of the PBS buffer solution into the pores of DBR smart particles.

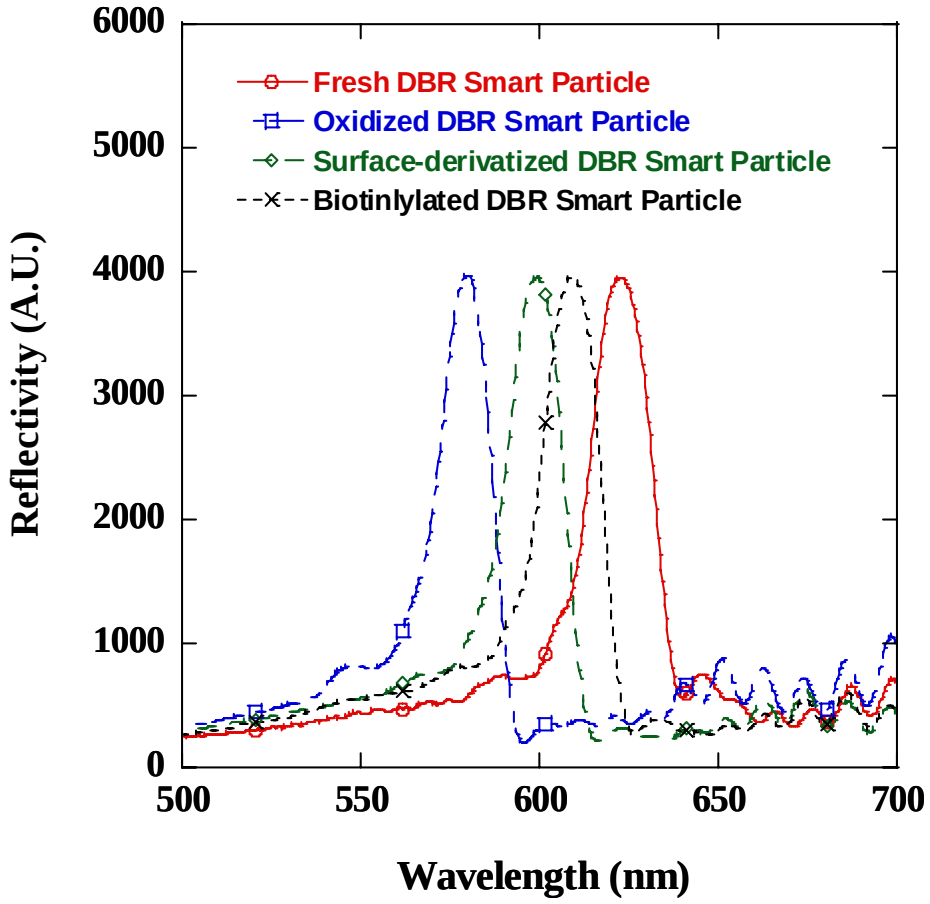

Figure 6.5. Optical reflectivity spectra of fresh, oxidized, surface-functionalized, and biotin derivatized DBR smart particle

The cell was then flushed with a constant flow rate of 0.8 mL/min of PBS containing avidin and streptavidin (20 μM), which coupled to the biotin-modified DBR smart particles surface. Figure 6.6 showed the change of reflection spectrum under the exposure of avidin and streptavidin to the biotin-functionalized DBR smart particles. An increase of the reflection wavelength in the reflectivity spectrum by 17 and 14 nm was observed, indicative of a change in refractive indices induced by binding of the avidin and streptavidin into the biotin-derivatized DBR smart particles, respectively. This increase was attributed to the replacement of some of the aqueous phase with avidin and streptavidin. The replacement changed the mean refractive indices of the DBR smart particles. They were observed as an increase of the reflection wavelength in the reflectivity.

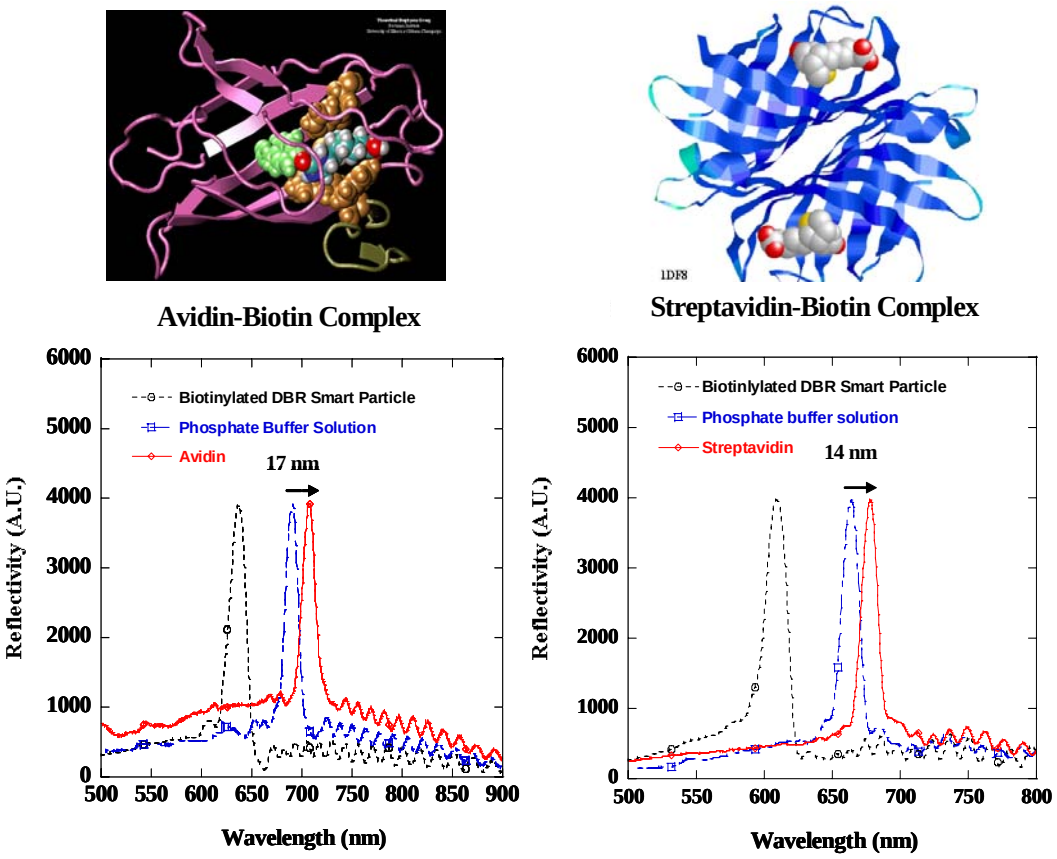

Figure 6.6. Sensing of avidin and streptavidin based on biotin derivatized DBR smart particle in PBS

6.4 Conclusions

Biotin/silole-derivatized DBR smart particles exhibiting dual optical properties such as photoluminescence (λ_{em} = 505 nm) and reflectivity (λ_{max} = 607 nm) for the detection of streptavidin were fabricated. Diffuse reflectance FT-IR spectroscopy was used to monitor the chemical and optical characterization of DBR smart particles during step-by-step functionalization of DBR smart particles surface. The reflection spectra of biotin-modified DBR smart particles were used in the avidin and streptavidin-binding studies. When the PBS buffer solution containing avidin and streptavidin was flushed into the biotin-functionalized DBR smart particle in the cell, a red-shift of reflectivity by 17 and 14 nm in the reflectivity spectrum was observed, respectively. This result indicated the binding of the avidin and streptavidin into the biotin-derivatized DBR smart particles.

6.5 References

[1] A. Uhlir, *Bell System Tech*. **35**, 333 (1956).

[2] H. Sohn, S. Letant, M. J. Sailor, and W. C. Trogler, *J. Am. Chem. Soc*. **122**, 5399 (2000).

[3] V. S.-Y. Lin, K. Motesharei, K.-P. S. Dancil, M. J. Sailor, and M. R. Ghadiri, *Science* **278**, 840 (1997).

[4] M. Simion, I. Kleps, T. Neghina, A. Angelescu, M. Miu, A. Bragaru, M. Danila, E. Condac, M. Costache, and L. Savu, *J. Alloy. Compd*. **434**, 830 (2007).

[5] S. Ilyas, T. Böcking, K. Kilian, P. J. Reece, J. Gooding, K. Gaus, and M. Gal, *Opt. Mater*. **29**, 619 (2007).

[6] M. A. Khan, M. S. Haque, H. A. Naseem, W. D. Brown, and A. P. Malshe, *Thin Solid Films*. **332**, 93 (1998).

[7] S. E. Lêtant, S. Content, T. T. Tan, F. Zenhausern, and M. J. Sailor, *Sensor Actuat. B.* **69**, 193 (2000).

[8] B.-J. Lee, S. Jang, and H. Sohn, *Solid State Phenom*. **124-126**, 491 (2007).

[9] J. Kim, Y. Koh, S. Jang, Y. C. Ko, H. -G. Woo, and H. Sohn, *J. Nanosci. Nanotechnol.* **7**, 4165 (2007).

[10] J. Park, S. Cho, Y. C. Ko, and H. Sohn, *J. Korean Phys. Soc.* **50**, 695 (2007).

[11] S. Jang, J. Kim, Y. Koh, Y. C. Ko, H.-G. Woo, and H. Sohn, *J. Nanosci. Nanotechnol.* **7**, 4049 (2007).

[12] R. L. Smith and S. D. Collins, *J. Appl. Phys.* **71**, R1 (1992).

[13] A. Janshoff, K.-P. S. Dancil, C. Steinem, D. P. Greiner, V. S. Lin, C. Gurtner, K. Motesharei, M. J. Sailor, and M. R. Ghadiri, *J. Am. Chem. Soc.* **120**, 12108 (1998).

[14] B.-J. Lee, S. G. Kim, and H. Sohn, *Key Eng. Mater.* **321-323**, 53 (2006).

[15] A. Brecht and G. Gauglitz, *Sensor. Actuat. B.* **38**, 1 (1997).

[16] J. Janata, M. Josowicz, and D. M. Devaney, *Anal. Chem.* **66**, 207R (1994).

[17] J. Piechler, A. Brandenburg, A. Brecht, E. Wagner, and G. Gauglitz, A*ppl. Opt.* **36**, 6554 (1997).

[18] A. P. Abel, M. G. Weller, G. L. Duveneck, M. Ehart, and H. M. Widmer, *Anal. Chem.* **68**, 2905 (1996).

[19] R. Polzius, E. Diessel, F. F. Bier, and U. Bilitewski, *Anal. Biochem.* **248**, 269 (1997).

[20] J. Homola, S. S. Yee, and G. Gauglitz, *Sensor. Actuat. B.* **54**, 3 (1999).

[21] P. I. Nikitin, A. A. Beloglazov, V. E. Kochregin, M. V. Valeiko, and T. I. Ksenevich, *Sensor. Actuat. B.* **54**, 43 (1999).

[22] J. Drott, K. Lindstrom, L. Rosengren, and T. J. Laurell, *Micromech. Microeng.* **7**, 14 (1997).

[23] T. Laurell, J. Drott, L. Rosengern, and K. Lindstrom, *Sensor. Actuat. B.* **31**, 161 (1996).

[24] K. L. Beattie, W. G. Beattie, L. Mengm S. L. Turner, R. Coral-Vazquez, D. D. Sith, P. M. Mclntyre, and D. D. Dao, *Clin. Chem.* **41**, 700 (1995).

[25] H. B. Gamper, M. W. Reed, T. Cox, J. S. Virosco, A. D. Adams, A. A. Gall, J. K. Scholler, and R. B. Meyer, *Nucleic Acids Res.* **21**, 145 (1993).

[26] I. Toulokhonovat, R. Zhao, M. Kozee, and R. West, *Main Group Met. Chem.* **24**, 737 (2001).

[27] W. A. Hendrickson, A. Pahler, J. L. Smith, Y. Satow, E. A. Merritt, and R. P. Phizackerley, *Proc. Natl. Acad. Sci.* **86**, 2190 (1989).

Part II.

Fluorescent Sensors Based on Nanoaggregates and Nanoparticles Containing Silicon and Germanium

Chapter Seven
Introduction of Organosilicon Chemistry

7.1 What is Organometallic Chemistry?

Organometallic chemistry is the study of chemical compounds containing bonds between carbon and a metal [1]. Since many compounds without such bonds are chemically similar, an alternative may be compounds containing metal-element bonds of a largely covalent character. Organometallic chemistry combines aspects of inorganic chemistry and organic chemistry.

Organometallic compounds are also known as organo-inorganics, metallo-organics and metalorganics. Organometallic compounds are distinguished by the prefix "organo-" e.g., organopalladium compounds. Examples of such organometallic compounds include all Gilman which contain lithium and copper. Tetracarbonyl nickel, and ferrocene are examples of organometallic compounds containing transition metals. Other examples include organomagnesium compounds like iodo(methyl)magnesium MeMgI, diethylmagnesium (Et_2Mg), and all Grignard reagents; organolithium compounds such as butyllithium (BuLi), organozinc compounds such as chloro(ethoxycarbonylmethyl)zinc ($ClZnCH_2C(=O)OEt$); and organocopper compounds such as lithium dimethylcuprate ($Li^+[CuMe_2]^-$).

In addition to the traditional metals, lanthanides, actinides, and semimetals, elements such as boron, silicon, arsenic, and selenium are considered to form organometallic compounds, e.g., organoborane compounds such as triethylborane (Et_3B).

7.2 History of Organometallic Chemistry

Early developments in organometallic chemistry include Louis Claude Cadet's synthesis of methyl arsenic compounds related to cacodyl, William Christopher Zeise's platinum-ethylene complex, Edward Frankland's discovery of dimethyl zinc, Ludwig Mond's discovery of $Ni(CO)_4$, and Victor Grignard's organomagnesium compounds. The abundant and diverse products from coal and petroleum led to Ziegler-Natta, Fischer-Tropsch, hydroformylation catalysis which employ CO, H_2, and alkenes as feedstocks and ligands.

Recognition of organometallic chemistry as a distinct subfield culminated in the Nobel Prizes to Ernst Fischer and Geoffrey Wilkinson for work on metallocenes. In 2005, Yves Chauvin, Robert H. Grubbs and Richard R. Schrock shared the Nobel Prize for metal-catalyzed olefin metathesis.

1760	Louis Claude Cadet de Gassicourt investigates inks based on Cobalt salts and isolates Cacodyl from cobalt mineral containing arsenic.
1827	Zeise's salt is the first platinum/olefin complex.
1863	Charles Friedel and James Crafts prepare organochlorosilanes.
1890	Ludwig Mond discovers Nickel carbonyl.
1899	Introduction of Grignard reaction.
1900	Paul Sabatier works on hydrogenation organic compounds with metal catalysts.
1909	Paul Ehrlich introduces Salvarsan for the treatment of syphilis, an early arsenic based organometallic compound.
1912	Nobel Prize Victor Grignard and Paul Sabatier.
1930	Henry Gilman works on lithium cuprates.
1963	Nobel prize for Karl Ziegler and Giulio Natta on Ziegler-Natta catalyst.
1965	Discovery of cyclobutadieneiron tricarbonyl.
1968	Heck reaction.
1973	Nobel prize Geoffrey Wilkinson and Ernst Otto Fischer on sandwich compounds.
2005	Nobel prize Yves Chauvin, Robert Grubbs, and Richard Schrock on metal-catalyzed alkene metathesis.

Table 7.1. Organometallic chemistry timeline

7.3 Classification of Organometallic Chemistry

Period 2 elements	organolithium chemistry, organoberyllium chemistry, organoborane chemistry.
Period 3 elements	organomagnesium chemistry, organoaluminum chemistry, **organosilicon chemistry**.
Period 4 elements	organotitanium chemistry, organochromium chemistry, organomanganese chemistry, organoiron chemistry, organocobalt chemistry, organonickel chemistry, organocopper chemistry, organozinc chemistry, organogallium chemistry, **organogermanium chemistry**.
Period 5 elements	organopalladium chemistry, organosilver chemistry, organocadmium chemistry, organoindium chemistry, organotin chemistry.
Period 6 elements	organoplatinum chemistry, organogold chemistry, organomercury chemistry, organothallium chemistry, organolead chemistry.

Table 7.2. Classification of organometallic chemistry

7.4 Organosilicon Chemistry

Even after more than 100 years of history, organosilicon Chemistry is arguably still one the most significant and diverse research areas of chemistry. The last ten years have witnessed tremendous advances and breakthroughs. Significant new applications in organic synthesis and medicinal chemistry have been developed.

Organosilicon compounds are organic compounds containing carbon silicon bonds. Organosilicon chemistry is the corresponding science exploring their properties and reactivity [2]. Like carbon, the organically bound silicon is tetravalent and tetrahedral. Carbon-silicon bonds are not found in any biomolecule [3]. The first organosilicon compound, tetraethylsilane was discovered by Charles Friedel and James Crafts in 1863 by reaction of tetrachlorosilane with diethylzinc. The carbosilicon silicon carbide is an inorganic compound.

7.4.1 Organosilanes

Carbon silicon bonds compared to carbon carbon bonds are longer (186 pm *vs* 154 pm) and weaker with bond dissociation energy 451 kJ/mol *vs* 607 kJ/mol. The C-Si is somewhat polarized towards carbon due to its higher electronegativity (C=2.55 *vs* Si=1.90). One manifestation of bond polarization in organosilanes is found in the Sakurai reaction. In oxidative couplings silicon is represented by the Hiyama coupling. Certain alkyl silanes can be oxidized to an alcohol in the Fleming-Tamao oxidation. The chemistry of silanes such as tetramethylsilane is comparable to that of alkanes in many aspects such as thermal stability. The β-silicon effect describes the stabilizing effect of a β-silicon atom on a carbocation with many implications for reactivity.

7.4.2 Siloxides

More notably bonds of silicon to oxygen are much shorter and stronger (809 compared to 538 kJ/mol) than that of those of carbon to oxygen. The polarization in this bond increases towards oxygen. Examples are silyl acetals $RR'Si(OR)_2$, the siloxanes and the polymeric polysiloxanes. Silyl ethers are extensively used as protective groups for alcohols. The favorable formation of Si-O bonds drive many organic reactions such as the Brook rearrangement and Peterson olefination.

Another manifestation is the highly explosive nature of the silicon pendant $Si(CH_2ONO_2)_4$ and $Si(CH_2N_3)_4$ of pentaerytritol tetranitrate [4]:

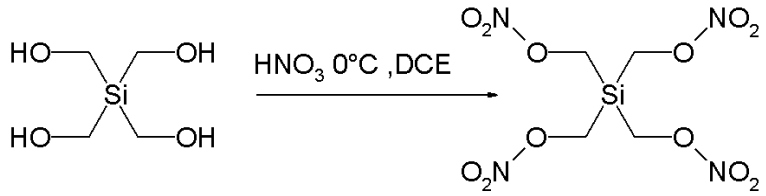

7.4.3 Silyl Halides

Organosilyl halides are important reagents in organic chemistry notably trimethylsilyl chloride Me_3SiCl. A classic method called the Flood reaction for the synthesis of this compound class is by heating hexaalkyldisiloxanes $R_3SiOSiR_3$ with concentrated sulfuric acid and a sodium halide [5]. Other relevant silyl halides are dichloromethylphenylsilane **1**, dimethyldichlorosilane **2**, methyltrichlorosilane **3**, trimethylchlorosilane **4**, trichloroethylsilane **5**, trichloro(chloromethyl)silane **6**, (4-aminobutyl)diethoxymethylsilane **7**, trichloro(dichlorophenyl) silane **8**, trichloro phenylsilane **9**. as shown in Figure 7.1.

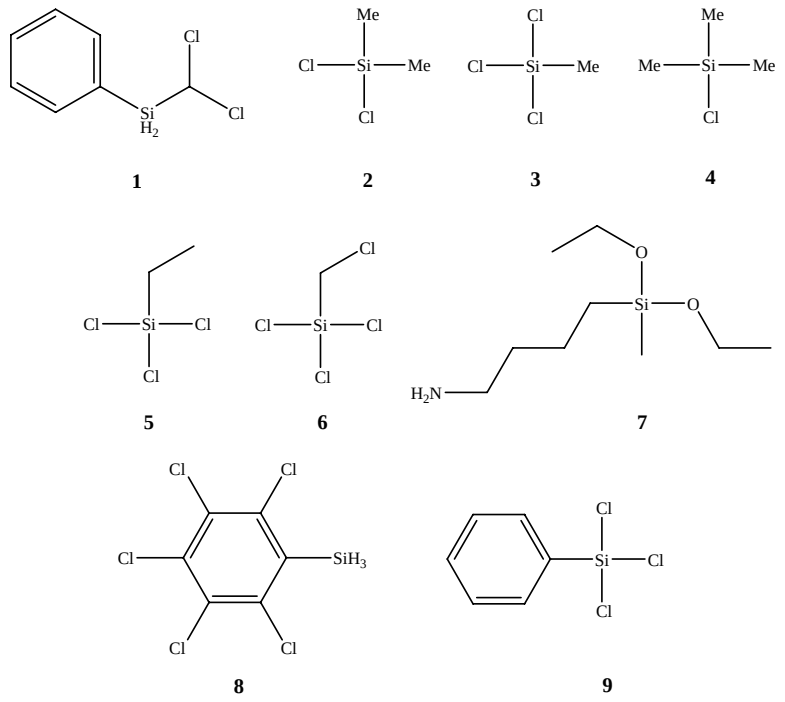

Figure 7.1. Structures of silyl halides

7.4.4 Silyl Hydrides

The silicon to hydrogen bond is longer than the C-H bond (148 compared to 105 pm) and weaker (299 compared to 338 kJ/mol). Hydrogen is more electronegative than silicon hence the naming convention of silyl hydrides. Silyl hydrides are very reactive and used as reducing agents for example polymethylhydrosiloxane (PMHS).

In one study triethylsilylhydride is used in the conversion of an phenyl azide to an aniline [6]:

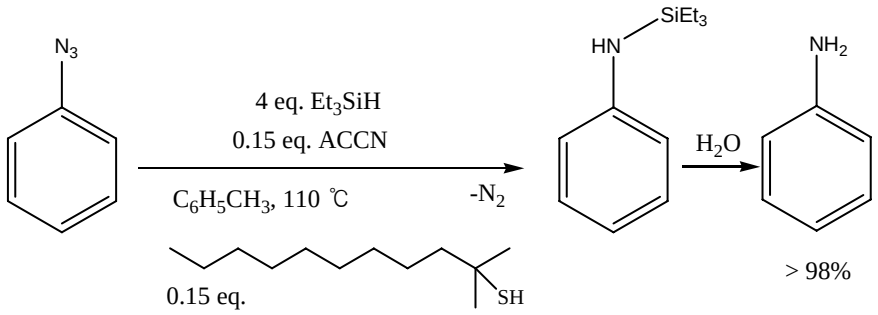

7.4.5 Hydrosilylation

Silyl hydrides react with various unsaturated substrates such as alkenes, alkynes, imines, carbonyls and oximes to new organosilicon compounds in hydrosilylation. In the reaction of triphenylsilyl hydride with phenylacetylene the reaction product is a trans or cis or the geminal vinyl silane, for example [7]:

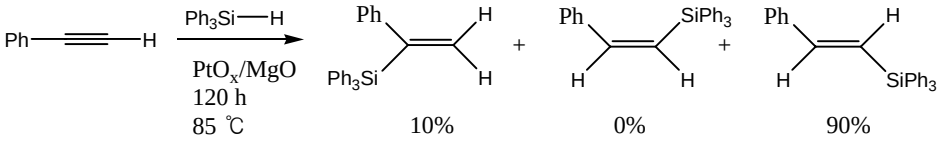

10% 0% 90%

Ph = 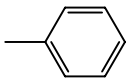

In the related silylmetalation, a metal replaces the hydrogen atom.

7.4.6 Silenes

Organosilicon compounds unlike their carbon counterparts do not have a rich double bond chemistry due to the large difference in electronegativity. Existing compounds with organosilene Si=C bonds are laboratory curiosities such as the silicon benzene analogue silabenzene, and Si=Si bond containing disilenes. Disilenes are compounds containing a silicon-silicon double bond and are considered to be heavier analogues of alkenes. They are sometimes also called disilaalkenes. The first transient disilene was synthesized in 1972 by D. N. Roark and Garry J. D. Peddle. The first thermally stable disilene, tetramesityldisilene, was isolated in 1981 by Robert West and coworkers [8].

7.4.7 Siloles

Siloles, silacyclopentadienes, are well established since the pioneering work of Braye and Hübel in 1959, their unique electronic structure has stimulated much research in recent years [9]. Siloles are the silicon pendants of pyrroles and of current academic interest due to their electroluminescence and other electronic properties. Silole is a silicon-containing five-membered cyclic diene, that is a silicon analog of cyclopentadiene. There have been extensive studies on the synthesis, reactivities, properties and coordination abilities of such compounds to transition metals, and the aromaticity of their anionic or cationic species. The most notable feature of siloles is their high electron-accepting property, associated with their low-lying LUMOs. Potential applications of silole span a wide range, including electron-transporting materials, electroluminescent (EL) devices, and electronic sensors. A general review on siloles by Yamaguchi and Tamao is available [10]. More specialized reviews on aromatic silole anions and polymeric siloles have been written by Saito and Yoshioka in 2005 and by Dyer *et al.* in 2003 [11-12].

7.5 Introduction of Siloles

7.5.1 Unique electronic structure of silole

According to the theoretical calculation of Tamao's group [13], silole has a quite different electronic structure from that of cyclopentadiene [14-18]. *Ab initic* calculatioans at the HF/6-31G* level of theory show that, while the HOMO of the parent silole is about 0.4 eV lower than that of the parent cyclopentadiene, the LUMO level of the silole is more than 1.2 eV lower in comparison with that of cyclopentadiene as shown in Figure 7.2.

The difference in their LUMO levels is due to the unique orbital interaction in the silole ring, as shown in Figure 7.3. When the molecular orbital of silole is constructed by orbital interaction of MOs of a silylene moiety and a butadiene moiety, the low-lying LUMO of silole arises from mixture of the σ^* orbital of the silylene moiety with the π^* orbital of the butadiene moiety, *i.e.*, σ^*-π^* conjugation. It should be noted that the σ^* orbital on the silicon and the lobes of π^* orbital on the adjacent carbons are in phase. This orbital interaction takes place effectively due to the fixed perpendicular arrangement of the plane of the silylene moiety, *i.e.* the plane involving two exocyclic σ bonds of the silole, to the plane of the butadiene moiety and to the energetically comparable σ^* and π^* orbitals. In the case of cyclobutadiene the σ^*-π^* conjugation in the LUMO is almost negligible because of the much higher energy level of the corresponding exocyclic σ^* orbital.

The shape of the LUMO of silole is visualized in Figure 7.4, together with that of cyclopentadiene for comparison.

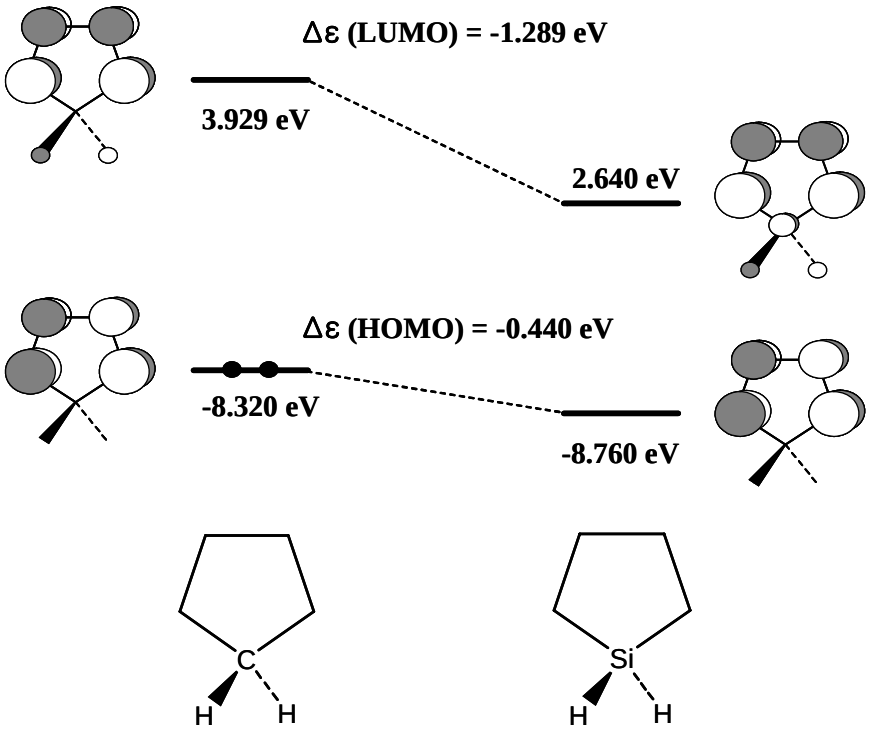

Figure 7.2. Releative energy levels of the HOMO and LUMO for silole and cyclobutadiene, based on the HF/6-31G* calculations

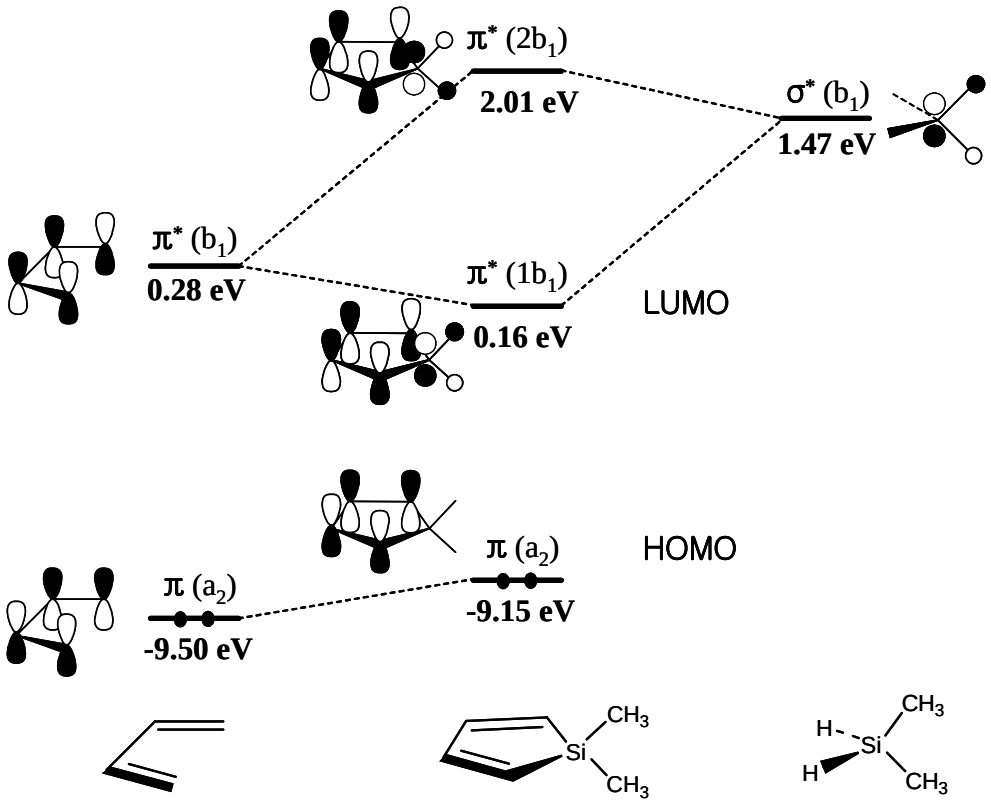

Figure 7.3. Orbital correlation diagram for 1,1-dimethylsilole, based on the PM3 calculations

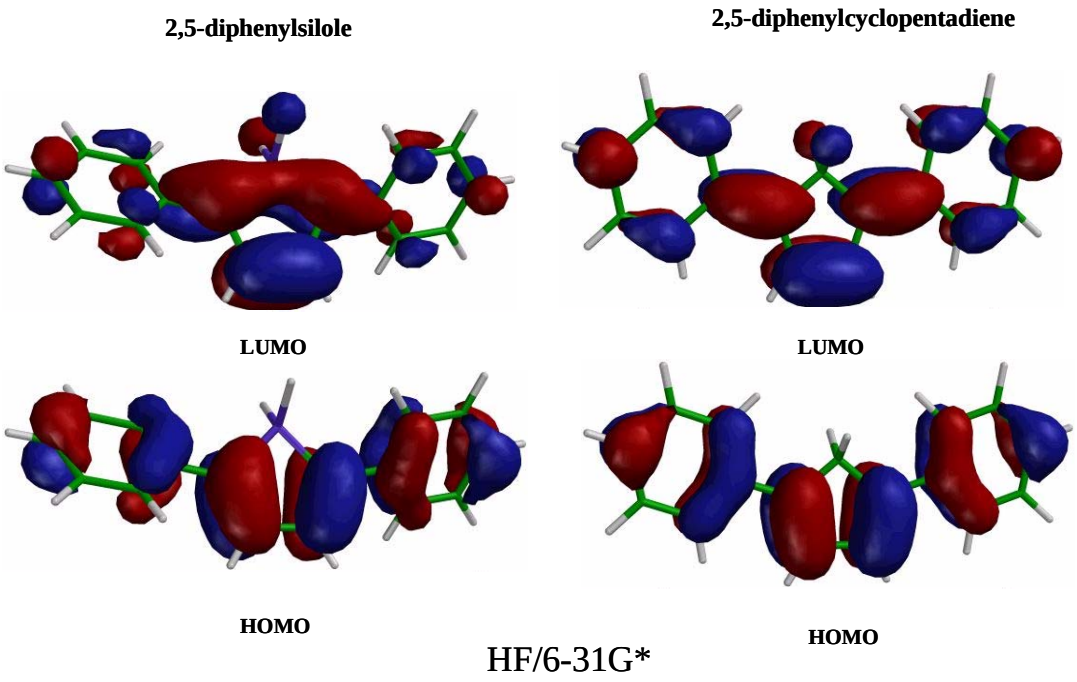

Figure 7.4. Shape of the HOMO and LUMO of silole and cyclopentadiene

7.5.2 Various silole derivatives

Siloles containing phenyl groups are synthesized best starting from diphenylacetylene and lithium, which affords 1,4-dilithio-1,2,3,4-tetraphenylbutadiene that readily react with the chlorosilanes $SiCl_4$, Me_2SiCl_2, Ph_2SiCl_2, and $PhSiCl_3$ to produce the siloles **1**-**4** (Scheme 7.1). Siloles containing methyl groups, such as **5**, are accessible upon metallation of 1,4-diiodo-1,2,3,4-tetramethylbutadiene providing the corresponding dilithio compound that may be reacted with chlorosilanes, such as $SiCl_4$ (Scheme 7.1). The 2,5-dilithiated 1,1-bis(diethylamino)silole **6** is available by the reduction of bis(phenylethynyl)silane **7** with lithium naphthalenide (Scheme 7.1). The subsequent reaction of **6** with trimethylchlorosilane and simethyl sulfate provides access to the 1,1-bis(diethylamino)siloles **8** and **9**, having trimethylsilyl and methyl groups in vicinal positions (Scheme 7.1).

The 1,1-bis(diethylamino)siloles **8** and **9**, are excellent precursors for the synthesis of other 1,1-difunctionalized-siloles (Scheme 7.2) [19]. the reaction of **8** and **9** with $EtOH/AlCl_3$ and HCl produces the siloles **10** and **11** containing ethoxy groups or chlorine atoms attached to the silicon. The 1,1-dichlorosiloles **12** and **13** have been converted into the corresponding 1,1-difluorosiloles **14** and **15** with ZnF_2. Hydrolysis of **13** and **15** yields the fluorosilanol **16** and the silanediol **17**, respectively (Scheme 7.2).

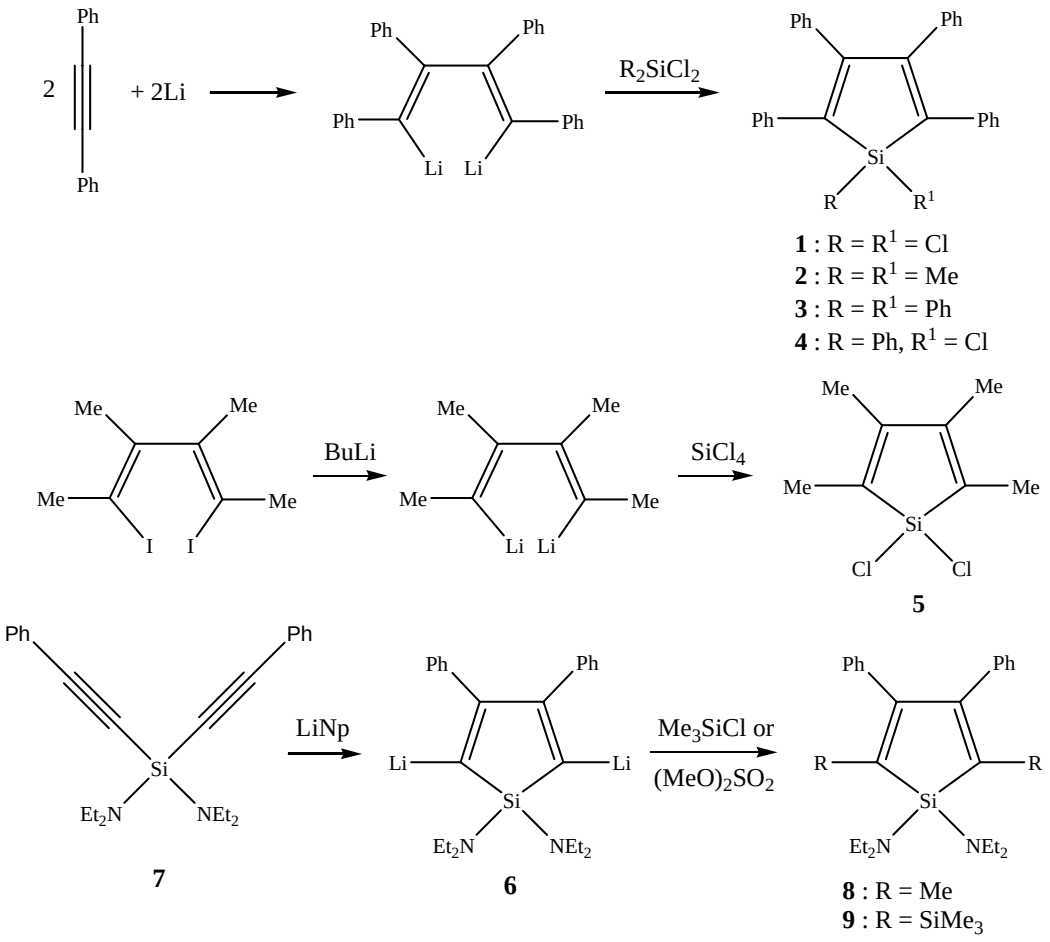

Scheme 7.1. Synthetic route of silole and silole derivatives **1-9**

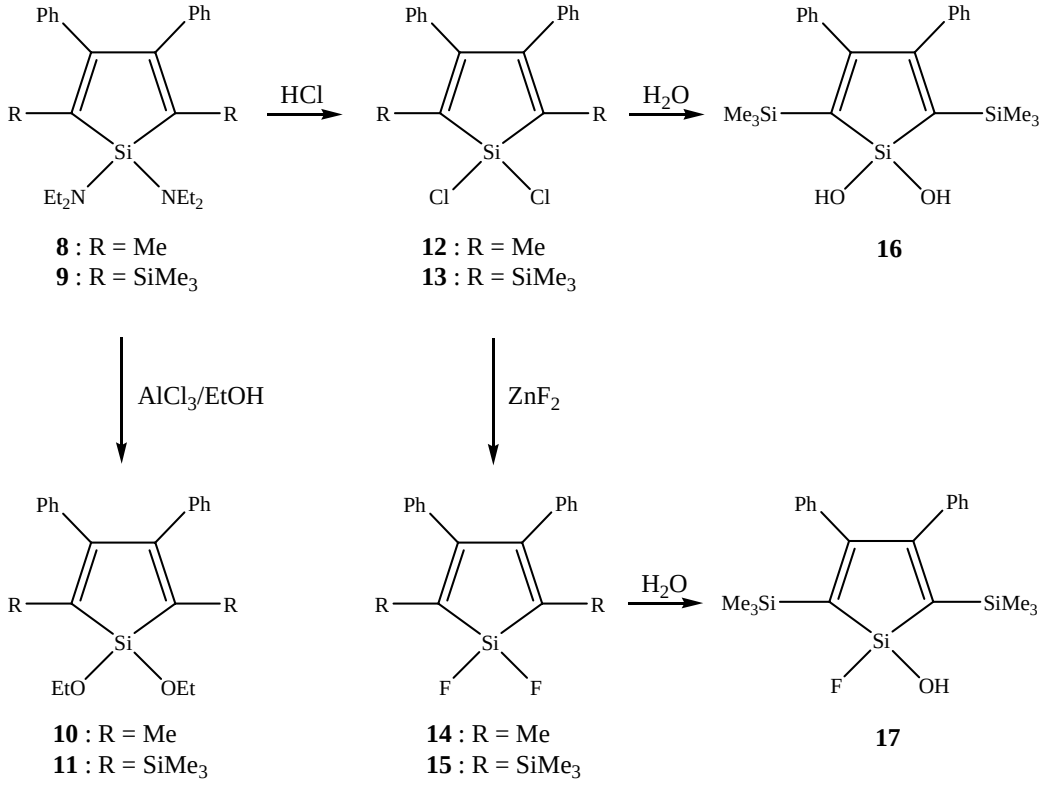

8 : R = Me
9 : R = $SiMe_3$

12 : R = Me
13 : R = $SiMe_3$

16

10 : R = Me
11 : R = $SiMe_3$

14 : R = Me
15 : R = $SiMe_3$

17

Scheme 7.2. Synthetic route of silole and silole derivatives **10-17**

The perphenylated 1,1-dichlorosilole **1** is also a versatile starting material for the prepararion of new silole derivatives (Scheme 7.3). The reaction of **1** with the metallated acetylene derivatives PhCCLi and HCCMgBr provides access to the siloles **18** and **1**9 containing ethynyl groups, whereas the careful hydrolysis with $NaHCO_3$ affords the silandiol **20** [20].

The reduction of **1** with $LiAlH_4$, sodium (short reaction time), and lithium (long reaction time) gives rise to formation of the dihydride **21**, the polysilole **22** having terminal chlorine atoms [21], and the lithium disilanide **23**, respectively [22-24].

The silole dianions are believed to be aromatic. The negative charge of **23** is partly distributed over the delocalized π-electron system, explaining the high electron-accepting property and the partial silylenoide character of the silicon atom. The catalytic dehydrocoupling of **21** using H_2PtCl_6 and $RhCl(PPh_3)_3$ gives access to low molecular weight polysilols **24** having terminal hydrogen atoms [25].

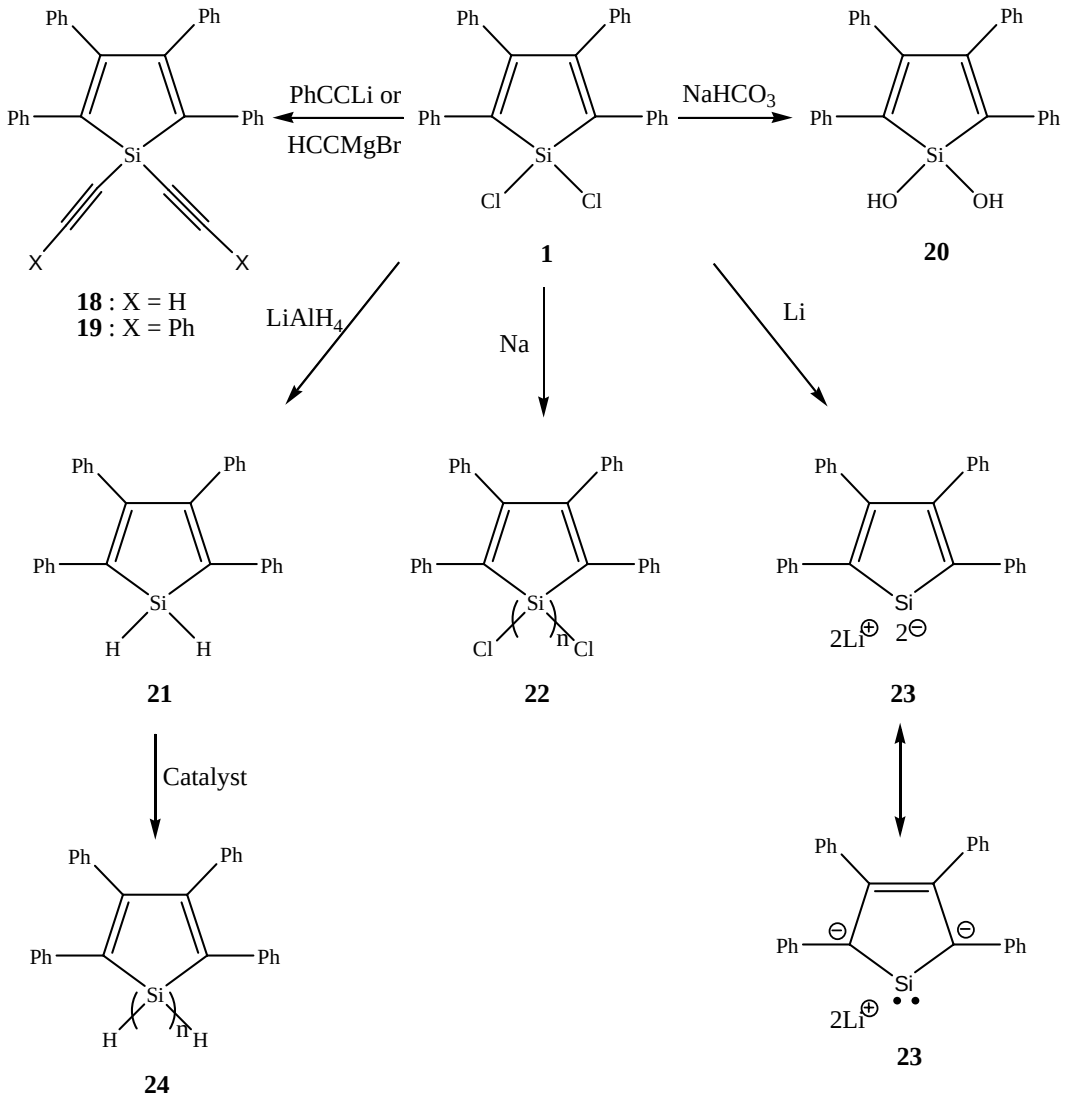

Scheme 7.3. Synthetic route of silole and silole derivatives **18-23**

7.6 Refernces

[1] R. H. Crabtree, The Organometallic Chemistry of the Transition Metals, Wiley, 560 (2005).

[2] C. E. Butterworth, Silicon in Organic Synthesis, London (1981).

[3] S. Pawlenko, Organosilicon Chemistry, Walter de Gruyter, New York (1986).

[4] T. M. Klapotke, B. Krumm, R. Ilg, D. Troegel, and R. Tacke, *J. Am. Chem. Soc.* **129**, 6908 (2007).

[5] E. A. Flood, *J. Am. Chem. Soc.* **55**, 1735 (1933).

[6] L. Benati, G. Bencivenni, R. Leardini, M. Minozzi, D. Nanni, R. Scialpi, P. Spagnolo, and G. Zanardi, *J. Org. Chem.* **71**, 5822 (2006).

[7] E. Ramirez-Oliva, A. Hernandez, J. Martinez-Rosales, A. Aguilar-Elguezabal, G. Herrera-Perez, and J. Cervantesa, *Arkivoc* 126 (2006).

[8] R. West, M. J. Fink, J. Michl, *Science* **214**, 1343 (1981).

[9] E. H. Braye and W. Hübel, *Chem. Ind.* 1250 (1959).

[10] S. Yamaguchi, R.-Z jin, and K. Tamao, *J. Chem. Soc., Dalton Trans.* 3693 (1998).

[11] M. Hissler, P. W. Dyer, and R. Reau, *Coord. Chem. Rev.* **1**, 244 (2003).

[12] M. Saito and M. Yoshioka, *Coord. Chem. Rev.* **249**, 765 (2005).

[13] S. Yamaguchi and K. Tamao. *Bull. Chem. Soc. Jpn.* **69**, 2327 (1996).

[14] V. Niessen, W. P. Kraemer, and L. S. Ceberbaum, *Chem. Phys.* **11**, 385 (1975).

[15] M. S. Gordon, P. Boudjouk, and F. Anwari, *J. Am. Chem. Soc.* **105**, 4972 (1983).

[16] C. Guimon, G. Pfister-Guillouzo, J. Dubac, A. Laporterie, G. Manuel, and H. Iloughmane, *Organometallics* **4**, 636 (1985).

[17] J. R. Damewood, *J. Org. Chem.* **51**, 5028 (1986).

[18] V. N. Khabashesku, S. E. Balaji, V. Boganov, O. M. Nefedov, and J. Michl, *J. Am. Chem. Soc.* **116**, 320 (1994).

[19] S. Yamaguchi, R.-Z jin, K. Tamao, and M. Shiro, *Organometallics* **16**, 2230 (1997).

[20] I. Toulokhonova, R. Zhao, M. Kozee, and R. West, *Main Group Met. Chem.* **24**, 737 (2001).

[21] H. Sohn, R. R. Huddleston, D. R. Powell, R. West, K. Oka, and X. Yonghua, *J. Am. Chem. Soc.* **121**, 2935 (1999).

[22] R. West, H. Sohn, U. Bankwitz, J. Calabrese, Y. Apeloig, and T. Müller, *J. Am. Chem. Soc.* **117**, 11608 (1999).

[23] R. West, H. Sohn, D. R. Powell, T. Müller, and Y. Apeloig, *Angew. Chem. Int. Ed.* **35**, 1002 (1996).

[24] Y. Liu, D. Ballweg, and R. West, *Organometallics* **20**, 5769 (2001).

[25] S. J. Toal, H. Sohn, L. N. Zakarov, E. S. Kassel, J. A. Golen, A. L. Rheingold, and W. C. Trogler, *Organometallics* **24**, 3081 (2005).

Chapter Eight
Enhancement of Photoluminescence Efficiency of Polysilole by Aggregation-induced Emission

8.1 Introduction

Polysiloles have recently received much attention [1] because of their unusual electronic properties. These unusual optical and electrical properties can be useful in electronic devices, such as electron transporting materials [2], light-emitting diodes (LEDs) [3-5], and chemical sensors [6,7]. Poly(2,3,4,5-tetraphenyl)-siloles (**1**) possess both 2,3,4,5-tetraphenyl-1-silacyclopenta-2,4-diene and Si-Si backbone that their absorptions exhibit at 314 nm. However, the unsaturated five-membered ring of the silole shifts their optical absorption and emission spectra into the visible spectral region at 364 and 520 nm, respectively. The aggregation of highly emissive organics and polymers into a solid state causes an emission-quenching effect, since the aggregation of molecules forms less emissive species such as excimers [8]. Reduction of emission efficiency in the solid state has been a major problem in device applications of light-emitting organic molecules. Many attempts to prevent aggregate formation have been made through chemical, physical, and engineering approaches. In contrast, few results on aggregation-induced emission (AIE) properties have been recently reported [9-12]. This chapter describes an aggregation-induced emission enhancement of polysiloles.

8.2 Experiments

The syntheses of **1**, dichloro(tetraphenyl)silole (**2a**), and dimethyl(tetraphenyl)silole (**2b**) were reported previously [3]. The reduction of 2a with lithium gave molecular weights (M_w) of 5500 (M_w/M_n = 1.1 determined by SEC). Fluorescence emission and excitation spectra were recorded on a Perkin-Elmer Luminescence Spectrometer LS 50B. The solvents were determined to be free of emitting impurities prior to use. The concentration of polysilole aggregates for the fluorescence measurement was 10 ㎍/L. 2a and 2b emit 380 and 425 nm, respectively. However polysilole **1** shows emission near 520 nm with excitation at 340 nm. Nanoaggregates of **1** are prepared by rapid precipitation from water solution by the injection of THF solution containing polysilole. This procedure is different from the previous report [10] and gives better monodisperse for any given water volume fraction. Polysilole aggregate exhibits a nearly identical emission band, however polysilole nanoaggregates are more highly fluorescent than polysiloles at identical concentration.

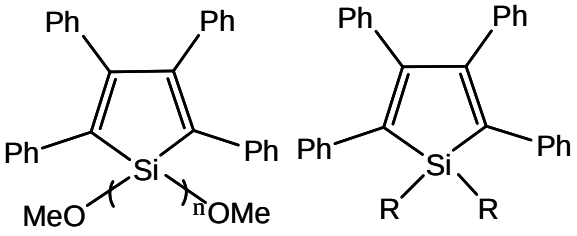

1 2a ; R = Cl
2b ; R = CH_3

8.3 Results and Discussion

Polysilole structure features a Si-Si backbone inside a conjugated ring system of side chains closely packed to yield a helical arrangement with 1 nm of diameter and 10 nm of length as shown in Figure 8.1. Figure 8.1 displays a space filling model structure of polysilole.

A photograph of polysiloles in THF solution (left) and polysilole nanoaggregates (right) under a UV lamp is shown in Figure 8.2, indicating that polysilole nanoaggregates are more highly fluorescent than polysiloles at identical concentration. For polysilole solution in pure THF, the photoluminescence (PL) intensity is very weak and an emission peak near 520 nm was observed. In solutions between 0% and 40% water by volume, the emission intensity of polysilole nanoaggregates does not increased. However, the intensity of the emission band increases by about 17.8 times when the solution is 99% water by volume. As the water fraction is increased, the emission intensity of polysilole nanoaggregates increases dramatically with no shift in the emission wavelength. Polysilole nanoaggregates in water-THF mixtures with 50%-99% water by volume exhibit one emission band at 513 nm when excited at 340 nm as shown in Figure 8.3. The emission band of polysilole nanoaggregates in water-THF mixtures is blue shifted by 7 nm compared to that of polysilole in THF. A minimum volume-fraction of 50% water is required to increase the luminescence, which indicates the onset of aggregation. This critical water concentration is that observed with other silole monomers [10]. The large increase in photoluminescence from polysilole aggregates could be attributed to the restricted rotation of the phenyl rings, which limits the nonradiative decay pathways [13] or inhibits the solvent assisted quenching resulting from aggregation.

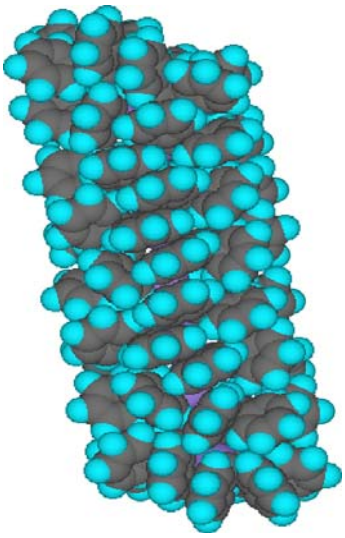

Figure 8.1. Space filling model structure of polysilole

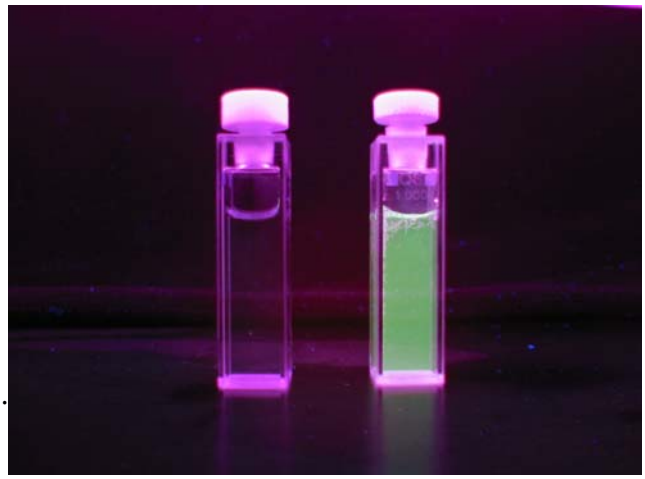

Figure 8.2. Photograph of polysilole in THF (10 mg/L, left) and polysilole nanoaggregates in water-THF mixture (90:10 by volume, 10 mg/L, right) under black light

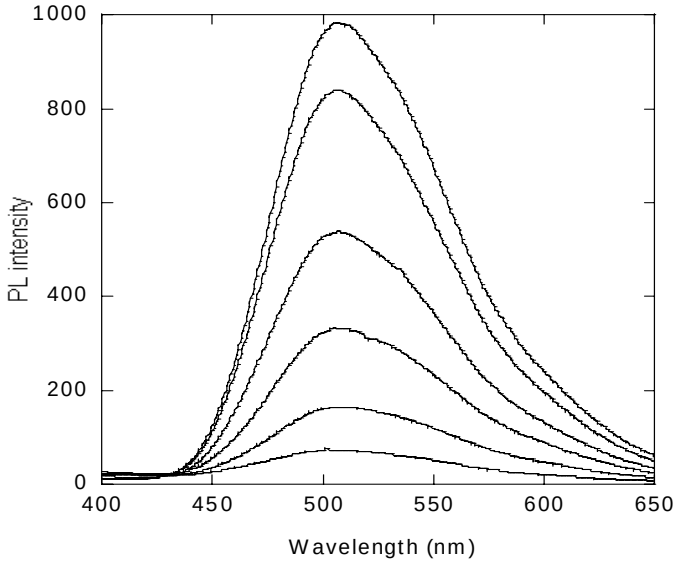

Figure 8.3. Fluorescence spectra of polysilole aggregates in water-THF mixtures (% water from top; 99%, 90%, 80%, 70%, 60%, 50%).

Figure 8.4 shows the plot for the relative PL intensity of polysilole nanoaggregate *vs* % water by volume. When the water fraction increases, the emission intensity increases exponentially, indicating that the luminescence intensity is proportional to the percent of aggregated polysilole. The stability of polysilole nanoaggregates in 90% water solutions has been investigated, and the PL intensity remains unchanged over a month. This indicates that polysilole nanoaggregates show neither further aggregation nor degradation. Figure 8.5 obtained by cold field emission scanning electron micrography (FE-SEM, Hitachi; S-4700) exhibits the

image of polysilole nanoaggregates in different water fractions. Aggregates of **1** consist of particles on the order of 20 nm in diameter in 90% water solution, as determined by dynamic light scattering measurements (Particle Size Analyzer, Microtrac: UPA150). Particle diameter appears to vary with water fraction, but the dispersity of diameter for given any suspension is about ± 3%. Particle diameters are around 700 nm for 50 to 70% water volume fraction and near 400 nm for 80% water, but they decrease dramatically above 80% water. Polysilole nanoaggregates exhibit a minimum in size at 90% water. A possible explanation is that at higher water concentrations the organic molecules aggregate to a higher extent in the hydrophilic environment, but THF absorbing into the aggregate causes them to swell at lower water concentrations. UV-vis spectra were obtained using Hewlett-Packard 8452A diode array spectrometer. UV-vis absorption and fluorescence spectra were measured for the polysilole in THF. Polysilole exhibits three absorption bands, which are assigned to the π-π^* (364 nm) transition in the silole ring and the σ-(σ_2^*+π^*) (314 nm) and σ-σ_1^* (260 nm) transitions in the Si-Si backbones. UV-vis absorption spectra of polysilole nanoaggregates have the same absorption band as the silole (2) in THF, but the π-π^* transition red shifts as the percent water increases. In 90% water solutions, the π-π^* transition of polysilole aggregates occurs at 374 nm.

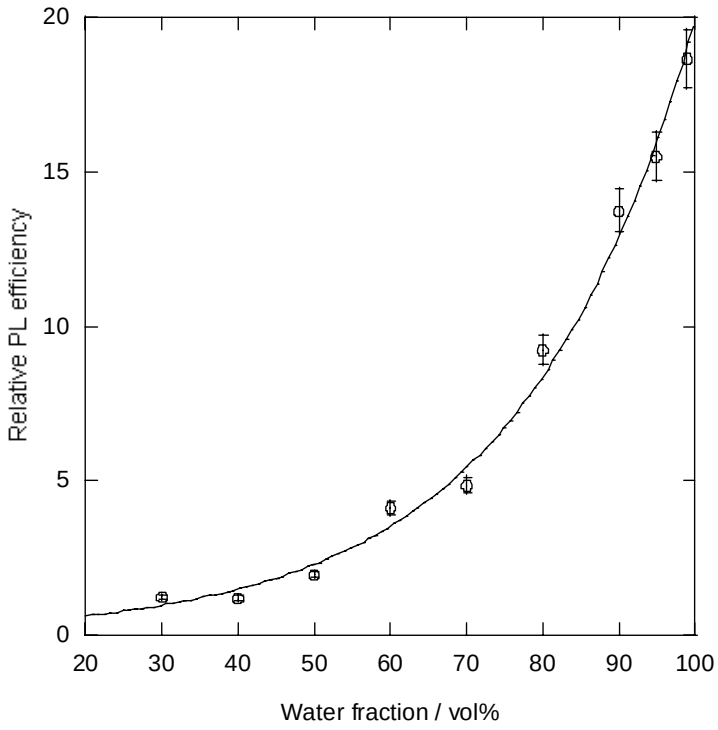

Figure 8.4. Plot of the relative intensity of polysilole aggregates *vs* % water by volume

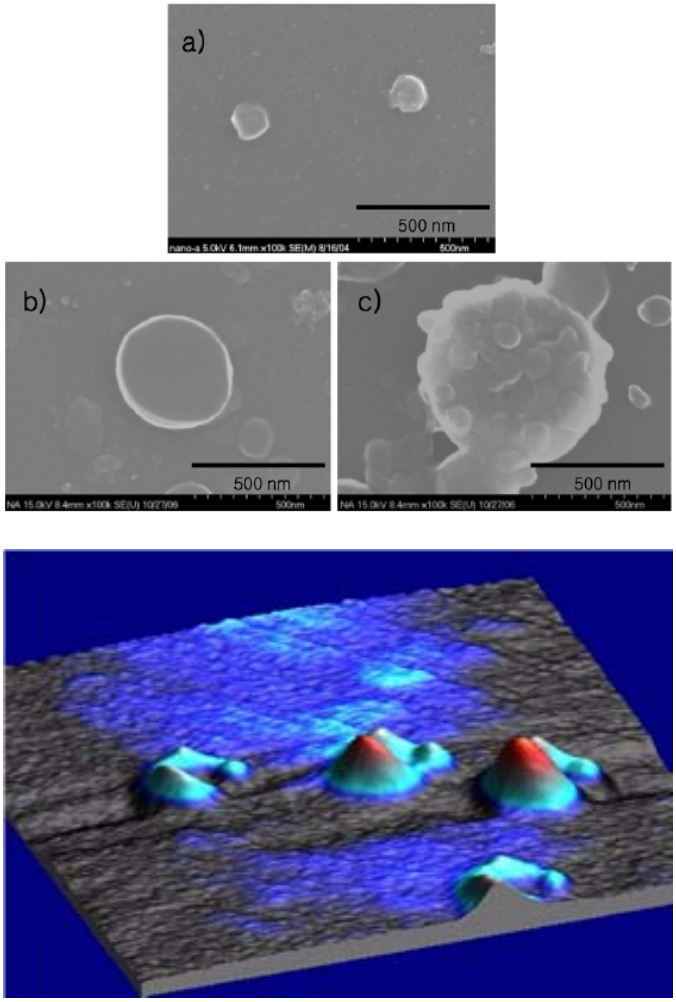

Figure 8.5. FE-SEM images of polysilole nanoparticles from (a) 90%, (b) 80%, and (c) 70% water fraction and AFM image of polysilole nanoparticles (dimension: 2.8×2.8 μm^2)

8.4 Conclusions

Polysilole nanoaggregates exhibit an aggregation-induced emission enhancement with an intensity of 17.8 times to that of normal photoluminescence when the water fraction is increased to 99%. The photoluminescence intensity of polysilole is exponential to the percent of water fraction and particle diameter is dependent on solvent composition.

8.5 References

[1] R. West, H. Sohn, U. Bankwitz, J. Calabrese, Y. Apeloig, and T. Mueller, *J. Am. Chem. Soc.* **117**, 11608 (1995).

[2] K. Tamao, M. Uchida, T. Izumizawa, K. Furukawa, and S. Yamaguchi, *J. Am. Chem. Soc.* **118**, 11974 (1996).

[3] H. Sohn, R. R. Huddleston, D. R. Powell, R. West, K. Oka, and X. Yonghua, *J. Am. Chem. Soc.* **121**, 2935 (1999).

[4] Y. Xu, T. Fujino, H. Naito, T. Dohmaru, K. Oka, H. Sohn, and R. West, *Jpn. J. Appl. Phys.* **38**, 6915 (1999).

[5] S. Yamaguchi, R. Z. Jin, and K. Tamao, *J. Am. Chem. Soc.* **121**, 2937 (1999).

[6] H. Sohn, R. M. Calhoun, M. J. Sailor, and W. C. Trogler, *Angew. Chem. Int. Ed.* **11**, 2104 (2001).

[7] H. Sohn, M. J. Sailor, D. Magde, and W. C. Trogler, *J. Am. Chem. Soc.* **125**, 3821 (2003).

[8] R. Jakubiak, Z. Bao, L. Rothberg, *Synth. Met.* **114**, 61 (2000).

[9] R. Deans, J. Kim, M. R. Machacek, and T. M. Swager, *J. Am. Chem. Soc.* **122**, 8565 (2000).

[10] J. Luo, Z. Xie, J. W. Lam, L. Cheng, H. Chen, C. Qiu, H. S. Kwok, X. Zhan, Y. Liu, D. Zhu, and B. Z. Tang, *Chem. Commun.* **115**, 1740 (2001).

[11] L. C. Palilis, A. J. Maekinen, M. Uchida, Z. H. Kafafi, *Appl. Phys. Lett.* **14**, 2209 (2003)

[12] B.-K. An, S.-K. Kwon, S.-D. Jung, and S. Y. Park, *J. Am. Chem. Soc.* **124**, 14410 (2002).

[13] M. H. Lee, D. Kim, Y. Dong, and B. Z. Tang, *J. Korean Phys. Soc.* **45**, 329 (2004).

Chapter Nine
Enhancement of Photoluminescence Efficiency of Polygermole by Aggregation-induced Emission

9.1 Introduction

Polymetalloles such as siloles and germoles containing silicon and germanium have continuously received much attention because of their unusual electronic properties [1-3]. These unusual optical and electrical properties can be useful in electronic devices, such as electron transporting materials [4], light-emitting diodes (LEDs) [5-7], and chemical sensors [8-9]. Analogous of cyclopentadiene, siloles and germoles are π-electron systems containing Si-Si and Ge-Ge atom as part of a cyclic 5-membered ring. Characteristic features of siloles and germoles include a low reduction potential and a low-lying LUMO due to σ^*-π^* conjugation arising from the interaction between the σ^* orbital of silicon and germanium, and the π^* orbital of the butadiene moiety of the five membered ring [10-11]. In a recent years, a few compounds including silole and polysilole have been found to display unusual aggregation-induced emission (AIE) properties [12-16]. However, studies of germole and polygermole aggregates have not been done yet. When the common molecules become aggregates, their photoluminescence is generally decreased. Thus, many attempts to prevent aggregate formation have been done through chemical, physical, and engineering approaches.

In contrast, polysiloles and polygermoles exhibit weak photoluminescence in

common organic solvents, but if they become aggregates, their efficiency of photoluminescence is surprisingly increased. In the previous chapter, the fluorescence quantum yields of polysilole aggregates were also increased by a few hundreds times, compare to those in organic solvent [13].

In this chapter, an aggregation-induced emission enhancement of polygermoles is described. PL intensity of polygermole aggregates has not been changed over a month. This indicates that polygermole nanoaggregates show neither further aggregation nor degradation.

9.2 Experiments

9.2.1 Generals

All synthetic manipulations were carried out under an atmosphere of dry argon gas using standard vacuum-line Schlenk technique. All solvents were purified and degassed before use according to standard literature methods: diethylether, tetrahydrofuran (THF), methanol were purchased from Aldrich Chemical Co. Inc. and distilled from sodium/benzophenone ketyl. All other reagents (Aldrich) such as diphenylacetylene, Lithium wire, and germanium tertrachloride were purchased and used without any purification. Spectroscopic grade THF from Fisher Scientific was used for the fluorescence measurements.

NMR grade deuteriochloroform was stored over 4 Å molecular sieves. NMR data were collected with 300 MHz spectrometer for ^{1}H NMR. Chemical shifts are reported in parts per million (δ ppm); downfield shifts are reported as positive values from tetramethylsilane (TMS) standard at 0.00 ppm.

UV-vis absorption spectrum and fluorescence emission spectrum were recorded with the use of a Shimadzu UV-2401 spectrophotometer and a Perkin-Elmer luminescence spectrometer LS 50B, respectively. The solvents were determined to be free of emitting impurities prior to use. To avoid changing the concentrations of the emitting compound, the experiments were carried out with solution by preparing the quencher in the same solution of the emitting compound.

The concentration of germole, polygermole, and polygermole aggregates for the fluorescence measurement was 1 mg/1 L = 1 ppm.

Sizes of polygermole aggregates were obtained by particle size analyzer (PSA) and a cold field emission scanning electron microscope (FE-SEM, S-4800, Hitachi).

9.2.2 Syntheses

9.2.2.1. Preparation of 1,1-dichloro-2,3,4,5-tetraphenylgermole 1

To a solution of diphenylacetylene (26.7 g, 150 mmol) in dry diethyl ether (130 mL) was added clean lithium shavings (1.39 g, 200 mmol). The reaction mixture was stirred at room temperature for 2 h in a dry argon atmosphere and frozen with liquid N_2 (-197 ℃). The mixture was then added excess germanium tetrachloride (25.7 mL, 300 mmol). The solution was allowed to warm up slowly to room temperature and stirred for an additional 2 h. After stirring for 2 h, the reaction mixture was standed for overnight. The organic solution layers extracted with cannula and evaporated under reduced pressure. Recrystallization from diethyl ether at -20 ℃ gave a faintly yellow crystals (30 g, 80%). M.p. 197-199 ℃.; ^{1}H NMR (300 MHz, $CDCl_3$): δ = 6.83-6.88 and 7.04-7.21 (m, 20H, Ph); ^{13}C NMR (75.403 MHz, $CDCl_3$ (δ = 77.00)): δ = 149.96, 136.57, 134.66, 132.72, 129.54, 129.50, 128.36, 128.06, 127.68, 127.47.

9.2.2.2. Preparation of Polytetraphenylgermole 2

To a solution of 1,1-dichloro-2,3,4,5-tetraphenylgermole **1** (3 g, 6 mmol) dissolved in dry THF (60 mL) was added 2 equivalent of clean lithium shavings (82.8 mg, 12 mmol). The reaction mixture was refluxed for 3 days in a dry argon atmosphere. The solution was allowed to warm up slowly to room temperature and then evaporated to concentrated solution. The solution was precipitated by pouring the solution into methanol and extacted under reduced pressure and then washed with excess methanol to remove unreacted lithium metals. Polytetraphenylgermole **2** was obtained as pale yellow powders (1.2 g, 30%).; ^{1}H NMR (300 MHz, $CDCl_3$): δ = 6.30-7.40 (m, 20H, Ph), δ = 3.50 (OMe); ^{13}C NMR (75.403 MHz, $CDCl_3$

(δ = 77.00)): δ = 125-131 and 137-147 (m, Ph).

9.2.2.3. Preparation of Polytetraphenylgermole Nanoaggregates 3

Polytetraphenylgermole nanoaggregates of **3** are prepared by rapid precipitation from water solution by the injection of THF solution containing polygermole. This procedure is different from the previous report [12] and gives better mono-disperse for any given water volume fraction.

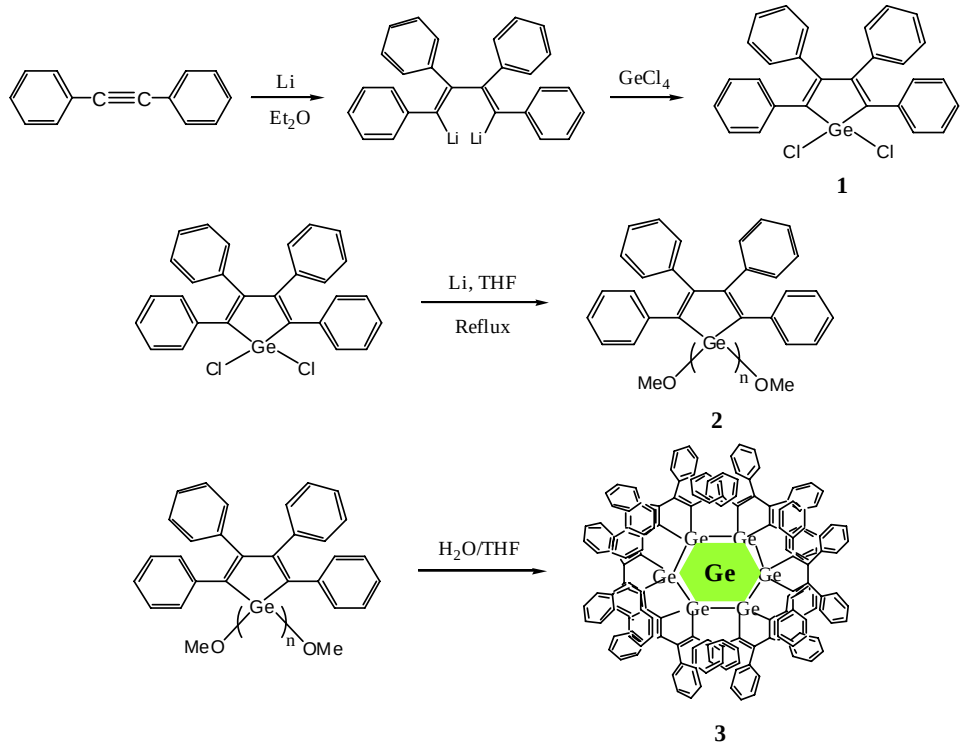

Scheme 9.1. Synthetic routes of compounds **1-3**

9.3 Results and Discussion

For polygermole solution in pure THF, the photoluminescence (PL) intensity was very low and an emission peak near 510 nm was observed. Polygermole aggregates **3** exhibit a nearly identical emission band, however polygermole aggregates are more highly fluorescent than germoles and polygermoles at identical concentration as shown in Figure 9.1.

Aggregates of polygermole are prepared by rapid precipitation from water solution by the injection of THF solution dissolving polygermole. This procedure is different from the previous report [12] and gives better monodisperse for any given water volume fraction. As increasing water fraction, the emission intensity of polygermole aggregates increases dramatically as shown in Figure 9.2. There is no shift in the emission wavelength. In the range of water fraction between 0% and 40%, the emission intensity of polygermole aggregates increases slightly. However, the intensity of emission band increases about 730%, when the solution is 90% water fraction by volume.

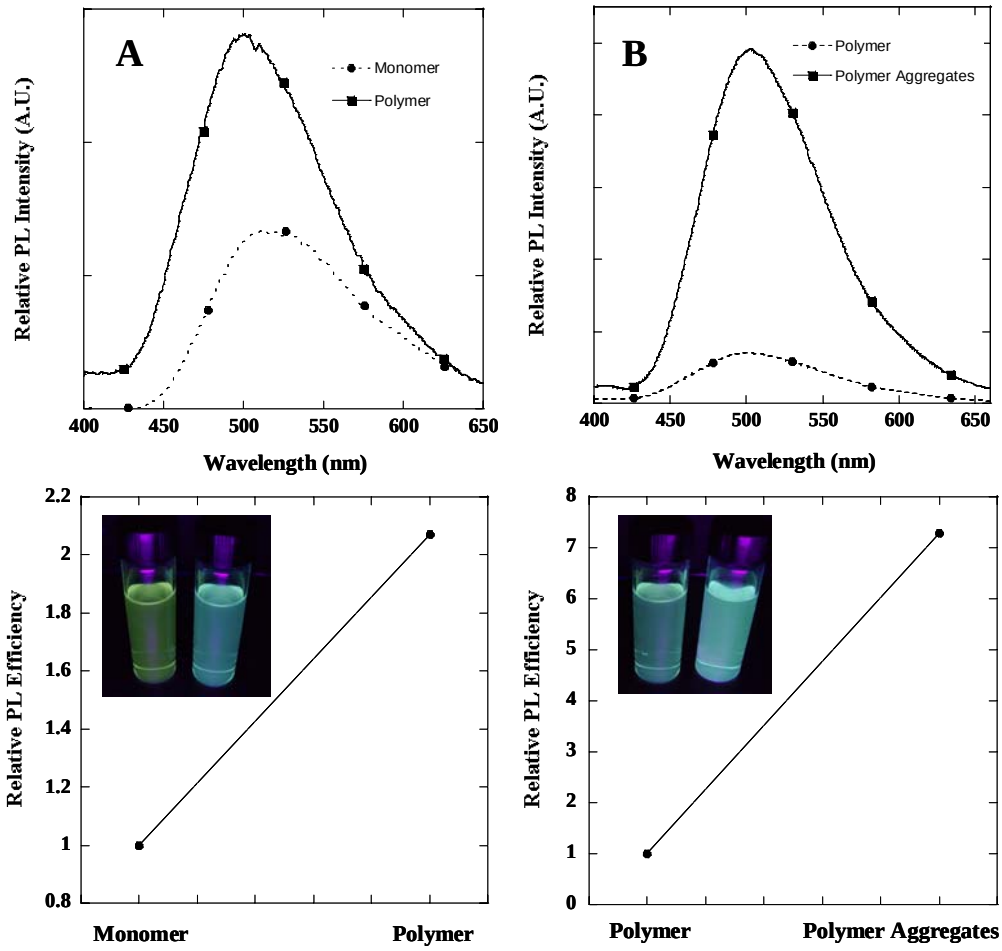

Figure 9.1. Relative PL spectra and plots of the relative intensity of monomer, polymer, and polymer nanoaggregates

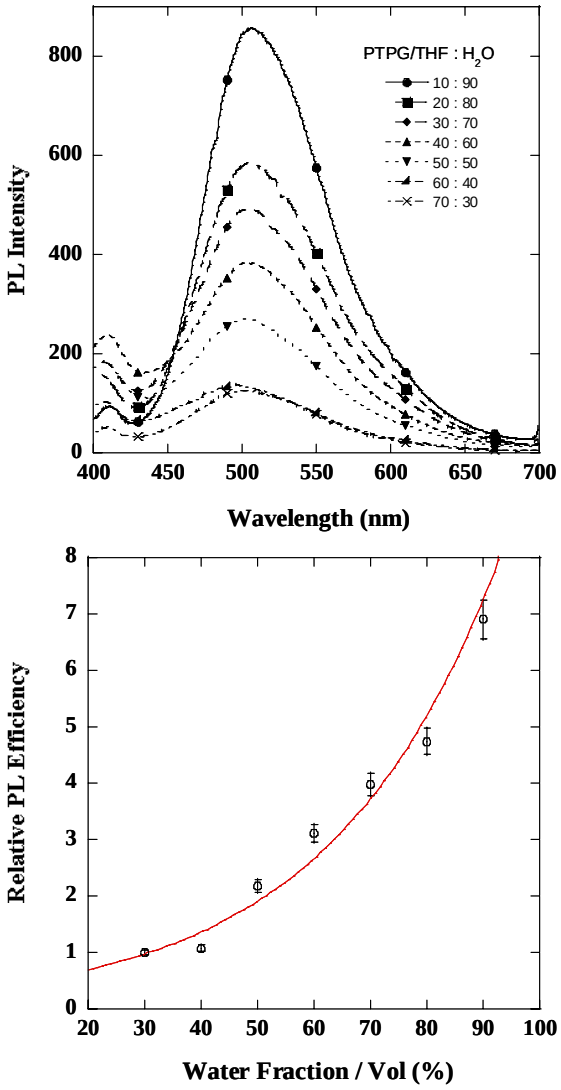

Figure 9.2. PL spectra of polygermole nanoaggregates in water-THF mixtures and plot of the relative intensity of polygermole nanoaggregates *vs* percent water by volume

Stability of polygermole aggregates with 90% water fraction has been investigated. PL intensity of polygermole aggregates has not been changed over a month. This indicates that polygermole aggregates show neither further aggregation nor degradation. Figure 9.3 shows that particle size distributions of polygermole aggregates exhibit between a few nanometer and hundreds nanometers in the water/THF mixtures with 90%, 80%, and 70% by volumes.

FE-SEM images of polygermole aggregates with different water fraction have been obtained and shown in Figure 9.4. Sizes of polygermole aggregates with different water fraction by volume are in the range from 40 to 238 nanometers corresponding to PSA data. FE-SEM images of polygermole aggregates indicate that the higher water fraction is the smaller aggregate particles. This implies that nanoparticles of polygermole aggregate can be readily tuned by controlling the water fraction.

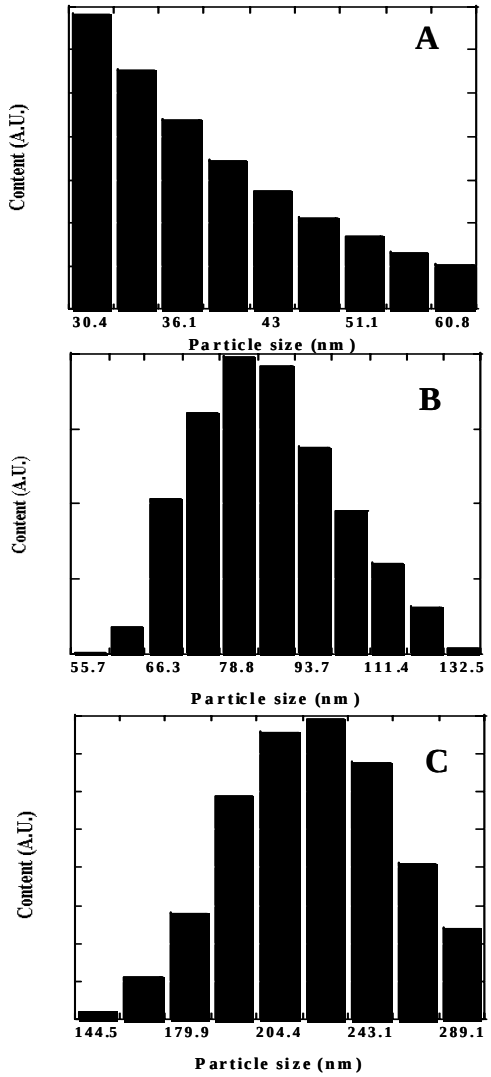

Figure 9.3. Particle size distributions of polygermole nanoaggregates in the water/THF mixtures with (A) 90%, (B) 80%, and (C) 70%

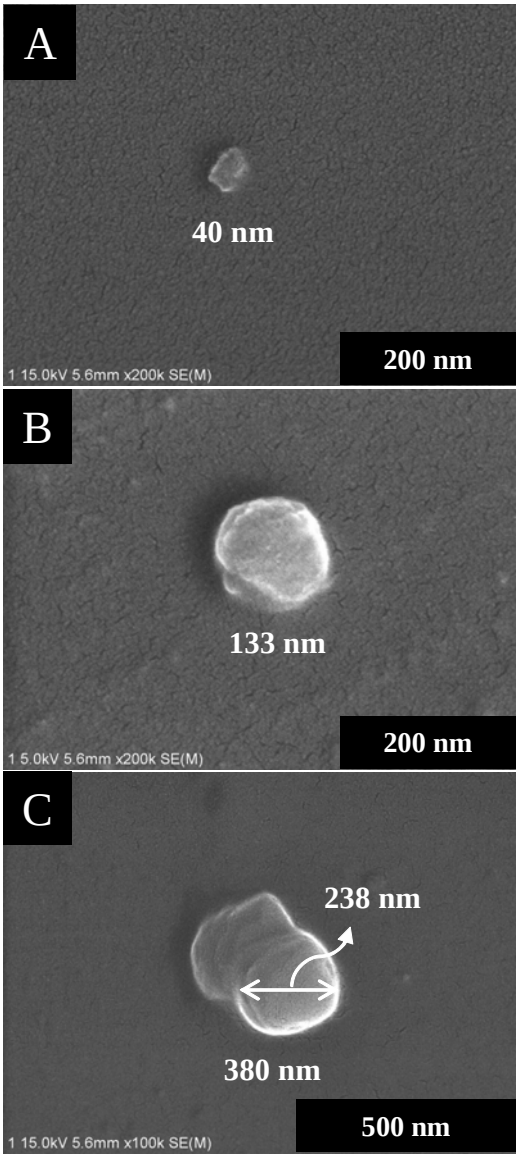

Figure 9.4. FE-SEM images of polygermole nanoaggregates in the water/THF mixtures with (A) 90%, (B) 80%, and (C) 70%

9.4 Conclusions

Polygermole aggregates have been developed by using an aggregation-induced emission property of polygermoles. Polygermole aggregates exhibit PL intensity of emission band increases about 730% to that of normal photoluminescence when the water fraction is increased to 90% water fraction by volume. Relative PL efficiency of polygermole aggregates is exponentially increased to the percent of water fraction and particle diameter is dependent on solvent composition. PL intensity of polygermole aggregates has not been changed over a month. This indicates that polygermole aggregates show neither further aggregation nor degradation at the experimental condition.

9.5 References

[1] R. West, H. Sohn, U. Bankwitz, J. Calabrese, Y. Apeloig, and T. Mueller, *J. Am. Chem. Soc.* **117**, (1995) 11608.

[2] S. Yamaguchi and K. Tamao, *J. Chem. Soc., Dalton Trans.* 3693 (1998).

[3] S. Yamaguchi, T. Endo, M. Uchida, T. Izumizawa, K. Furukawa, and K. Tamao, *Chem. Eur. J.* **6**, 1683 (2000).

[4] K. Tamao, M. Uchida, T. Izumizawa, K. Furukawa, and S. Yamaguchi, *J. Am. Chem. Soc.* **118**, 11974 (1996).

[5] H. Sohn, R. R. Huddleston, D. R. Powell, and R. West, *J. Am. Chem. Soc.* **121**, 2935 (1999).

[6] Y. Xu, T. Fujino, H. Naito, T. Dohmaru, K. Oka, H. Sohn, and R. West, *Jpn. J. Appl. Phys.* **38**, 6915 (1999).

[7] S. Yamaguchi, R. Z. Jin, and K. Tamao, *J. Am. Chem. Soc.* **121**, 2937 (1999).

[8] H. Sohn, R. M. Calhoun, M. J. Sailor, and W. C. Trogler, *Angew. Chem. Int.*

Ed. **40**, 2104 (2001).

[9] H. Sohn, M. J. Sailor, D. Magde, and W. C. Trogler, *J*. *Am*. *Chem*. *Soc*. **125**, 3821 (2003) .

[10] Y. Yamaguchi, *Synth*. *Met*. **82**, 149 (1996).

[11] S. Yamaguchi and K. Tamao, *Bull*. *Chem*. *Soc*. *Jpn*. **69**, 2327 (1996).

[12] J. Luo, Z. Xie, J. W. Y. Lam, L. Cheng, H. Chen, C. Qiu, H. S. Kwok, X. Zhan, Y. Liu, D. Zhu, and B. Z. Tang, *Chem*. *Commun*. 1740 (2001).

[13] S. Jang, S. G. Kim, D. Jung, H. Kwon, J. Song, S. Cho, Y. C. Ko, and H. Sohn, *Bull*. *Korean Chem*. *Soc*. **27**, 1965 (2006).

[14] R. Deans, J. Kim, M. R. Machacek, and T. M. Swager, *J*. *Am*. *Chem*. *Soc*. **122**, 8565 (2000).

[15] L. C. Palilis, A. J. Maekinen, M. Uchida, and Z. H. Kafafi, *Appl*. *Phys*. *Lett*. **14**, 2209 (2003).

[16] B.-K. An, S.-K. Kwon, S.-D. Jung, and S. Y. Park, *J*. *Am*. *Chem*. *Soc*. **124**, 14410 (2002).

Chapter Ten
Fluorescent Chemosensors Based on Aminosilole for the Detection of Inorganic Acids

10.1 Introduction

Chemical sensors, which are new approaches to the rapid detection of ultra-trace analytes from inorganic acids, have attracted a great deal of attention in recent years for their toxicity. Detection of inorganic acid such as hydrochloric acid, hydrofluoric acid, nitric acid, and sulfuric acid is important, since they are highly toxic (for example, the Occupational Safety and Health Administration, OSHA, limit for human exposure to HF in the gas phase is 3 ppm) and used in large quantities in industrial environments, in particular in the semiconductor and petroleum refining industries [1].

Functionalized siloles have been a topic of interest because of their unique optical and electroluminescent properties [2-3]. These unusual optical and electrical properties can be useful in the applications of electronic devices, such as electron transporting materials, light-emitting diodes (LEDs), and chemical sensors [4-7]. Silole, silacyclopentadienes, are a group of unsaturated five-membered ring that possess unique low-lying LUMO level associated with σ^*-π^* conjugation arising from the interaction between the σ^* orbital of two exocyclic σ-bond on the silicon atom and the π^* orbital of the butadiene moiety [8-9]. Polymetalloles and their nanoaggregates can be also great candidates for the detection of explosives

such as TNT, DNT, NB and picric acid and carcinogenic heavy metals [10]. However, these polymers and aggregates require many steps to synthesize and are less sensitive to inorganic acids.

This chapter describes the development of 1-amino-1-methyl-2,3,4,5-tetraphenyl silole **2** and 1-methyl-1-(3-amino)propyl-2,3,4,5-tetraphenylsilole **4** with novel fluorescence properties which can be widely used as a new chemosensor for the detection of inorganic acids. The detection of inorganic acids is achieved from the measurement of quenching and enhancing photoluminescence of aminosiloles by adding the analytes.

TLC-based detection method covered with aminosilole is also developed. This TLC-based detection method can be employed a thin film of photoluminescent compounds, which are stable in air, water, and common organic solvents. Detection efficiency for the detection of inorganic acids can be enhanced by using TLC-based method about 100 times compare to litmus paper.

10.2 Experiments

10.2.1 Generals

All synthetic manipulations were carried out under an atmosphere of dry argon gas using standard vacuum-line Schlenk technique. All solvents were purified and degassed before use according to standard literature methods: diethylether, hexanes, tetrahydrofuran (THF), and toluene were purchased from Aldrich Chemical Co. Inc. and distilled from sodium/benzophenone ketyl. Spectroscopic grade THF from Fisher Scientific was used for the fluorescence measurements. NMR grade deuteriochloroform was stored over 4 Å molecular sieves. All other reagents (Aldrich) such as HCl, HNO_3, and H_2SO_4 were purchased and used without any purification. NMR data were collected with 300 MHz spectrometer for ^1H NMR. Chemical shifts are reported in parts per million (δ ppm); downfield shifts are reported as positive values from tetramethylsilane (TMS) standard at 0.00 ppm. UV-vis absorption spectrum and fluorescence emission spectrum were recorded with the use of a Shimadzu UV-2401 spectrophotometer and a Perkin-Elmer luminescence spectrometer LS 50B, respectively. The solvents were determined to be free of emitting impurities prior to use. To avoid changing the concentrations of the emitting compound, the experiments were carried out with solution by preparing the quencher in the same solution of the emitting compound. The concentration of aminosiloles for the fluorescence quenching measurements was 10 mg/1 L, which is about 2.4×10^{-6} M. Fluorecence spetra were immediately taken after injection of analyte.

10.2.2 Syntheses

10.2.2.1. Preparation of 1-chloro-1-methyl-2,3,4,5-tetraphenylsilole 1

To a solution of diphenylacetylene (8.9 g, 50 mmol) in dry ether (60 mL) was added clean lithium shavings (695 mg, 100 mmol). The reaction mixture was stirred at room temperature for 2 h in a dry argon atmosphere and frozen with liquid N_2 (-197 ^oC). The mixture was then added excess trichloromethylsilane (19 g, 127 mmol). The solution was allowed to warm up slowly to room temperature and stirred for an additional 2 h. After stirring for 2 h, the reaction mixture was standed for overnight. The organic solvent layers separated with cannula and removed by vacuum pump. Recrystallization from ether gave a faintly greenish-yellow powder.

^1H NMR (300 MHz, $CDCl_3$): δ = 6.7-7.2 (m, 20H, Ph), δ = 0.853 (s, 3H, Me).

10.2.2.2. Preparation of 1-amino-1-methyl-2,3,4,5-tetraphenylsilole 2

1-amino-1-methyl-2,3,4,5-tetraphenylsilole **2** was obtained from the reaction of 1-chloro-1-methyl-2,3,4,5-tetraphenylsilole **1** with excess ammonia dissolved in 0.5 M solution in 1,4-dioxane. The reaction mixture was filtered and filtrate was washed with ether. The organic layer was extracted with ether and dried over magnesium sulfate. The solvent was removed by vacuum pump. Recrystallization from ether gave a yellow powder.

^1H NMR (300 MHz, $CDCl_3$): δ = 6.74-7.19 (m, 20H, Ph), δ = 2.14 (s, 2H, amine) and δ = 0.61 (s, 3H, Me).

10.2.2.3. Preparation of 1-methyl-1-hydro-2,3,4,5-tetraphenylsilole 3

1-methyl-1-hydro-2,3,4,5-tetraphenylsilole **3** was obtained from the reduction of 1-chloro-1-methyl-2,3,4,5-tetraphenylsilole with 2 equivalent of lithium aluminum hydride ($LiAlH_4$) under dry ice bath (-78 ^oC). The reaction mixture was filtered and filtrate was washed with ether. The organic layer was extracted with ether and dried over magnesium sulfate. The solvent was removed by vacuum pump. Recrystallization from ether gave a greenish-yellow powder.

^1H NMR (300 MHz, $CDCl_3$): δ = 6.7-7.1 (m, 20H, Ph), δ = 4.9 (s, 1H,) and δ = 0.56 (s, 3H, Me).

10.2.2.4. Preparation of 1-methyl-1-(3-amino)propyl-2,3,4,5-tetraphenylsilole 4

Methylhydrosilole **3** (1.0 g, 2.5 mmol) dissolved in 20 mL of freshly distilled toluene was added 2 equivalent of allylamine (0.36 mL, 5.0 mmol), $H_2PtCl_6 \cdot 5H_2O$ (2.5 mg, 5 μmol) under dry argon atmosphere and refluxed for 20 h. The solution was cooled and filtered. The solvent was evaporated to dryness. The product was dissolved in ether and precipitated with hexanes and filtered. The precipitate was collected as a yellow powder.

^1H NMR (300 MHz, $CDCl_3$): δ = 6.67-7.14 (m, 20H, Ph), δ = 2.62 (t, 2H), δ = 1.50 (m, 2H), δ = 1.03 (m, 2H) and δ = 0.48 (s, 3H, Me).

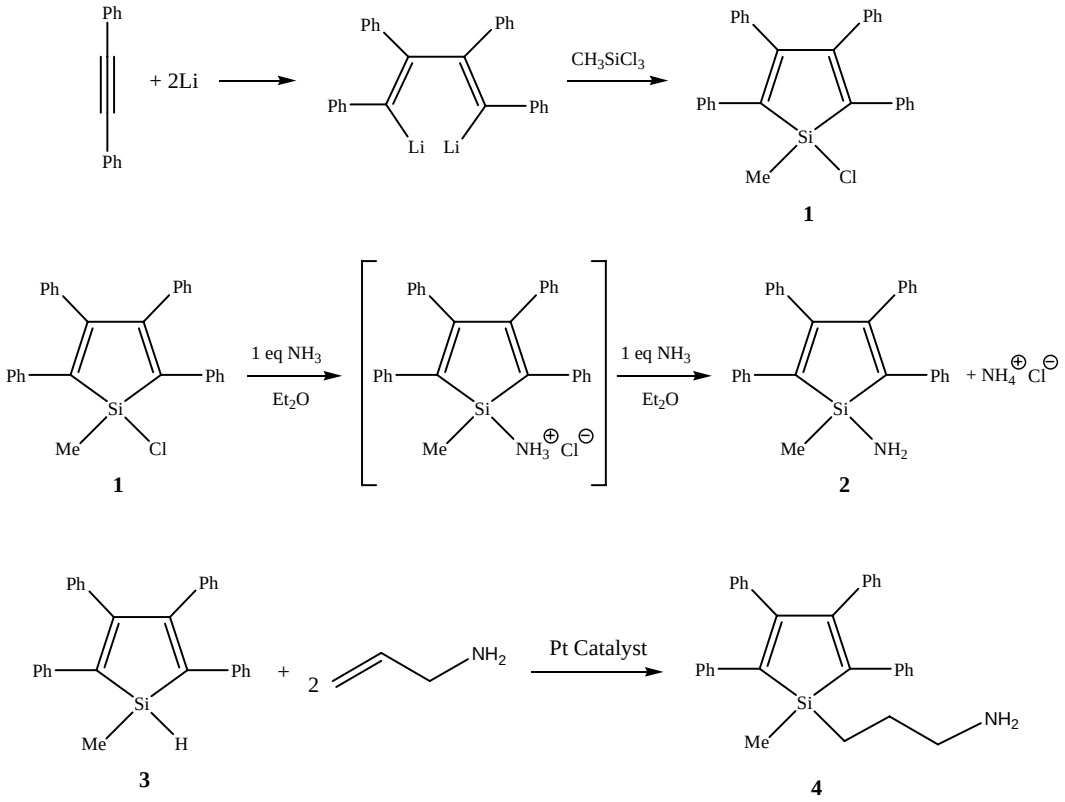

Scheme 10.1. Synthetic routes of compounds **1-4**

10.3 Results and Discussion

The UV-vis absorption and fluorescence spectra are measured for the 1-amino-1-methyl-2,3,4,5-tetraphenylsilole **2** and 1-methyl-1-(3-amino)propyl-2,3,4,5-tetraphenylsilole **4** in THF, respectively as shown in Figure. 10.1. 1-amino-1-methyl-2,3,4,5-tetraphenylsilole **2** exhibits one emission band (λ_{max}, 495 nm) when excited at 375 nm and 1-methyl-1-(3-amino)propyl-2,3,4,5-tetraphenylsilole **4** exhibits one emission band (λ_{max}, 492 nm) when excited at 360 nm, respectively.

The detection method for hydrochloric acid involves measurement of the quenching of photoluminescence of the 1-amino-1-methyl-2,3,4,5-tetraphenylsilole **2** by adding analyte (using a Perkin-Elmer LS 50B fluorescence spectrometer, 360 nm excitation wavelength) and dictated quenching mechanism. Figure 10.2A shows that photoluminescence of 1-amino-1-methyl-2,3,4,5-tetraphenylsilole **2** is quenched by adding 10 ppm of HCl. In contrast, 1-methyl-1-(3-amino)propyl-2,3,4,5-tetraphenyl-silole **4** could be also used for the detection of inorganic acids as a chemosensor by measurement of the enhancing of photoluminescence as shown in Figure. 10.3A.

The Stern-Volmer equation is commonly used to quantify the differences in quenching efficiency for various analytes [11].

$$(I_0/I)\text{-}1 = K_{sv}[A]$$

In this equation, I_0 is the initial fluorescence intensity without analyte, I is the fluorescence intensity with added analyte of concentration [A], and K_{sv} is the Stern-Volmer constant. Figure 10.2B and 10.3B show that Stern-Volmer plots of 1-amino-1-methyl-2,3,4,5-tetraphenylsilole **2** and 1-methyl-1-(3-amino)propyl-2,3,4,5-tetraphenylsilole **4** for the detection of HCl are obtained. A linear Stern-Volmer

relationship may be usually observed if either static or dynamic quenching process is dominant. However, in this cases of 1-amino-1-methyl-2,3,4,5-tetraphenylsilole **2** and 1-methyl-1-(3-amino)propyl-2,3,4,5-tetraphenylsilole **4**, the two processes might be competitive, which results in a nonlinear Stern-Volmer relationship.

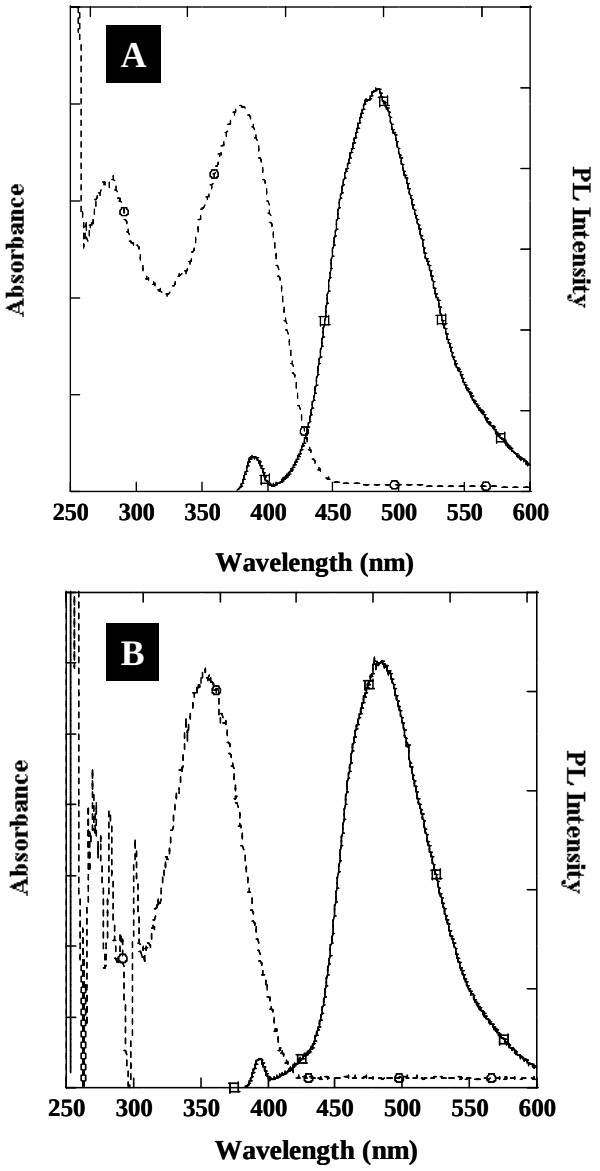

Figure 10.1. UV-Vis absorption and fluorescence spectra. A; 1-amino-1-methyl -2,3,4,5-tetraphenylsilole **2**, B; 1-methyl-1-(3-amino)propyl-2,3,4,5- tetraphenylsilole **4**

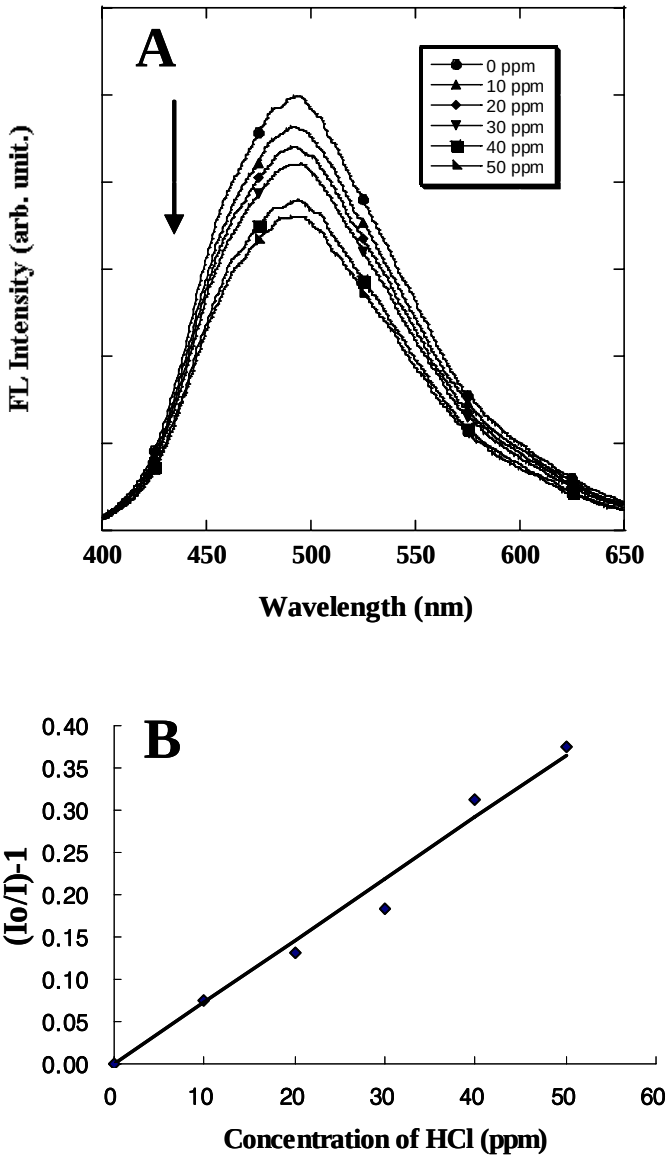

Figure 10.2. FL quenching spectra (A) and Stern-Volmer plot (B) of **2**

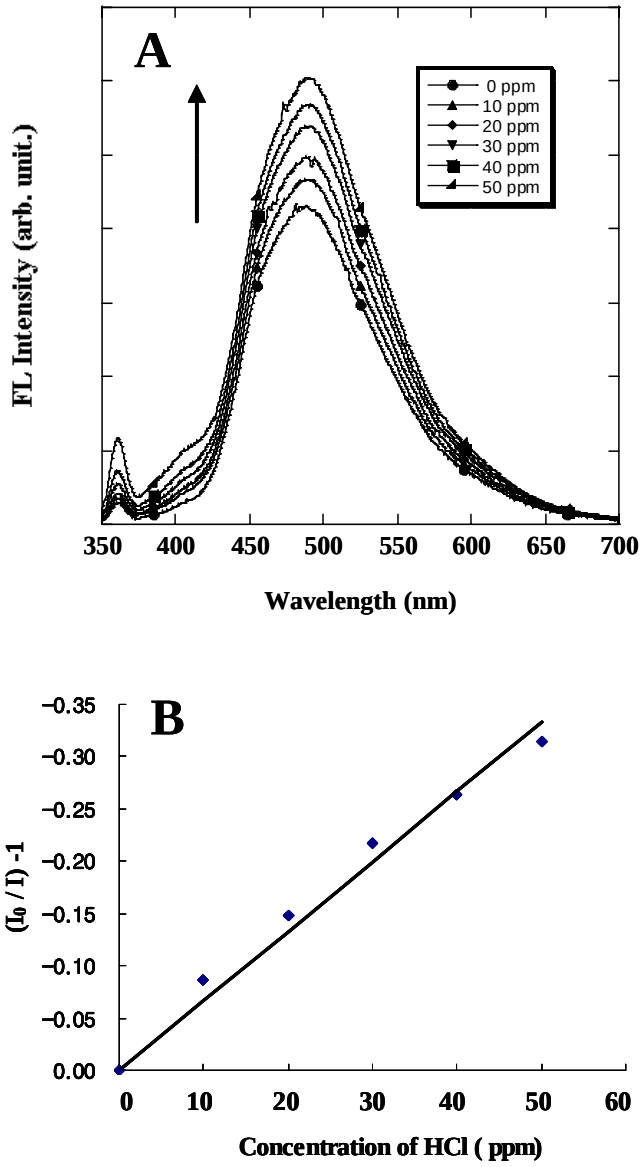

Figure 10.3. FL enhancing spectra (A) and Stern-Volmer plot (B) of **4**

Nitric acid and sulfuric acid are also detected by measuring the enhancing photoluminescence based on 1-methyl-1-(3-amino)propyl-2,3,4,5-tetraphenylsilole **4**. Figure 10.4 shows enhancing photoluminescence spectra of 1-methyl-1-(3-amino) propyl-2,3,4,5-tetraphenylsilole **4** with the different concentration of inorganic acids.

1-amino-1-methyl-2,3,4,5-tetraphenylsilole **2** has a different lifetime when inorganic acid is presence or absence as shown in Figure 10.5.

Thin-layer chromatography (TLC) is widely used in synthetic chemistry as a handy tool for monitoring propagations of chemical reactions. Combinations of TLC with modern spectrometric techniques have led to the development of convenient analysis system for product identifications, which include TLC-MS, TLC-FTIR, TLC-Raman, and TLC-Fluorescence [12-13]. TLC-based method was recently developed for measurement of the solid-state luminescence spectra of the siloles [14]. However, this method has not been used as chemosensor for the detection of inorganic acids.

In this chapter, a simple and reliable aminosilole chemosensor using TLC-based method has been developed. Figure 10.6 demonstrates that HCl vapors can be detected with aminosilole chemosensor using TLC-based method. When a 1 ppm of HCl vapors are exposed to aminosilole for 5 s, photoluminescence of aminosilole is perfectly quenched due to the formation of inorganic salt from the reaction between aminosilole and HCl. Detection limit for the detection of HCl was surprisingly obtained about 40 ppt = 80 femtogram of HCl as shown in Figure. 10.7. This result indicates that aminosilole chemosensor shows better detection efficiency than litmus paper (1 ppb).

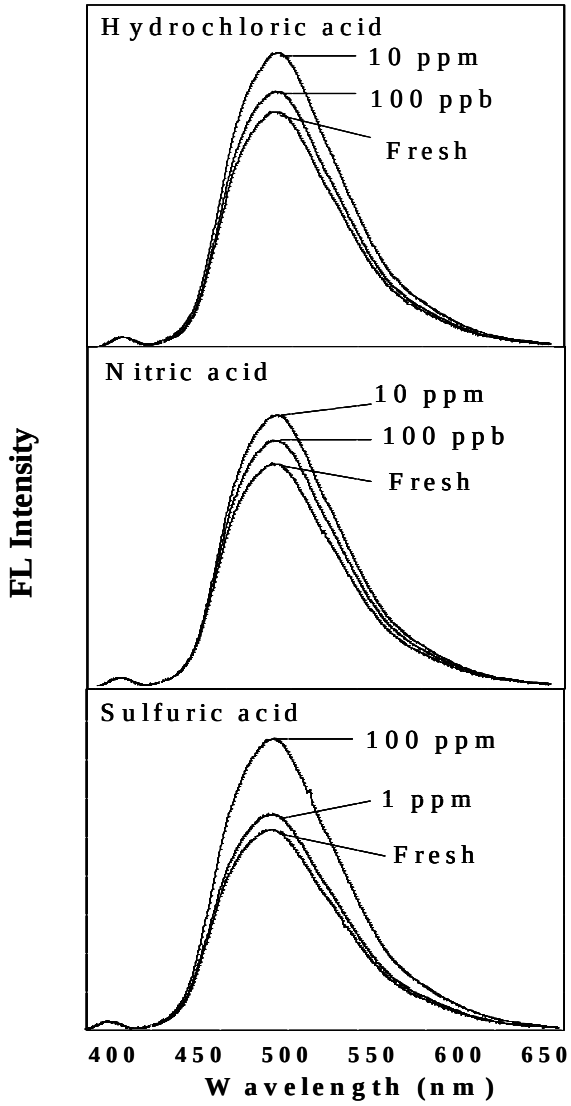

Figure 10.4. Enhancing photoluminescence spectra of **4** with different concentration of inorganic acids

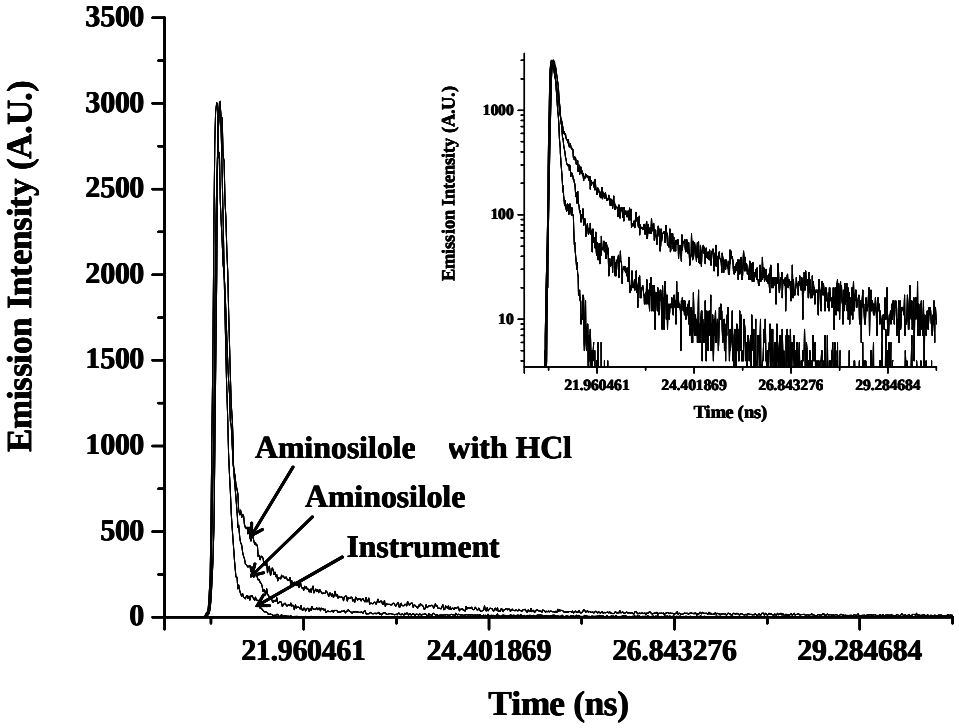

Figure 10.5. Lifetime of **2** and photoluminescence quenched **2** with HCl

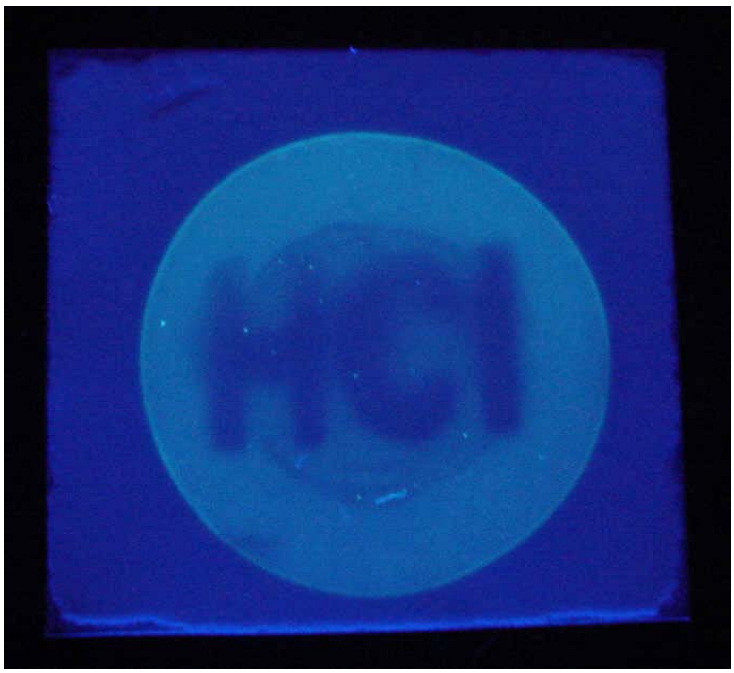

Figure 10.6. Photograph of **2** after exposing 1 ppm of HCl vapor for 5 s under 365 nm UV-lamp

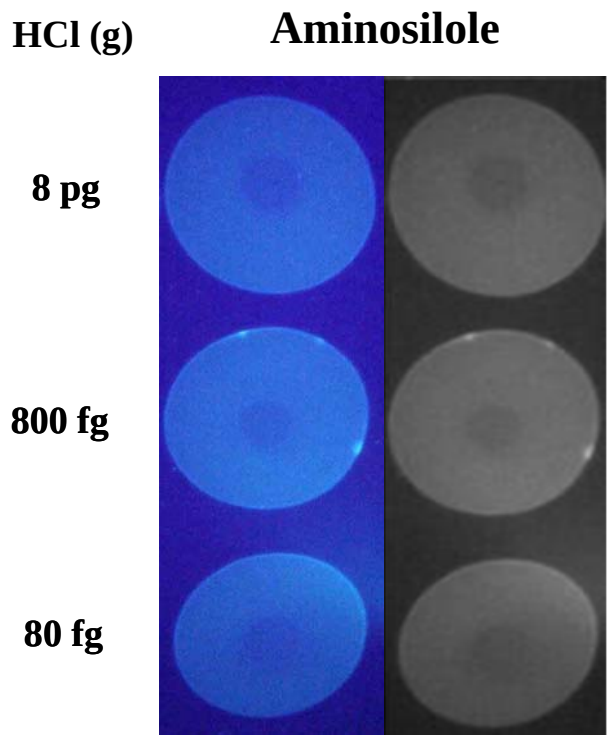

Figure 10.7. Visible traces of photoluminescene quenching of **2** for investigation of the detection limit

10.4 Conclusions

A new chemosensors for the detection of inorganic acids based on photoluminescent 1-amino-1-methyl-2,3,4,5-tetraphenylsilole, ($C_4Ph_4SiMeNH_2$, **2**) and 1-methyl-1-(3-amino)propyl-2,3,4,5-tetraphenylsilole, ($C_4Ph_4SiMeC_3H_6NH_2$, **4**) have been developed. The detection of inorganic acids is achieved from the measuring of quenching and enhancing photoluminescence of aminosiloles by adding the analytes. Photoluminescence changes of aminosiloles were immediately observed. Linear or nonlinear relationship of the Stern-Volmer plots for detection of hydrochloric aicd (HCl) was obtained. The detection mechanism for quenching of photoluminescent aminosilole involve that the reaction between aminosilole and inorganic acids is allow to be inorganic salt, which is not photoluminescence compound. The aminosiloles are highly sensitive and selective to detect the inorganic acids without any other interference. TLC-based detection method with aminosilole is also developed. Our dectection limit for sensing inorganic acid (hydrochloric acid, 40 ppt = 80 femtogram) was obtained using TLC-based technique.

10.5 References

[1] S. E. Letant and M. J. Sailor, *Adv. Mater.* **12**, 355 (2000)

.

[2] S. Yamaguchi and K. Tamao, *J. Chem. Soc., Dalton Trans.* 3693 (1998).

[3] S. Yamaguchi, T. Endo, M. Uchida, T. Izumizawa, K. Furukawa, and K. Tamao, *Chem. Eur. J*, **6**, 1683 (2000).

[4] K. Tamao, M. Uchida, T. Izumizawa, K. Furukawa, and S. Yamaguchi, *J. Am. Chem. Soc.* **118**, 11974 (1996).

[5] H. Sohn, R. R. Huddleston, D. R. Powell, and R. West, *J. Am. Chem. Soc.* **121**, 2935 (1999).

[6] Y. Xu, T. Fujino, H. Naito, T. Dohmaru, K. Oka, H. Sohn, and R. West, *Jpn. J. Appl. Phys.* **38**, 6915 (1999).

[7] H. Sohn, R. M. Calhoun, M. J. Sailor, and W. C. Trogler, *Angew. Chem. Int. Ed.* **40**, 2104 (2001).

[8] S. Yamaguchi, *Synth. Met.* **82**, 149 (1996).

[9] S. Yamaguchi and K. Tamao, *Bull. Chem. Soc. Jp*n. **69**, 2327 (1996).

[10] H. Sohn, M. J. Sailor, D. Magde, and W. C. Trogler, *J. Am. Chem. Soc.* **125**, 3821 (2003).

[11] N. J. Turro, Modern Molecular Photochemistry; University Science Books: Sausalito, California, 1991.

[12] J. Sherma, *Rev. Anal. Chem*. **14**, 75 (1995).

[13] G. W. Somsen, W. Morden, and I. D. Wilson, *J. Chromatogr. A*, **703**, 613 (1995).

[14] J. Chen, C. C. W. Law, J. W. Y. Lam, Y. Dong, S. M. F. Lo, I. D. Williams, D. Zhu, and B. Z. Tang, *Chem. Mater*. **15**, 1535 (2003).

Chapter Eleven
Detection of Explosives Based on Highly Fluorescent Polymetalloles/PMPS composite Nanoaggregates Using AIE and Energy Migration

11.1 Introduction

Chemical sensors, which are new approaches to the rapid detection of ultra-trace anaytes from explosives, have attracted a great deal of attention in recent years, because explosives are extremely important chemical species to detect in mine fields, military bases, remediation sites, and urban transportation areas [1]. It is also important in forensic investigations such as post-blast residue determinations. Metal detectors, which are portable instrument for field explosive detection, cannot locate the plastic casing of modern land mines. Trained dogs are both expensive and difficult to maintain. Other detection methods for explosives use gas chromatography coupled with a mass spectrometer [2], surface-enhanced Raman [3], nuclear quadrupole resonance [4], energy-dispersive X-ray diffraction [5], neutron activation analysis, and electron capture detection [6].

Most detection methods for explosives are only applicable to air samples due to interference problems encountered in complex aqueous media. Sensing TNT and picric acid in ground water or seawater is important for the detection of buried unexploded ordnance and for locating underwater mines. There are also environmental applications for characterizing soil and ground water contaminated

with toxic TNT at military bases and munitions production and distribution facilities. Yang and Swager have shown that highly π-conjugated, porous organic polymers can be used to detect vapors of electron deficient chemicals [7-8]. However, these polymers require many steps to synthesize and are less sensitive to explosives. We also invented an inexpensive and highly efficient inorganic polymer sensor that can detect nitroaromatic compounds, such as picric acid, nitrobenzene, 2,4-dinitrotoluene (DNT), and 2,4,6-trinitrotoluene (TNT) in air or seawater as shown in Figure 11.1 [9-10].

The sensor employs a thin film of photoluminescent metallole copolymers, which are stable in air, water, acids, common organic solvents, and even seawater containing bioorganisms. An important aspect of the inorganic polymer sensors is their insensitivity to common environmental interferents. These conjugated polymers are organometallic semiconductors resulting from the π-molecular orbitals delocalized along the polymer chain. Both photoluminescence and electroluminescence originate from the radiative recombination of exciton states, in the former case formed by photoexcitation, and in the latter by combination of oppositely charged polarons generated by injection of electrons and holes [11]. These unusual optical and electrical properties can be useful in electronic devices, such as diodes, transistors [12-14], light-emitting diodes (LEDs) [13], and large-area light-emitting displays [15]. These unique optoelectronical properties can be used for excellent candidates for luminescent chemical sensors.

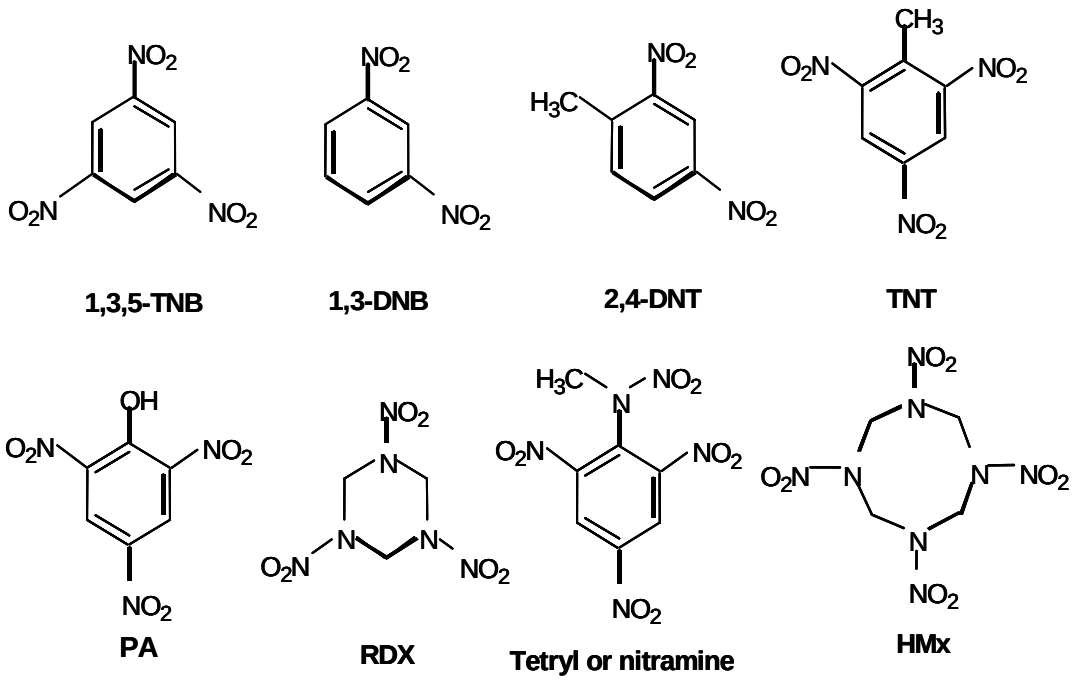

Figure 11.1. Structures of common nitroaromatic compounds as explosives

11.2 Experiments

All synthetic manipulations were carried out under an atmosphere of dry argon gas using standard vacuum-line Schlenk technique. All solvents were purified and degassed before use according to standard literature methods: diethylether, hexanes, tetrahydrofuran (THF), and toluene were purchased from Aldrich Chemical Co. Inc. and distilled from sodium/benzophenone ketyl. Spectroscopic grade THF from Fisher Scientific was used for the fluorescence measurements. NMR grade deuteriochloroform was stored over 4 Å molecular sieves. All other reagents (Aldrich) were purchased and used without any purification.

Polytetraphenylsilole (PTPS) has been synthesized by the procedures described in the previous chapter 7.5.2 (Scheme 7.3). The polymeric aggregate of silole has been synthesized by the procedures described in the previous chapter 8 using 90% water-THF mixtures. TNT was synthesized from the DNT purchased as analytical grade from Aldrich and purified by recrystallization from methanol three times before use [10]. Silole-germolealternating copolymer, in which every other silicon or germanium atom in the polymer chain is also part of a silole or germole ring, was synthesized from the coupling of dichloro(tetraphenylgermole [16] and dilithio(tetraphenyl)silole [17]. dilithio(tetraphenyl) silole is obtained from the dichlorotetraphenylsilole by reduction with lithium as shown in scheme 11.1. The The molecular weight of silole-germole copolymer, M_w = 5.5 × 10^3 Dalton, M_n = 5.0 × 10^3 Dalton, M_w/M_n = 1.10 determined by SEC (size exclusion chromatography) with polystyrene standards, is similar to that of polysilole or polygermoles. For energy migration to polysilole, poly(phenylmethyl)silane (PMPS) as an electron donor was prepared as reported previously [18].

NMR data were collected with 300 MHz spectrometer for ^{1}H NMR. Chemical

shifts are reported in parts per million (δ ppm); downfield shifts are reported as positive values from tetramethylsilane (TMS) standard at 0.00 ppm. UV-vis absorption spectrum and fluorescence emission spectrum were recorded with the use of a Shimadzu UV-2401 spectrophotometer and a Perkin-Elmer luminescence spectrometer LS 50B, respectively. The solvents were determined to be free of emitting impurities prior to use. To avoid changing the concentrations of the emitting compound, the experiments were carried out with solution by preparing the quencher in the same solution of the emitting compound.

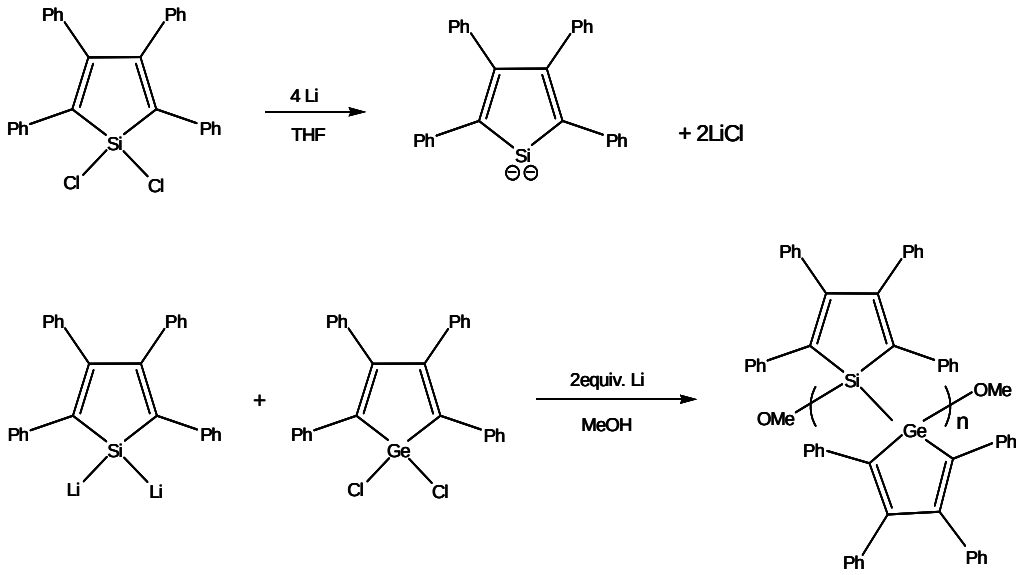

Scheme 11.1. Synthetic routes of silole-germole copolymer

11.3 Results and Discussion

11.3.1 Energy Migration from PMPS to PTPS

The effect of the doping of poly(methylphenylsilane) (PMPS), a good hole transport material, into PTPS has been studied. Polysilanes are well known as thermally stable polymers and they exhibit efficient emission in the UV region, high hole mobility, and high nonlinear optical susceptibility. These novel properties arise from σ-σ^* delocalization of electrons along the Si-Si backbones. We have reported polysilole nanoaggregates based on aggregation-induced emission effect and observed stronger fluorescent than polysiloles at the identical concentration as described in chapter 8.

This chapter describes the development of new type of composite nanoaggregates which are synthesized from simple blending of two photoluminescence polymers. These composite nanoaggregates result the energy migration of polymethylphenylsilane (PMPS) to polytetraphenylsilole (PTPS) or polytetraphenylgermole (PTPG). PMPS, PTPS, and PTPG exhibit emission bands at 360, 520, and 510 nm, respectively. In nanoaggregates state, energy migrations from PMPS to PTPS or PTPG result increased pholuminescence quantum efficiency of PTPS or PTPG as shown in Figure 11.2.

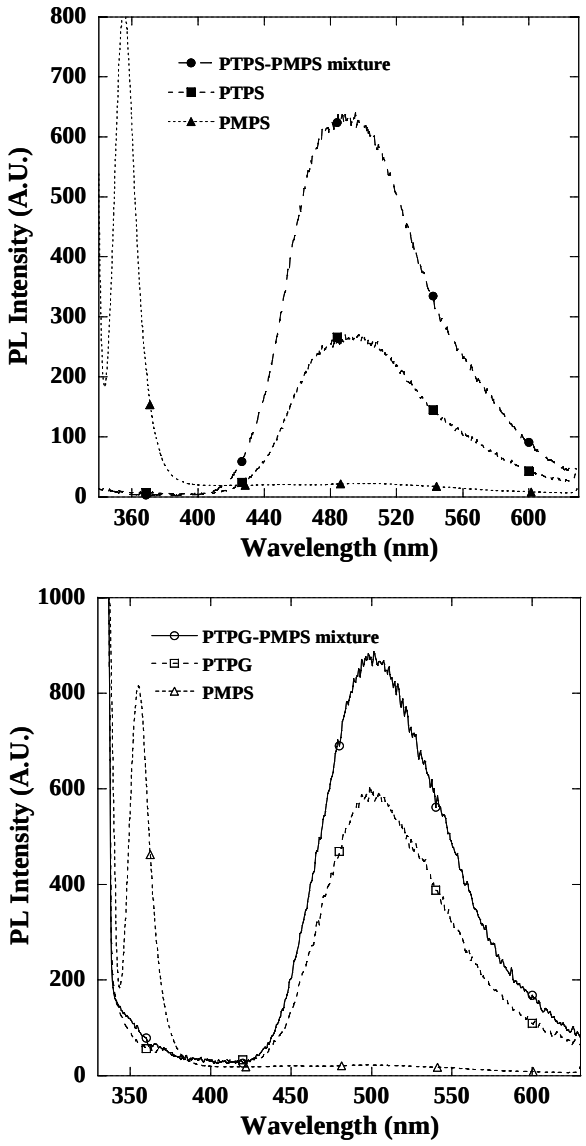

Figure 11.2. PL Spectra of PTPS, PTPG, PMPS, PTPS-PMPS, and PTPG-PMPS mixture in nanoaggregates state

However, it is interesting to note that these energy migrations are not observed in organic solutions where the polymers are completely dissolved as polymer molecules as shown in Figure 11.3.

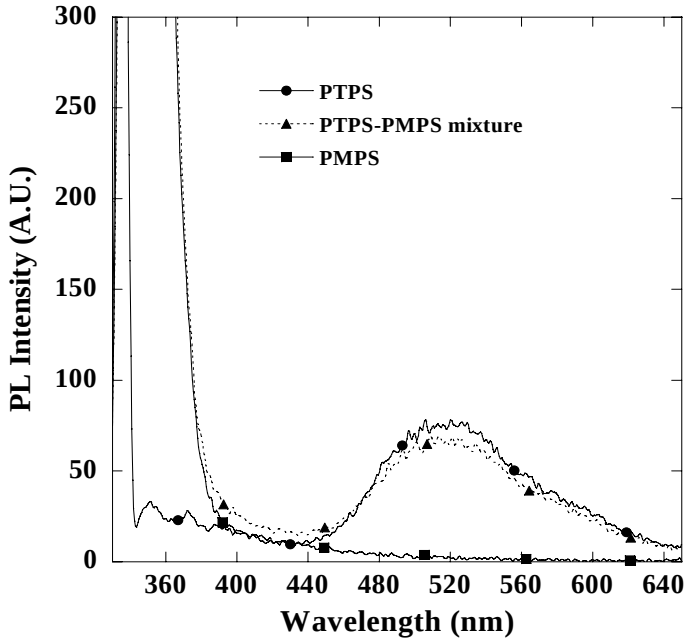

Figure 11.3. PL spectra of PTPS, PMPS, and PTPS-PMPS mixture in molecular state

Efficiency of PL enhancement of polymetalloles increase with incresing of PMPS. Figure 11.4 shows PL spectra of polymetalloles *vs* PMPS weight percent. When the ratios between polymetallole and PMPS in nanoaggregate are PTPS:PMPS = 1:1, PTPG:PMPS = 1:4, and copolymer:PMPS = 1:3, the efficiency of energy migration shows maximum, respectively.

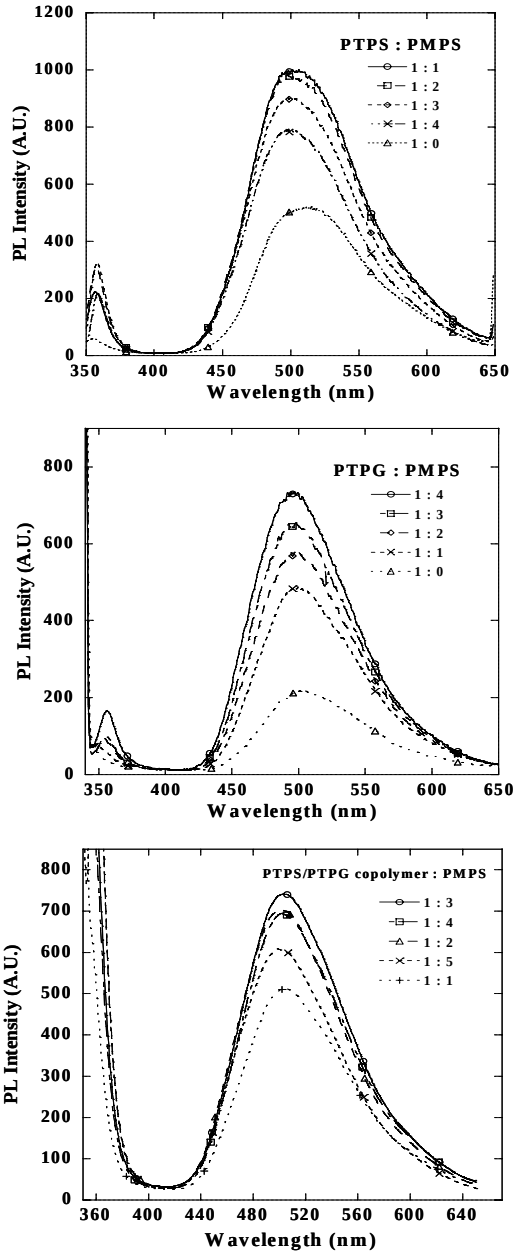

Figure 11.4. PL spectra of polymetalloles *vs* PMPS weight percent

Figure 11.5 shows enhancement of PL efficiency of polymer, polymer nanoaggregates, and polymer/PMPS composite nanoaggregates at the same concentration (1 ppm). For example, PTPS nanoaggragates exhibits 1370% better PL efficiency at 90% water fraction by volume compared with PTPS in organic solvent. In addition, PTPS/PMPS composite nanoaggregates shows about 2550% greater PL efficiency compared with PTPS in THF solution.

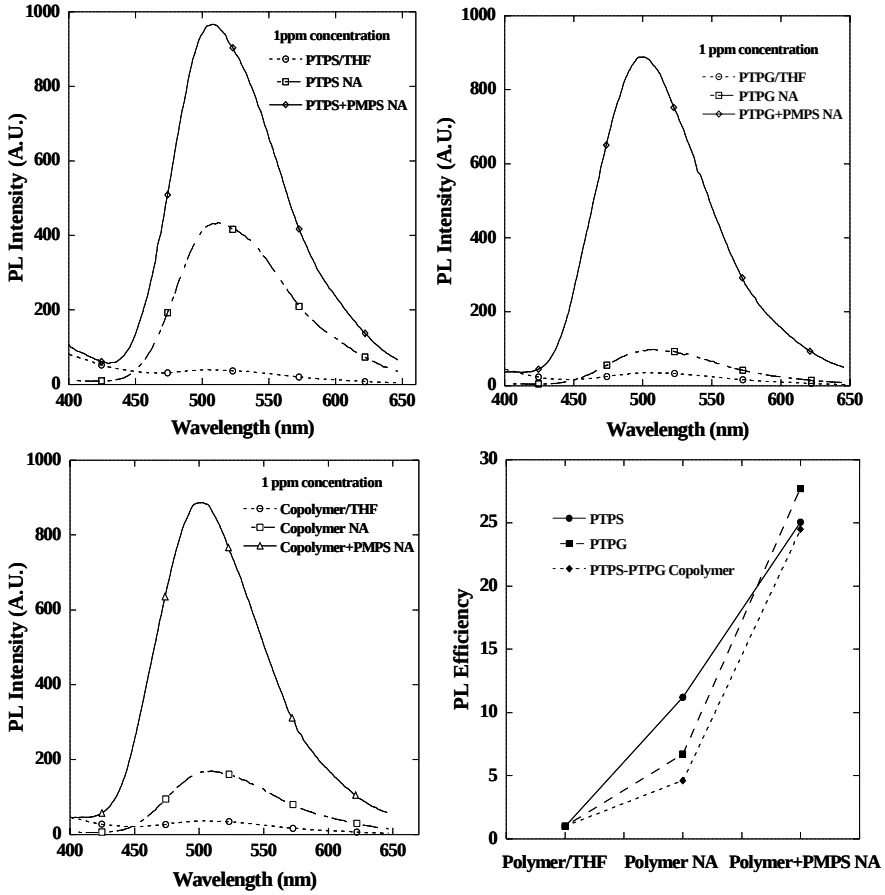

Figure 11.5. Enhancement of PL efficiency of polymer, polymer nanoaggregates, and polymer/PMPS composite nanoaggregates at the same concentration (1 ppm)

A photograph from silole monomer in THF solution to PTPS/PMPS nanoaggregates in the water/THF mixtures under a UV lamp is shown in Figure 11.6, indicating that PTPS/PMPS composite nanoaggregates are more highly fluorescent than silole monomer, polysilole, polysilole nanoaggregates at identical concentration. For silole monomer solution in pure THF, the PL intensity is very weak and an emission peak near 520 nm was observed. In solutions between 0% and 40% water by volume, the emission intensity of PTPS nanoaggregates does not increased. However, the intensity of the emission band increases by about 1370% when the solution is 99% water by volume. As the water fraction is increased, the emission intensity of polysilole nanoaggregates increases dramatically with no shift in the emission wavelength. Moreover, PTPS/PMPS composite nanoaggregates shows about 2550% greater PL efficiency compared with PTPS in THF solution.

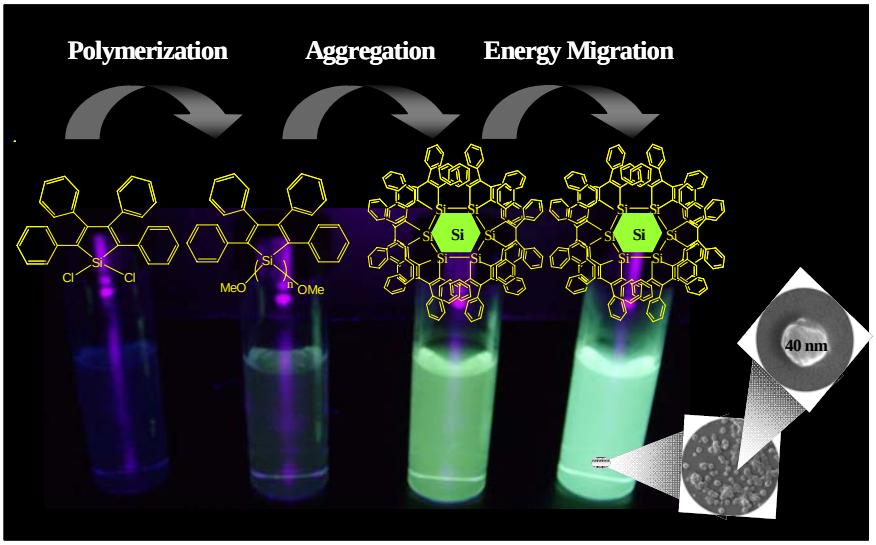

Figure 11.6. Photograph from silole monomer in THF (10 mg/L) to PTPS/PMPS composite nanoaggregates (1:99 by volume, 10 mg/L) under black light

Figure 11.7 shows FE-SEM images of polymetallole/PMPS nanoaggregates. FE-SEM images of polymetallole/PMPS nanoaggregates indicate that the higher water fraction is the smaller aggregate particles. This implies that nanoparticles of polymetallole/PMPS nanoaggregates can be readily tuned by controlling the water fraction. Particle size distributions of polymetallole/PMPS nanoaggregates exhibit between a few nanometer and hundreds nanometers in the water/THF mixtures with 99% and 70% by volumes.

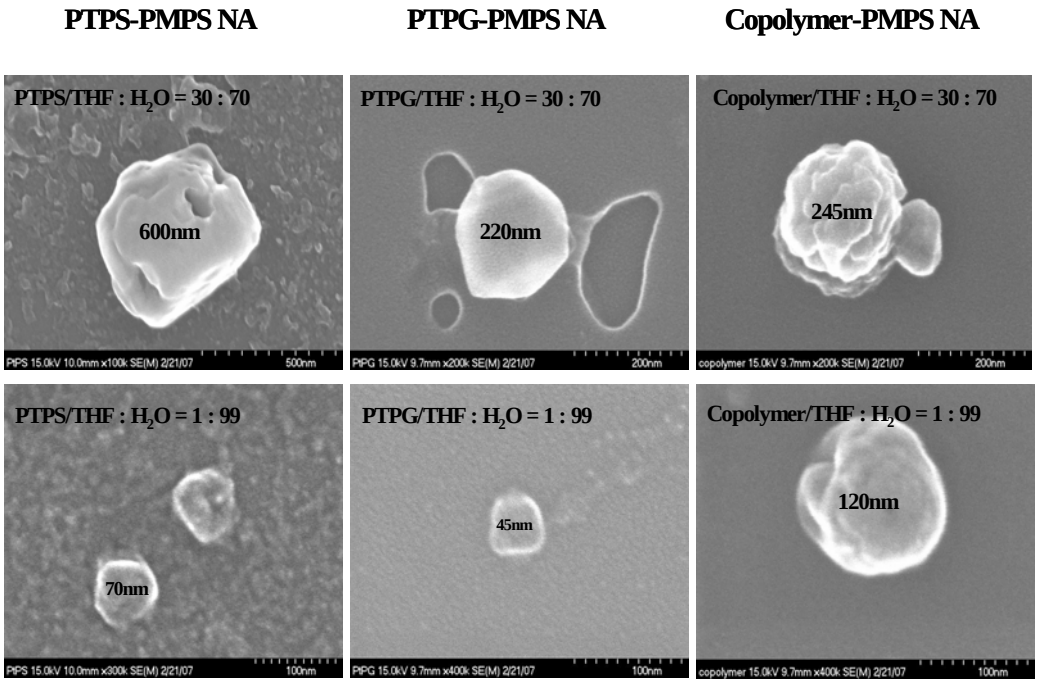

Figure 11.7. FE-SEM images of polymetallole/PMPS nanoaggregates in the water/THF mixtures with 70% (top) and 99% (bottom)

11.3.2 Fluorescence Quenching Studies with Nitroaromatic Analytes

The detection method for nitroaromatic compounds such as 2,4,6-trinitrotoluene (TNT), 2,4-dinitrotoluene (DNT), nitrobenzene, and picric acid involves measurement of the quenching of PL of the Polymetallole/PMPS composite nanoaggregate by adding analytes (using a Perkin-Elmer LS 50B fluorescence spectrometer, 340 nm excitation wavelength).

Quenching PL spectra of Polymetallole/PMPS composite nanoaggregate in 99% water-THF mixture solution were obtained upon successive addition of aliquots of nitroaromatic analytes in water. Figure 11.8~10 display the quenching of PL spectra of the polymetallole/PMPS composit nanoaggregates upon addition of (A) DNT, (B) TNT, and picric acid. PL quenching efficiencies of the polymetallole/PMPS composite nano- aggregates are in the order of picric acid > TNT > DNT.

The purity of the TNT sample was found to be important to obtain reproducible results. It was synthesized by nitration of dinitrotoluene and recrystallized twice from methanol. A third recrystallization produces the same results as the twice-recrystallized material. When the quenching experiment was undertaken without recrystallization of TNT, higher (ca. 10×) quenching percentages are obtained. Presumably, impurities with higher quenching efficiencies are present in crude TNT.

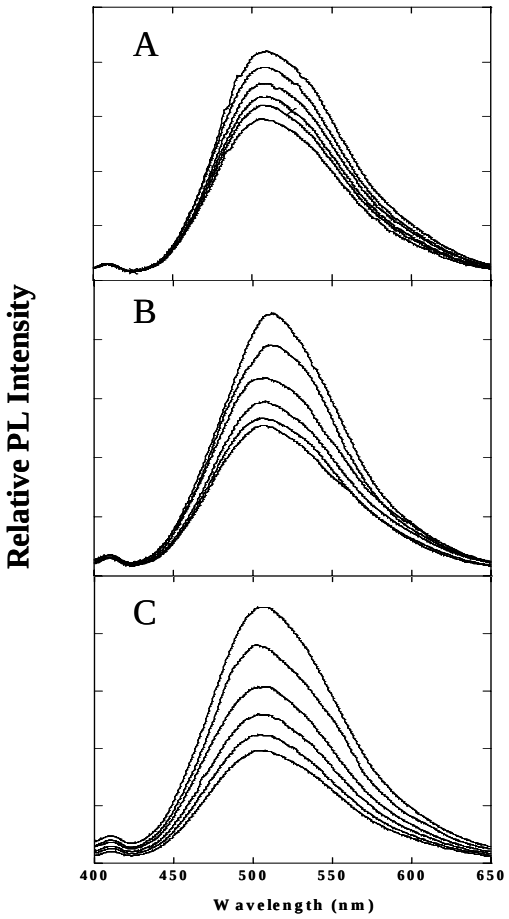

Figure 11.8. Quenching of photoluminescence spectra of PTPS/PMPS composite nanoaggregates with (A) DNT, from top 5.5×10^{-7} M, 1.1×10^{-6} M, 1.65×10^{-6} M, 2.2×10^{-6} M, 2.75×10^{-6} M, 3.3×10^{-6} M, (B) TNT, from top 4.4×10^{-7} M, 8.8×10^{-7} M, 1.32×10^{-6} M, 1.76×10^{-6} M, 2.2×10^{-6} M, 2.64×10^{-6} M, (C) picric acid, from top 4.36×10^{-7} M, 8.72×10^{-7} M, 1.31×10^{-6} M, 1.74×10^{-6} M, 2.18×10^{-6} M, 2.61×10^{-6} M

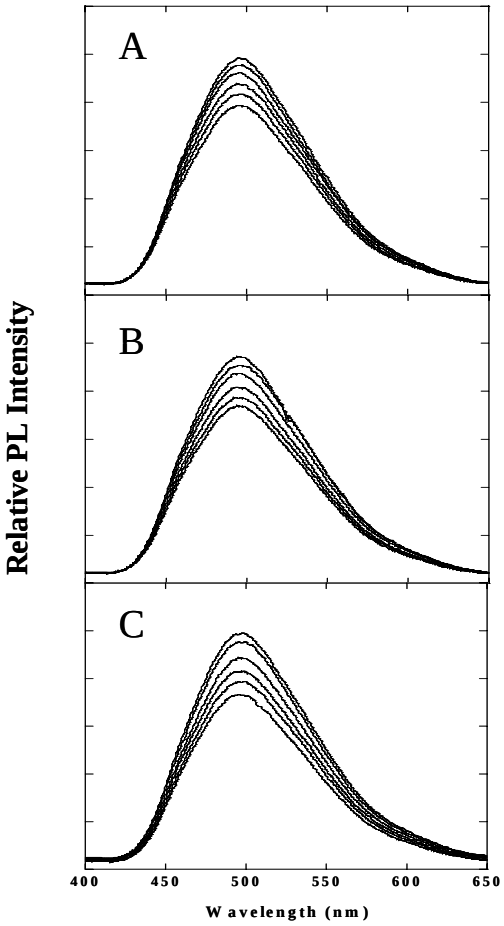

Figure 11.9. Quenching of photoluminescence spectra of PTPG/PMPS composite nanoaggregates with (A) DNT, from top 5.5×10^{-7} M, 1.1×10^{-6} M, 1.65×10^{-6} M, 2.2×10^{-6} M, 2.75×10^{-6} M, 3.3×10^{-6} M, (B) TNT, from top 4.4×10^{-7} M, 8.8×10^{-7} M, 1.32×10^{-6} M, 1.76×10^{-6} M, 2.2×10^{-6} M, 2.64×10^{-6} M, (C) picric acid, from top 4.36×10^{-7} M, 8.72×10^{-7} M, 1.31×10^{-6} M, 1.74×10^{-6} M, 2.18×10^{-6} M, 2.61×10^{-6} M

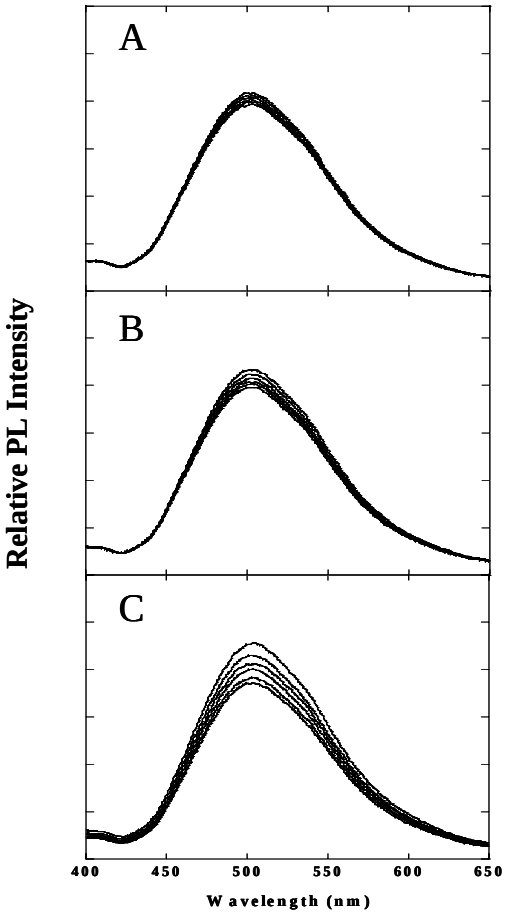

Figure 11.10. Quenching of photoluminescence spectra of PTPS-PTPG Copolymer/PMPS composite nanoaggregates with (A) DNT, from top 5.5×10^{-7} M, 1.1×10^{-6} M, 1.65×10^{-6} M, 2.2×10^{-6} M, 2.75×10^{-6} M, 3.3×10^{-6} M, (B) TNT, from top 4.4×10^{-7} M, 8.8×10^{-7} M, 1.32×10^{-6} M, 1.76×10^{-6} M, 2.2×10^{-6} M, 2.64×10^{-6} M, (C) picric acid, from top 4.36×10^{-7} M, 8.72×10^{-7} M, 1.31×10^{-6} M, 1.74×10^{-6} M, 2.18×10^{-6} M, 2.61×10^{-6} M

11.3.3 Plot Studies of Stern-Volmer

The Stern-Volmer equation was used to quantify the differences in quenching efficiency for various nitroaromatic analytes. In this equation, I_o is the initial fluorescence intensity without analyte concerned, I is the fluorescence intensity with added analyte, [A] is the concentration of analyte, and K_{sv} is the Stern-Volmer constant.

$$(I_o/I\ ) - 1 = K_{sv}\ [A]$$

Figure 11.11 displays Stern-Volmer plots of polymetallole/PMPS composite nano-aggregates for each analyte. A linear Stern-Volmer relationship is observed in all cases, but the Stern-Volmer plot for picric acid exhibits an exponential dependence. A linear Stern-Volmer relationship may be observed if either static or dynamic quenching process is dominant. PL may arise from either a static process, by the quenching of a bound complex, or a dynamic process, by collisionally quenching the excited state [19-20].

For chemosensor applications, it is useful to have sensors with varied responses. Each of the polymer/PMPS composite nanoaggregates exhibits a different ratio of the PL quenching for picric acid, TNT, and DNT and a different response with the same analyte as shown in Figure 11.12. PL quenching efficiencies of the explosive analytes are in the order of PTPS/PMPS composite nanoaggregates > PTPG/PMPS composite nanoaggregates > PTPS-PTPG coplymer/PMPS composite nanoaggregates.

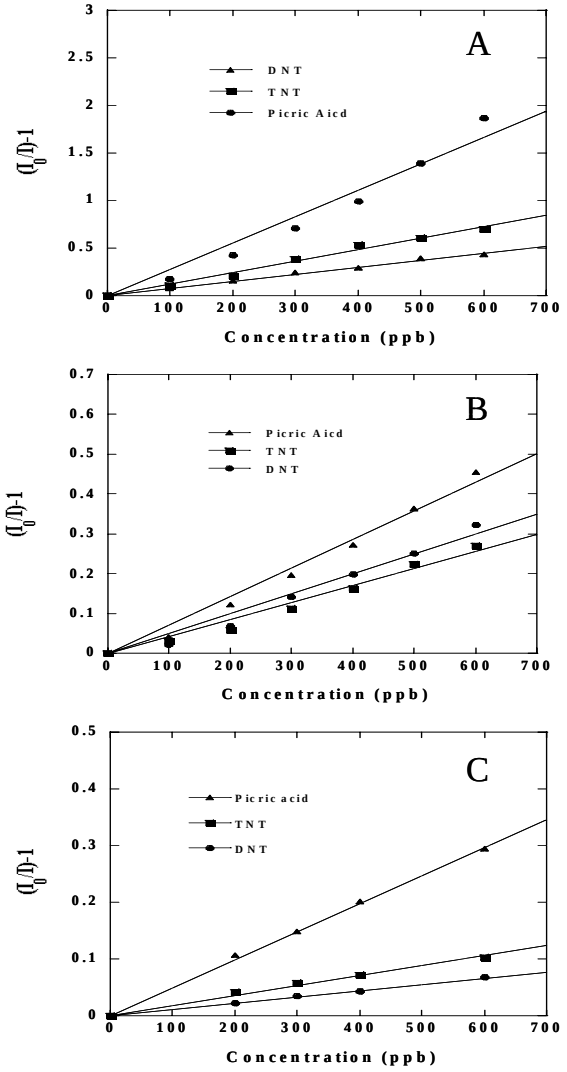

Figure 11.11. Stern-Volmer plots; from top (A) PTPS/PMPS composite nanoaggregates, (B) PTPG/PMPS composite nanoaggregates, and (C) PTPS-PTPG copolymer/PMPS composite nanoaggregates

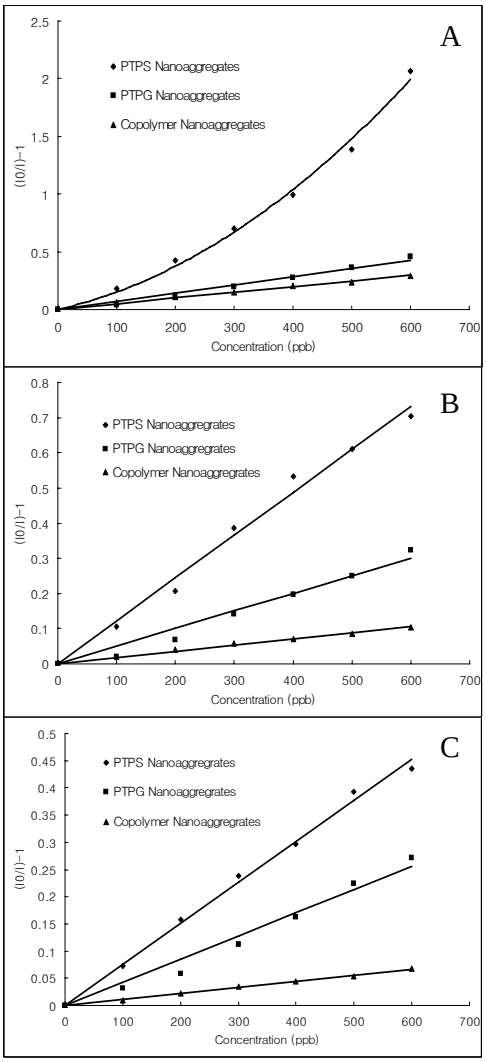

Figure 11.12. Comparison of Stern-Volmer plots; from top (A) picric acid, (B) TNT, and (C) DNT

11.3.4 Visible Trace of TNT

The effect of TNT exposure on PTPS/PMPS composite nanoaggregates-coated substrates is readily visible to the nake eye when the samples are illuminated with a small UV lamp. Thus, PTPS/PMPS composite nanoaggregates can be used as a convenient indicator reagent for TNT residues. Trace amounts of TNT deposited by a glove that was used to handle TNT, and then wiped clean, show up as an easily viewd change in the PL as shown in Figure 11.13. The left hand (silicon rubber gloved) had been rubbed with about 10 mg of TNT, and the glove was brushed to remove all visible TNT particles before being pressed onto the paper sheet. The image taken under UV light demonstrates the utility of PTPS/PMPS composite nanoaggregates for visualizing trace residues of TNT.

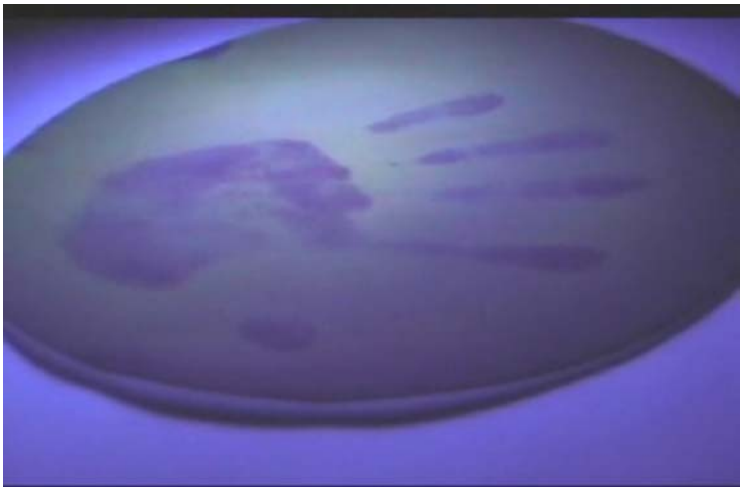

Figure 11.13. TNT residue hand print visualized as quenched luminescence on paper developed with PTPS/PMPS composite nanoaggregates and illuminated with UV light

11.3.5 Detection Mechanism

A schematic diagram of the electron transfer mechanism for the quenching of photoluminescence of the metallole polymers with analyte is shown in Scheme 11.2. Optical excitation produces an electron-hole pair, which is delocalized through the metallole copolymers. When an electron deficient molecule, such as TNT is present, an electron transfer quenching occurs from the conduction band of the metallole copolymers to the LUMO of the analyte. The observed dependence of K_{sv} on analyte reduction potential suggests that for the static quenching mechanism, the polymer aggregates-quencher complex luminescence intensity depends on the electron acceptor ability of the quencher. An alternative explanation would be that the formation constant of the polymer aggregates-quencher complex is dominated by a charge-transfer interaction between polymer aggregates and quencher that the formation constant increase with quencher electron acceptor ability.

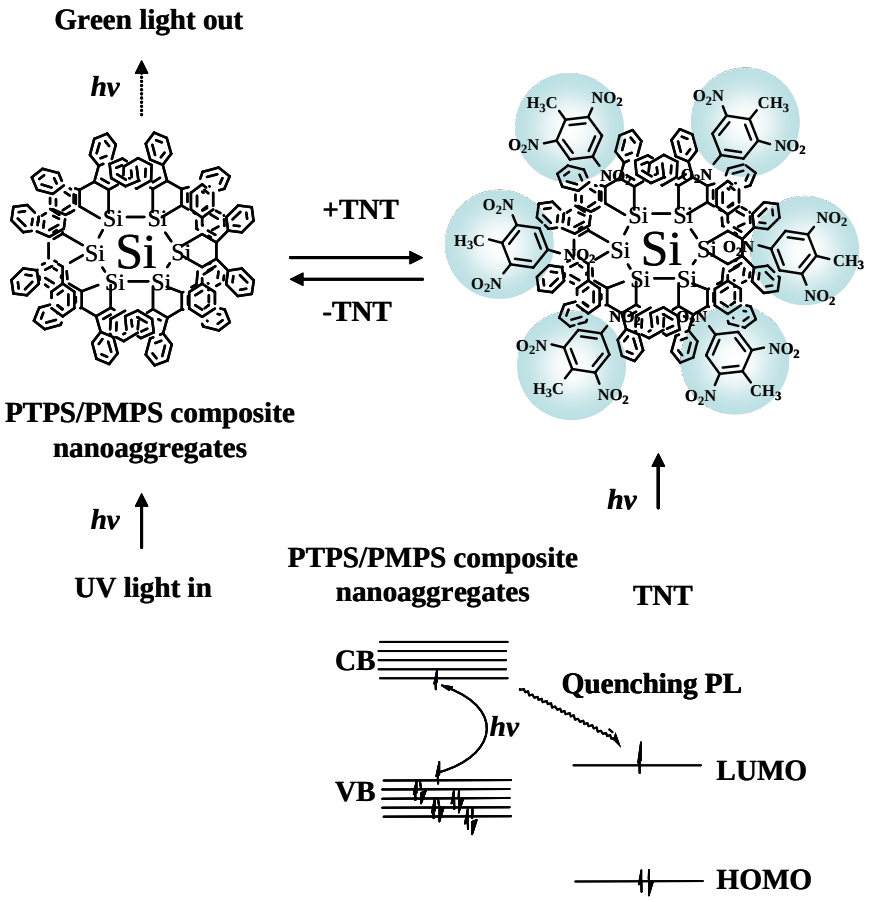

Scheme 11.2. Schematic diagram of electron-transfer mechanism for quenching the PL of polymetallole/PMPS composite nanoaggregates by TNT

11.4 Conclusions

A new chemosensor for nitroaromatic compounds as explosive based on the highly photoluminescenct polymetallole/PMPS composite nanoaggregates has been developed and we have also developed new type of composite nanoaggregates which are synthesized from simple blending of two photoluminescence polymers for sensing explosives.

The detection of explosives is achieved from the measuring of quenching PL of polymetallole/PMPS composite nanoaggregates by adding the analyte. PL quenching of polymetallole/PMPS composite nanoaggregates was immediately observed in air and water. A nonlinear relationship of Stern-Volmer plot for TNT detection was obtained. The efficiency of photoluminescence quenching is in the order of picric acid > TNT > DNT, which is correlated with their reduction potentials. The mechanism of quenching would involve electron transfer from the conduction band of polymetallole/PMPS composite nanoaggregates to the analyte. This result indicates that the quenching PL properties strongly depend on the electrostatic interactions between electron rich polymer aggregates and electron deficient analytes. The polymetallole/PMPS composite nanoaggregates are quite insensitive to common interferents in air and water.

11.5 References

[1] A. R. Maureen, C&EN News 1997, 14-22.

[2] K. Hakansson, R. V. Coorey, R. A. Zubarev, V. L. Talrose, and P. J. Hakansson, *Mass Spectrom*. **35**, 337 (2000).

[3] J. M. Sylvia, J. A. Janni, J. D. Klein, and K. M. Spencer, *Anal*. *Chem*. **72**, 5834 (2000).

[4] V. P. Anferov, G. V. Mozjoukhine, and R. Fisher, *Rev*. *Sci*. *Instrum*. **71**, 1656 (2000).

[5] R. D. Luggar, M. J. Farquharson, J. A. Horrocks, and R. J. J. Lacey, *X-ray Spectrom*. **27**, 87 (1998).

[6] A. M. Rouhi, *Chem*. *Eng*. *News*, **75**, 14 (1997).

[7] J.-S. Yang and T. M. Swager, *J*. *Am*. *Chem*. *Soc*. **120**, 11864 (1998).

[8] J.-S. Yang and T. M. Swager, *J*. *Am*. *Chem*. *Soc*. **120**, 5321 (1998).

[9] H. Sohn, R. M. Calhoun, M. J. Sailor, and W. C. Trogler, *Angew. Chem. Int. Ed.* **11**, 2104 (2001).

[10] H. Sohn, M. J. Sailor, D. Magde, and W. C. Trogler, *J. Am. Chem. Soc.* **125**, 3821 (2003).

[11] D. D. C. Bradley, *Chem. Brit.* **27**, 719 (1991).

[12] J. H. Burroughes, C. A. Jones, and R. H. Friend, *Nature* **335**, 137 (1988).

[13] J. H. Burroughes, D. D. C. Bradley, A. R. Brown, R. N. Marks, K. Mackay, R. H. Friend, P. L. Burns, and A. B. Holmes, *Nature* **347**, 539 (1990).

[14] Y. Yang and A. J. Heeger, *Nature* **372**, 344 (1994).

[15] R. H. Friend, R. W. Gymer, A. B. Holmes, J. H. Burroughes, R. N. Marks, C. Taliani, D. D. C. Bradley, D. A. D. Santos, J. L. Bredas, M. Logdlund, and W. R. Salaneck, *Nature* **397**, 121 (1999).

[16] R. West, H. Sohn, D. R. Powell, T. Mueller, and Y. Apeloig, *Angew. Chem. Int. Ed.* **35**, 1002 (1996).

[17] R. West, H. Sohn, U. Bankwitz, J. Calabrese, Y. Apeloig, and T. Mueller, *J. Am. Chem. Soc.* **117**, 11608 (1995).

[18] K. Oka, M. Fukudoma, T. Dohmaru, and R. West, *Electrophotography* **34**, 386 (1995).

[19] K. A. Connors, Binding constant: The Measurement of molecular Complex Stability, Wiley-Interscience, New York, (1987).

[20] J. R. Lakowicz, *Priciples of Fluorescence Spectroscopy*, Plenum Press, New York, (1986).

Chapter Twelve
New Synthetic Route of Alkyl-Terminated Silicon Nanoparticles and Their Optical Characteristics

12.1 Introduction

Over the past decade there has been considerable interest in semiconductor nanoparticles for their unusual properties resulting from the confinement of carriers in all three dimensions and for their possible applications in electronics, optics, and sensors such as a diode lasers [1-3]. These unusual properties are attributed to quantum confinement effects which occur when the size of the particle becomes smaller than the exciton diameter of the bulk semiconducting material. There have been extensive studies of II-VI semiconductor nanoparticles, particularly cadmium selenide monodisperse nanoparticles [4-7]. Good quality nanocrystals of some III-V nanoparticles such as InP and InAs have also been synthesized [8-10]. Recent advances have resulted in the large-scale preparation of relatively monodisperse quantum dots [5,11-15], the fabrication of quantum dot arrays [16-21], light-emitting diodes [22], and fluorescent probes for biomolecule detection [23-24]. The colloidal chemical technique has been used to prepare high quality dots in the nanosize regime, but only a limited number of materials have been successfully produced by these methods.

Since nanocrystalline forms of Si luminesce intensely over a range of wavelengths, with emission occurring primarily in the blue and the red spectral regions [25-26], this would enable a broad range of optoelectronic applications

involving efficient silicon-based emitters. Preparations of silicon quantum dots have been investigated by several groups. However there has been little advancement in synthetic methods for the production of group IV nanoparticles despite the large interest in nanostructured Si. First, colloidal suspensions of silicon nanoparticles can be prepared by the ultrasonic dispersion of electrochemically etched silicon wafers [27-28]. Several different routes are also available for the preparation of silicon nanoparticles, including both gas-phase and solution decomposition of silanes [29-31]. A sonochemical procedure for generating silicon nanoparticles has also been reported based on ultrasound induced reduction of tetraethyl orthosilicate (TEOS) with colloidal sodium in toluene solvent at -70^{o}C [32]. More recently, efficient solution syntheses for the group IV semiconductor nanocrystals were reported from the reaction of the Zintl salt, Mg_2M or NaM (M = Si [33-34], Ge [35-36], or Sn [37]) with $SiCl_4$ in ethylene glycol as well as the solution reduction of silicon halides by lithium naphthalenide [38-39].

Here an approach has been made for the synthesis of silicon nanoparticles by an improvement in the solution reduction method. This synthesis covers the reaction of silicon tetrachloride with sodium benzophenone in glyme as a solvating medium to give rise to chloride capped silicon nanoparticle that can further be terminated by *n*-butyllithium as source for surface-derivatization. Surface-derivatization is expected to provide long stability to the nanoparticle.

12.2 Experiments

12.2.1 Materials

Sodium (Aldrich, 99%), benzophenone (Aldrich, 99%), silicon tetrachloride ($SiCl_4$, Aldrich, 99.999%), and *n*-butyllithium (Aldrich, 1.6 M in hexane) were used without further purification. Ethylene glycol dimethyl ether (glyme) was dried and distilled from a sodium-potassium (Na-K) alloy under argon gas. The Na-K alloy was freshly prepared from a mixture of sodium and potassium pieces (Aldrich, 98%). HPLC-grade water (Aldrich) and HPLC-grade hexane (Aldrich) were used as received. Manipulations of these chemicals were handled via standard Schlenk line techniques. Glasswares were silonated by reaction for 1 h with a 2% solution of $(CH_3)_2SiCl_2$ in toluene followed by repeated washes with hexane and methanol and dried overnight at 120℃.

12.2.2 Synthesis of Sodium Benzophenone Ketal

Sodium metal (523.9 mg, 22.8 mmol) was added to a Schlenk flask in a drybox and transfer to a Schlenk line. Benzophenone (4.154 g, 22.8 mmol) was subsequently added under argon. Approximately 60 mL of freshly distilled and degassed glyme was added to the solids, and the mixture was stirred vigorously overnight. The color of the solution changed from colorless to dark blue upon the dissolution of Na metal.

12.2.3 Synthesis of N-butyl-terminated Si Nanoparticles

60 mL of a solution of Na/benzophenone ketal was added rapidly via cannular to 2.23 g (13 mmol) of silicon tetrachloride in 100 mL of glyme in a Schlenk flask at room temperature with rapid stirring. The solution color changed from clear solution to a dark blue suspension upon the addition of the Na/benzophenone ketal mixture. It was allowed to stir for 2 h. After stirred for 10 min, the suspension was allowed settle. A dark brown solid appeared at the bottom of the flask and a bright yellow solution appeared on the top. The top solution was transferred via cannular to new Schlenk flask and vacuum dried to remove the benzophenone by sublimation. 100 mL of distilled glyme was added to the flask, followed by 8.2 mL of *n*-butyllithium. The mixture was allowed to stir for overnight. The mixture was pumped down to dryness, the organicterminated product was extracted with hexane, and the extract was rinsed with water. After the removal hexane and any residual benzophenone, 500 mg of viscous brown oil (soluble in hexane or chloroform) was obtained. Synthetic procedure of *n*-butyl-capped Si nanoparticles is described in Scheme

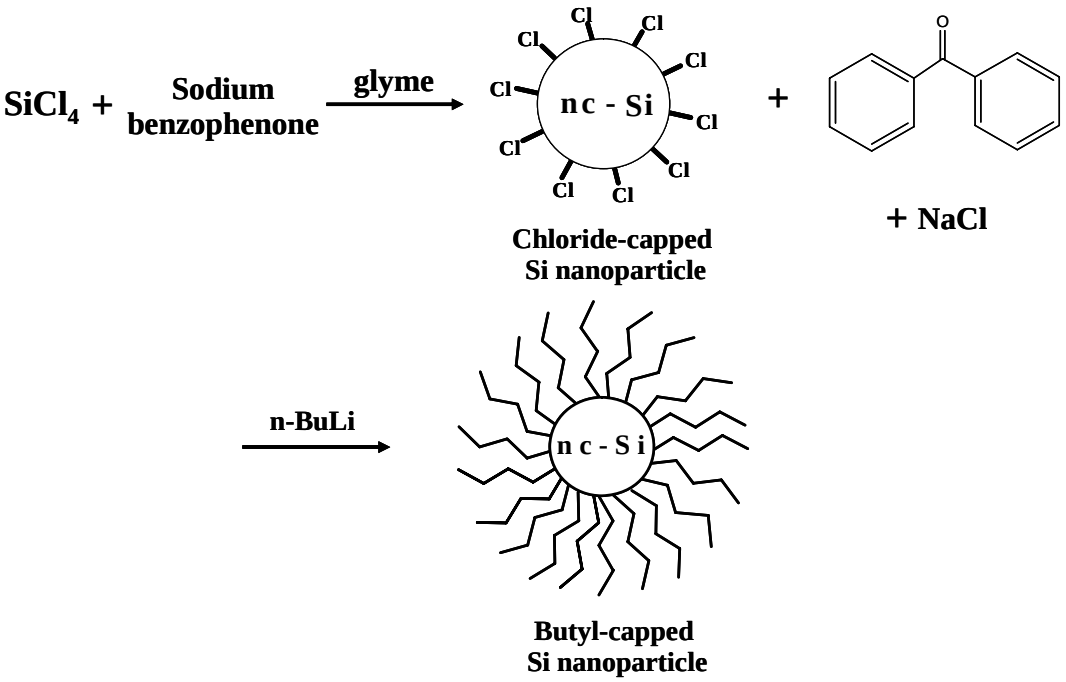

Scheme 12.1. Preparation of butyl-capped silicon nanoparticles

12.2.4 Characterization

Optical characteristics of silicon nanoparticles were characterized by FT-IR (Nicolet 5700), UV-vis absorption (Shimadzu, UV-2401 spectrophotometer), and photoluminescence spectroscopy (Perkin-Elmer, LS 55 luminescence spectrophotometer). Size contribution of *n*-butyl-capped Si nanoparticles was measured by PSA (Microtrac, UPA-150). The TEM images of *n*-butyl-capped Si nanoparticles were obtained using a Tecnai F20 transmission electron microscope. Samples for TEM analysis were prepared by dip-coating a solution of a sample on formvar/carbon-film Cu grids (20 mesh, 3 mm). The average particle size and distribution were determined based on the measurement of at least 100 particles.

12.3 Results and Discussion

The colloidal chemical technique was used to prepare high quality II-VI nanoparticles in the nanosize regime, but only a limited number of materials were successfully produced by these methods [15]. Although there was significant progress in size and shape control of II-VI semiconductors, there was very little in the pursuit of Si nanoparticles. The use of metal silicides was investigated as precursors to silicon nanoparticles with subsequent surface passivation with organic ligands [33]. The synthesis involved a metathesis reaction of the metal silicide with silicon tetrachloride and subsequent termination with alkyl groups. However, Mg_2Si does not dissolve in any solvent to an appreciable extent, it can be assumed that the reaction is a heterogeneous surface reaction, and the size and shape control are not possible. Recently, the use of sodium naphthalenide to reduce $SiCl_4$ was reported to produce amorphous silicon nanoparticles with various sizes from 3 to 9 nm in diameter.

Tri-*n*-octylphosphineoxide (TOPO) surfactant in CdSe nanoparticles ensured the solubility of the nanoparticles in nonpolar solvents. Control might be possible through the use of coordinating ligands to produce an even size distribution of nanoparticles. Herein, we reported a new room temperature solution synthesis of crystalline silicon nanoparticles with macroscopic amounts. The silicon nanoparticles were obtained from the reduction of $SiCl_4$ with Na/benzophenone ketal. Na/benzophenone acted as both reducing agent to produce nanoparticles and surfactant to control size of nanoparticles, provided a medium that allowed for better mixing of the reagents, and prevented the particles from agglomerating.

Silicon tetrachloride was reduced with Na/benzophenone in a diluted 1,2-dimethoxyethane (glyme) solution at room temperature under inert argon gases.

The as-synthesized chloride-capped nanoparticles were converted to silanide Si nanoparticles via termination treatments of alkylation. TEM, high resolution TEM, and selected area electron diffraction (SAED) were used to confirm the identity of the nanoparticles isolated in hexane. Figure 12.1(A) showed the TEM micrograph for the as-prepared *n*-butyl-capped Si nanoparticles. The sizes of silicon nanoparticles ranged from 4 to 9 nm in diameter. The nanoparticles appeared to be of uniform size but there were large numbers of particles that were aggregated. Selected lattice fringes and area electron diffraction showed a diffraction pattern consistent with a Si single crystalline structure as shown in Figure 12.1(B and C)

Figure 12.2 showed the histogram of the size distributions derived from the *n*-butyl-capped Si nanoparticles corresponding with TEM images. The average diameter of *n*-butyl-capped Si nanoparticles was 6.5 nm.

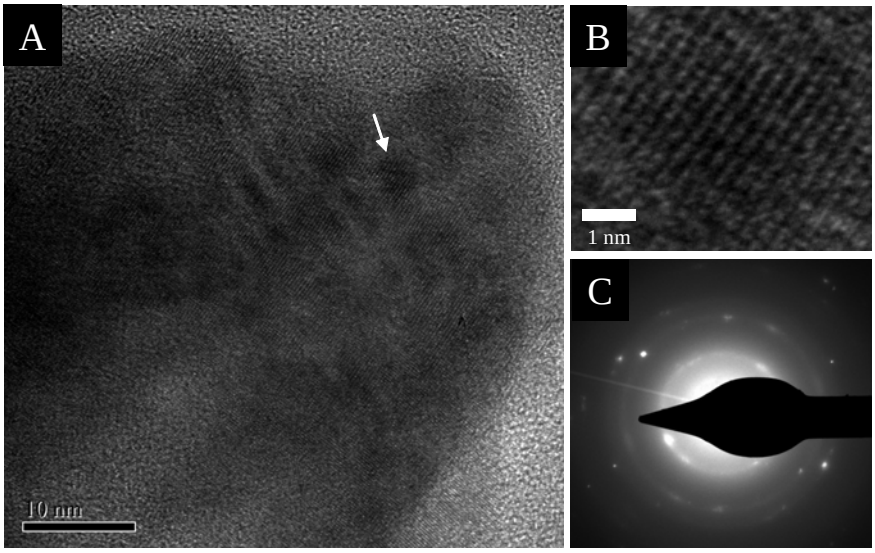

Figure 12.1. TEM micrograph for the as-prepared *n*-butyl-capped Si nanoparticles (A, B) and selected area electron diffraction (SAED) patterns of *n*-butyl-capped Si nanoparticles (C)

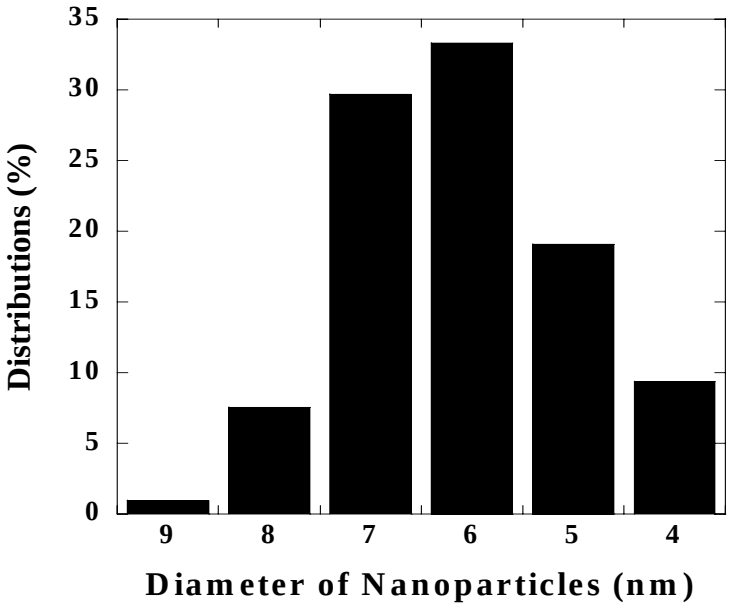

Figure 12.2. Particle size distributions of *n*-butyl-capped Si nanoparticles

FT-IR spectroscopy was used to identify and characterize the organic species on the Si nanoparticle surfaces. FT-IR spectrum for an *n*-butyl-capped Si nanoparticle shown in Figure 12.3 showed characteristic vibrational frequencies for C-H mode. Strong peaks corresponding to alkyl C-H_x bonds at 2960, 2937, 2871, 1494, and 1460 cm^{-1} appeared after treatment with *n*-butyllithium. The band assignments to the functional group were taken from the literature [40].

Optical absorption and photoluminescence spectroscopy were used to investigate the optical properties of Si nanoparticles. An absorption edge appeared at approximately 360 nm for the *n*-butyl-capped Si nanoparticles. There was no detectable emission observed in the spectra above 600 nm. Photoluminescence spectra were measured at room temperature and the emission spectra were collected with excitation wavelengths ranging from 300 to 380 nm. The monotonic shift of the PL as a function of excitation wavelength resulted from the excitation of different sizes of nanocrystals that have different optical transition energies. The maximum intensity of emission spectrum was centered at 410 nm with an excitation wavelength of 360 nm as shown in Figure 12.4(A). The PL spectra of the silicon nanoparticles showed 80-97 nm of full-widths at half-maximum (FWHM). Very important factor in the ultimate utility of the silicon nanoparticles in applications and investigations of their surface chemistry was the long-term stability of their optical properties. Lack of PL stability significantly hampered applications of silicon nanoparticles. Surface-derivatization was expected to provide long stability to the nanoparticle. The stabilization of the particle was usually accomplished by capping or passivating the surface with molecules that were covalently attached to the particle. The stability of *n*-butyl-capped Si nanoparticles was investigated, and the PL intensity remained unchanged over the week as shown in Figure 12.4(B). This indicated that *n*-butyl-capped Si nanoparticles exhibited

neither aggregation nor degradation.

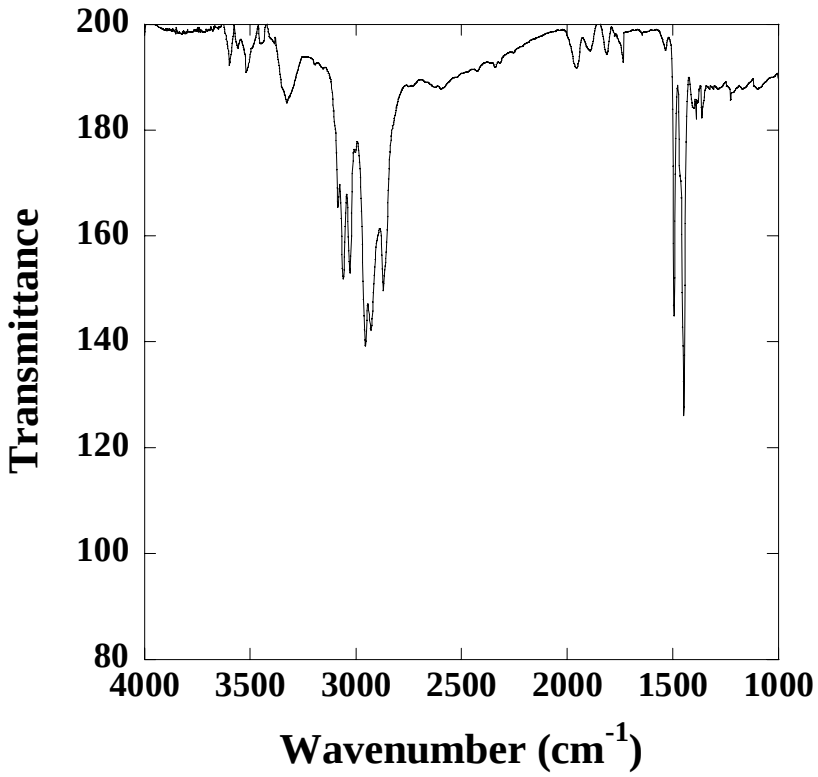

Figure 12.3. FT-IR spectrum for silicon nanoparticles terminated with *n*-butyl groups

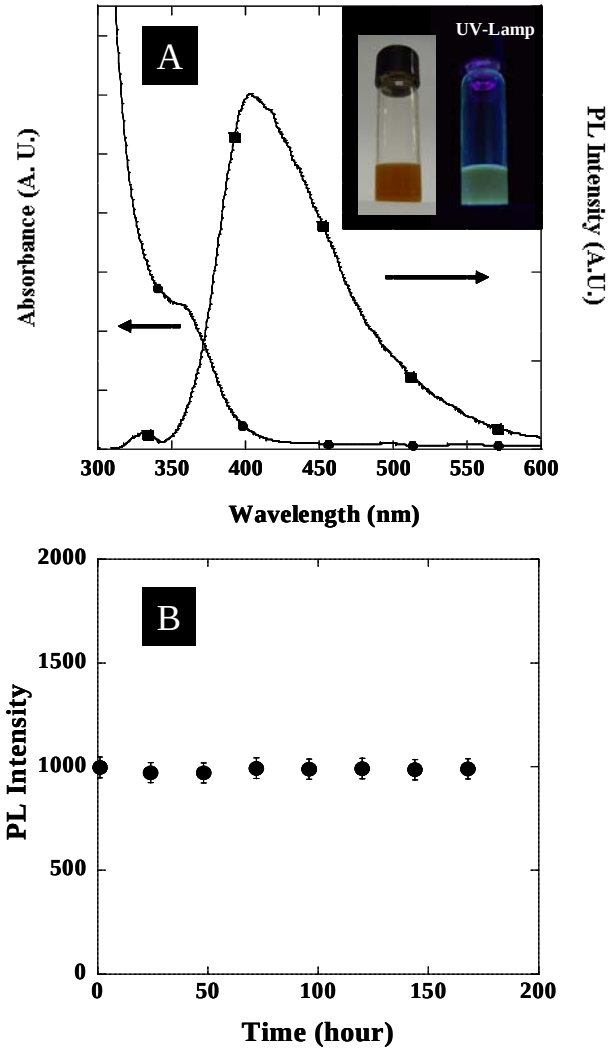

Figure 12.4. UV absorption and PL spectra of *n*-butyl-capped Si nanoparticles (A) and stability measurement of PL of *n*-butyl-capped Si nanoparticles (B)

12.4 Conclusions

A new room temperature solution synthesis of crystalline silicon nanoparticles, alkyl-capped nanocrystalline silicon (R-n-Si), was achieved from the reaction of silicon tetrachloride with sodium benzophenone ketal, followed by *n*-butyllithium. Na/benzophenone and *n*-butyllithium served as an effective reducing agent for silicon tetrachloride to build nanoclusters and good passivating agent for surface-derivatization for the synthesis of *n*-butyl-capped Si nanoparticles, respectively. This method was able to produce in macroscopic amount of silicon nanoparticles with brighter and visible PL. Optical Characteristics of *n*-butyl-capped Si nanoparticles were measured by FT-IR, UV-vis and PL spectroscopy. Butyl-capped Si nanoparticles exhibited an emission band at 410 nm with excitation wavelength of 360 nm. Diameters of *n*-butyl-capped Si nanoparticles were investigated by TEM, HR-TEM, SAED, and PSA. Average size of *n*-butyl-capped Si nanoparticles was about 6.5 nm in diameter.

12.5 References

[1] A. P. Alivisatos, *Science* **271**, 933 (1996).

[2] A. P. Alivisatos, *J. Phys. Chem.* **100**, 13226 (1996).

[3] D. L. Feldheim and C. D. Keating, *Chem. Soc. Rev.* **27**, 1 (1998).

[4] C. B. Murray, D. J. Norris, and M. G. Bawendi, *J. Am. Chem. Soc.* **115**, 8706 (1993).

[5] J. E. B. Katari, V. L. Colvin, and A. P. Alivisatos, *J. Phys. Chem.* **98**, 4109 (1994).

[6] T. Vossmeyer, L. Katsikas, M. Giersig, I. G. Popovic, K. Diensner, A. Chemseddine, A. Eychmuller, and H. Weller, *J. Phys. Chem.* **98**, 7665 (1994).

[7] S. G. Hickey and D. J. Riley, *J. Phys. Chem.* **103**, 4599 (1999).

[8] O. I. Micic, J. R. Sprague, C. J. Curtis, K. M. Jones, J. L. Machol, A. J. Nozik, B. Giessen, B. Fluegel, G. Mohs, and N. Peyghambarian, *J. Phys. Chem.* **99**, 7754 (1995).

[9] A. A. Guzelian, J. E. B. Katari, U. Banin, A. V. Kadavanich, K. Hamad, E. Juban, A. P. Alvisatos, R. H. Wolters, C. C. Arnold, and J. R. Heath, *J. Phys. Chem.* **100**, 7212 (1996).

[10] M. A. Olshavsky, A. N. Goldstein, and A. P. Alivisatos, *J. Am. Chem. Soc.* **112**, 9438 (1990).

[11] M. Nirmal, B. O. Dabbousi, M. G. Bawendi, J. J. Macklin, J. K. Trautman, T. D. Harris, and L. E. Brus, *Nature* **383**, 802 (1996).

[12] M. A. Hines and P. GnyotSionnest, *J. Phys. Chem.* **100**, 468 (1996).

[13] M. Kuno, J. K. Lee, B. O. Dabbousi, F. V. Mikulec, and M. G.Bawendi, *J. Chem. Phys.* **106**, 9869 (1997).

[14] B. O. Dabbousi, J. RodriguezViejo, F. V. Mikulec, J. R. Heine, H. Mattoussi, R. Ober, K. F. Jensen, and M. G. Bawendi, *J. Phys. Chem.* **101**, 9463 (1997).

[15] F. V. Mikulec, M. Kuno, M. Bennati, D. A. Hall, R. G. Griffin, and M. G. Bawendi, *J. Am. Chem. Soc.* **122**, 2532 (2000).

[16] R. P. Andres, J. D. Bielefeld, J. I. Henderson, D. B. Janes, V. R. Kolagunta, C. P. Kubiak, and W. J. Mahoney, and R. G. Osifchin, *Science* **273**, 1690 (1996).

[17] C. B. Murray, C. R. Kagan, and M. G. Bawendi, *Science* **270**, 1335 (1995).

[18] J. R. Heath, R. S. Williams, J. J. Shiang, S. J.Wind, J. Chu, C. Demic, W. Chen, C. L. Stanis, and J. J. Bucchignano, *J. Phys. Chem.* **100**, 3144 (1996).

[19] C. P. Collier, R. J. Saykally, J. J. Shiang, S. E. Henrichs, and J. R. Heath, *Science* **277**, 1978 (1997).

[20] C. A. Mirkin, R. L. Letsinger, R. C. Mucic, and J. J. Storhoff, *Nature* **382**, 607 (1996).

[21] A. P. Alivisatos, K. P. Johnsson, X. G. Peng, T. E. Wilson, C. J. Loweth, M. P. Bruchez, and P. G. Schultz, *Nature* **382**, 609 (1996).

[22] V. L. Colvin, M. C. Schlamp, and A. P. Alivisatos, *Nature* **370**, 354 (1994).

[23] M. Bruchez, M. Moronne, P. Gin, S. Weiss, and A. P. Alivisatos, *Science* **281**, 2013 (1998).

[24] W. C. W. Chan and S. M. Nie, *Science* **281**, 2016 (1998).

[25] L. Brus, *J. Phys. Chem.* **98**, 3575 (1994).

[26] A. G. Cullis, L. T. Canham, and P. D. J. Calcott, *J. Appl. Phys.* **82**, 909 (1997).

[27] J. L. Heinrich, C. L. Curtis, G. M. Credo, K. L. Kavanagh, and M. J. Sailor, *Science* **255**, 66 (1992).

[28] R. A. Bley, S. M. Kauzlarich, J. E. Davis, and H. W. H. Lee, *Chem. Mater.* **8**, 1881 (1996).

[29] K. A. Littau, P. J. Szajowski, A. J. Muller, A. R. Kortan, and L. E. Brus, *J. Phys. Chem.* **97**, 1224 (1993).

[30] A. Fojtic and A. Heinglein, *Chem. Phys. Lett.* **221**, 363 (1994).

[31] J. D. Holmes, K. J. Ziegler, R. C. Doty, L. E. Pell, K. P. Johnston, and B. A. Korgel, *J. Am. Chem. Soc.* **123**, 3742 (2001).

[32] N. A. Dhas, C. P. Raj, and A. Gedanken, *Chem. Mater.* **10**, 3278 (1998).

[33] C. S. Yang, R. A. Bley, S. M. Kauzlarich, H. W. H. Lee, and G. R. Delgado, *J. Am. Chem. Soc.* **121**, 5191 (1999).

[34] R. A. Bley and S. M. Kauzlarich, *J. Am. Chem. Soc.* **118**, 12461 (1996).

[35] B. R. Tayler, S. M. Kauzlarich, H. W. H. Lee, and G. R. Delgado, *Chem. Mater.* **10**, 22 (1998).

[36] B. R. Taylor, S. M. Kauzlarich, G. R. Delgado, and H. W. H. Lee, *Chem. Mater*. **11**, 2493 (1999).

[37] C. S. Yang, Q. Liu, S. M. Kauzlarich, and B. Phillips, *Chem*. *Mater*. **12**, 983 (2000).

[38] J. R. Heath, *Science* **258**, 1131 (1992).

[39] R. K. Baldwin, K. A. Pettigrew, J. C. Garno, P. P. Power, G.-Y. Liu, and S. M. Kauzlarich, *J. Am*. *Chem*. *Soc*. **124**, 1150 (2002).

[40] C. S. Yang, S. M. Kauzlarich, Y. C. Wang, and H. W. H. Lee, *J. Clust*. *Sci*. **11**, 423 (2000).

저작물 이용 허락서

학 과	화학과	학 번	20067294	과 정	박사
성 명	한글: 장 승 현 한문: 張 勝 賢 영문: Jang, Seunghyun				
주 소	광주광역시 북구 오치동 1028-5				
연락처	E-mail : twimh108@naver.com				
논문제목	**한글 : 다공성 실리콘과 실리콘 나노입자를 기초로 한 화학 및 생물학 센서의 개발** **영문 : Development of Chemical and Biological Sensors Based on Porous Silicon and Silicon Nanoparticles**				

본인이 저작한 위의 저작물에 대하여 다음과 같은 조건아래 조선대학교가 저작물을 이용할 수 있도록 허락하고 동의합니다.

- 다 음 -

1. 저작물의 DB구축 및 인터넷을 포함한 정보통신망에의 공개를 위한 저작물의 복제, 기억장치에의 저장, 전송 등을 허락함.
2. 위의 목적을 위하여 필요한 범위 내에서의 편집·형식상의 변경을 허락함. 다만, 저작물의 내용변경은 금지함.
3. 배포·전송된 저작물의 영리적 목적을 위한 복제, 저장, 전송 등은 금지함.
4. 저작물에 대한 이용기간은 5년으로 하고, 기간종료 3개월 이내에 별도의 의사표시가 없을 경우에는 저작물의 이용기간을 계속 연장함.
5. 해당 저작물의 저작권을 타인에게 양도하거나 또는 출판을 허락을 하였을 경우에는 1개월 이내에 대학에 이를 통보함.
6. 조선대학교는 저작물의 이용허락 이후 해당 저작물로 인하여 발생하는 타인에 의한 권리 침해에 대하여 일체의 법적 책임을 지지 않음.
7. 소속대학의 협정기관에 저작물의 제공 및 인터넷 등 정보통신망을 이용한 저작물의 전송·출력을 허락함.

동의여부 : 동의 (○), 반대 ( )

2009년 2월 일

저작자: 장 승 현 (서명 또는 인)

조선대학교 총장 귀하